New Image Fusion Schemes using Hilbert Vibration Decomposition (HVD), Fractional Fourier Transform (FRFT) and Graph Signal Processing (GSP) Techniques

Submitted in

fulfillment of the requirements for the degree of

Doctor of Philosophy

by

Nidhi Saxena
ID: 2014REC9027

Under the Supervision of

Prof. Kamalesh Kumar Sharma

DEPARTMENT OF ELECTRONICS AND COMMUNICATION ENGINEERING
MALAVIYA NATIONAL INSTITUTE OF TECHNOLOGY, JAIPUR

July 2018

DECLARATION

I, Nidhi Saxena, declare that this thesis titled, "**New Image Fusion Schemes using Hilbert Vibration Decomposition (HVD), Fractional Fourier Transform (FRFT) and Graph Signal Processing (GSP) Techniques**" and the work present in it, are my own. I confirm that:

- This work was done wholly or mainly while in candidature for a research degree at this university.
- Where any part of this thesis has previously been submitted for a degree or any other qualification at this university or any other institution, this has been clearly stated.
- Where I have consulted the published work of others, this is always clearly attributed.
- Where I have quoted from the work of others, the source is always given.
- With the exception of such quotations, this thesis is entirely my own work.
- I have acknowledged all main sources of help.
- Where the thesis is based on work done by myself, jointly with others, I have made clear exactly what was done by others and what I have contributed myself.

Date:

Nidhi Saxena
(2014REC9027)

Prof. Kamalesh Kumar Sharma
Professor
Department of Electronics And Communication Engineering
Malaviya National Institute of Technology Jaipur
J.L.N. Marg, Jaipur – 302017
INDIA

CERTIFICATE

This is to certify that the thesis entitled "**New Image Fusion Schemes using Hilbert Vibration Decomposition (HVD), Fractional Fourier Transform (FRFT) and Graph Signal Processing (GSP) Techniques**" being submitted by **Nidhi Saxena** (2014REC9027) is a bonafide research work carried out under my supervision and guidance in fulfillment of the requirement for the award of the degree of **Doctor of Philosophy** in the **Department of Electronics and Communication Engineering**, Malaviya National Institute of Technology, Jaipur, India. The matter embodied in this thesis is original and has not been submitted to any other University or institute for the award of any other degree.

Place:
Date:

Prof. Kamalesh Kumar Sharma
Professor
Dept. of ECE
MNIT, Jaipur

ACKNOWLEDGEMENT

First and above all, I praise God, the almighty for providing me this opportunity and granting me wisdom, health and strength to undertake this research work and complete it successfully. I could never have accomplished this without the faith I have in the almighty. Although the work described here was performed independently, it would not have been possible without the help and support of many wonderful peoples. I would therefore like to offer my sincere thanks to them.

I am extremely grateful to my supervisor **Prof. Kamalesh Kumar Sharma** for his valuable guidance, scholarly inputs and consistent encouragement throughout the research work. Completion of this doctoral work was possible only because of his unconditional support. He always made himself available to clarify my doubts despite of his busy schedules. His guidance, fruitful discussions, keen interest and dedication in the research motivated me to shape my research direction. I greatly appreciate his efforts for making my research work focused to achieve goal. His achievements, his work ethics, and his keen eye for every important detail have been an inspiration throughout all the years I have worked with him. Thank you sir for the patience you had to supervise and direct my work, I consider it as a great opportunity to do my doctoral programme under his guidance and to learn from his research expertise.

I express my sincere gratitude to DREC members, **Dr. Mohammed Saleem, Dr. Ghanshyam Singh** and **Dr. S. J. Nanda** for their valuable suggestions during my research work and semester end presentations. I also extend my deep sense of gratitude to **Prof. Udaykumar R Yaragatti**, Director, MNIT, Jaipur and Dean Academics **Prof. Khaleequr Rehman Niazi** for strengthening the research environment of institute by providing all necessary facilities to research scholars and all other faculties who directly or indirectly helped me throughout my time at MNIT. I would like to thank administrative and technical staff members of MNIT who have been kind enough to advise and help me in their respective roles.

A lot of credit also goes to my colleagues **Ms. Pulak Avinashi, Ms. Urvashi Shukla and Ms. Rachna Gupta** for their incessant and untiring support.

I am deeply thankful to my entire family for their love and support. Words cannot express how grateful I am to my mother, father, mother-in law, and my father-in-law for all of the sacrifices that you have made on my behalf. Your prayer for me was what sustained me thus far. I acknowledge my entire family for providing me healthy educated atmosphere in our family. This last word of acknowledgment I have saved for my dear husband **Mr. Gaurav Saxena**, who has been with me all these years and has made them the best years of my life. I always fall short of words and felt impossible to describe his support in words. Without your unconditional supports and encouragements, I could not have finished this work, it was you who kept the fundamental of our family, and I understand it was difficult for you. I see myself unable to even express my feelings about the love and patience that I observed from you. I can just say thanks for everything and may God give you all the best in return. Last, I would like to thank my son, **Krishna Saxena** who made these years unforgettable and enjoyable.

(Nidhi Saxena)

ABSTRACT

Imaging sensors are a valuable resource in today's world. Further, a single sensor cannot provide complete information about the environment in many applications. The role of image fusion in current image processing systems is increasing due to the growing variety of image acquisition techniques. Image Fusion is the process of combining substantial information from several sensors using mathematical techniques to create a single composite image that will be more comprehensive and thus, more useful for a human operator or other computer vision tasks. Latest technology in imaging sensors provides a broad kind of information that may be extracted from a located scene. Images which have been captured using different sensor modalities reveal numerous characteristics, such as the form of degradation, salient features, texture properties and many others. The automated procedure of conveying all the meaningful information from the input sensors to a final composite image is the goal of a fusion system, which appears to be an essential preprocessing stage for many applications, such as aerial and satellite imaging, medical imaging, robot vision and vehicle or robot guidance. The basic purpose of the image fusion or pansharpening methods is to improve the spatial quality and reduce the spectral distortion in the fused image. Some of the schemes achieve this objective by performing filtering in the time domain or joint time-frequency domains.

The objective of present research work is to develop efficient techniques for improving the spatial and spectral quality of the fused image. For attaining these objectives, image fusion/pansharpening algorithms are developed using three techniques-Hilbert vibration decomposition (HVD), fractional Fourier transforms (FRFT) and graph signal processing (GSP).

Initially, the HVD technique is used for developing the three new image fusion/pansharpening schemes for improving the spatial and spectral quality of the fused image. These proposed techniques are closer to the filtering based approaches

used in the many of the existing image fusion/pansharpening schemes. The HVD decomposes a wideband input signal into many signals in the decreasing order of the energy in terms of instantaneous amplitude and frequency components. The instantaneous amplitude of the first signal in a decomposition obtained through the HVD is similar in shape to the lowpass filtered version of a signal. This lowpass signal obtained through the HVD happens to be the highest energy component of the original signal, and it is instantaneous frequency-based lowpass filtering of the signal. On the other hand, the output signal obtained through the conventional lowpass filtering does not take the energy of the input/output signal into account and is based on the frequency content of the input signal only. This signal energy dependent and instantaneous frequency, based filtering are the main advantages of the HVD over conventional lowpass filtering based image fusion/pansharpening approaches. In the HVD based pansharpening schemes, the filtered signal of the panchromatic (PAN) and multispectral (MS) images used for increasing the spatial information to MS images. The tuning factor of the pansharpening model is optimized using particle swarm optimization (PSO) technique. The criteria chosen for optimization are the minimization of relative dimensionless global error (ERGAS) which essentially is a measure of spatial distortion between MS and fused image. In the HVD based image fusion scheme, the HVD decomposes the source images into instantaneous amplitude and frequency components. Amplitude components of the first and second signals in the decomposition of the original images are used to generate the fused images. Performance evaluation of fused images is done by computing fusion quality metrics, and the fusion results are compared with other existing fusion schemes. It is seen that the performance of the proposed schemes is better as compared to the existing fusion schemes.

The initial stage is followed by implication of second intermediate FRFT technique. Using 2D-discrete FRFT (2D-DFRFT) three novel image fusion/ pansharpening approaches are proposed, which improves the spatial and spectral quality of the fused image. The 2D-DFRFT is a generalized version of the conventional Fourier transform which provides the representation of a given signal

in intermediate domains between spatial and fast Fourier transform (FFT) domains. The angle parameters associated with the 2D-DFRFT provide additional degrees of freedom. Smaller values of angle parameters of a signal are similar in shape to the low pass filtered version of a signal, and hence it can be considered as fractional domain filtering of the signal. The 2D-DFRFT provides different representations of the given signal/image corresponding to different angles which can be optimized for better results. In the 2D-DFRFT based proposed pansharpening schemes, fractional domain filtered signal of the PAN image used for adding the spatial information to the MS images for pansharpening purpose similar to other MRA based approaches. The angle parameters associated with the 2D-DFRFT provide additional degrees of freedom which are optimized by a single objective PSO algorithm for finding better pansharpening results. In the 2D-DFRFT based image fusion scheme, input source images are transformed using 2D-DFRFT and then subtracted from the respective source images to obtain the detailed images. The detailed images are further used to generate the fused image using an appropriate fusion rule. The additional degree of freedom in terms of its angle parameters associated with the 2D-DFRFT exploited for obtaining better results in the proposed fusion scheme. It is observed that the proposed image fusion/pansharpening schemes provide improved spectral and spatial quality as compared to the existing schemes. The effects of aliasing and mis-registration errors on the proposed pansharpening methods are also investigated and compared with existing pansharpening methods. It is seen that the proposed methods are robust against aliasing and mis-registration errors.

The intermediate technique followed by the implication of third and last technique GSP/spectral graph wavelet filterbank (SGWF). Using the multistage multichannel SGWF, two new image fusion/pansharpening approaches are proposed. In the SGWF based proposed pansharpening method, the PAN image decomposed by the multistage M-channel SGWF, and then the weighted combination of lowpass component signals in the multistage SGWF decomposition is used to generate the pansharpened image using appropriate pansharpening rule. Simulation results of the proposed technique using different wavelets such as spline

wavelet (SW), Mexican-hat wavelet (MHW), Meyer wavelet (MW) and simple tight frame wavelet (SPW) are also presented and compared with existing pansharpening methods in terms of both visual perception and objective metrics such as Q-index (Q4), spectral angle mapper (SAM), relative dimensionless global error (ERGAS) and quality with-no reference (QNR). It is observed that the proposed pansharpening scheme provides better pansharpening results using MHW filterbank as compared to some of the existing schemes. In the proposed SGWF based image fusion scheme, lowpass signal generated from multistage multichannel of SGWF decomposition is used to add additional information in the source images using fusion rule. Performance evaluation of fused image is done by computing fusion quality metrics, and the fusion results are compared with other existing fusion schemes. It is seen that performance of the proposed schemes is better as compared to the existing fusion schemes.

In a nutshell, the present research work investigates image fusion/ pansharpening schemes to develop efficient techniques for improving the spatial quality and reducing the spectral distortion in the fused image. We demonstrate application of the HVD, FRFT and GSP techniques in image fusion/pansharpening schemes. The comparative analysis of the simulation results shows that the GSP based proposed image fusion/pansharpening scheme provides better simulation results as compared to the HVD and FRFT based image fusion/pansharpening schemes.

Contents

Declaration iii

Certificate iv

Acknowledgements v

Abstract vii

Contents xi

List of Figures xv

List of Tables xix

Abbreviations xxi

Symbols xxv

1 Introduction 1

1.1 Applications of Image Fusion . . . 2
1.2 Image Registration . . . 5
1.3 Performance Parameters . . . 7
1.3.1 Quantitative Assessment of Remote Sensing Image Fusion . . . 10
1.3.1.1 Degraded Scale Assessment . . . 10
1.3.1.2 Full Scale Assessment . . . 12
1.4 Challenges of the Image Fusion Schemes . . . 13
1.5 Motivation . . . 13
1.6 Problem Statement . . . 15
1.7 Thesis Contribution . . . 15
1.8 Organization of Thesis . . . 16

2 Literature Review **19**
2.1 Classification of Image Fusion and Pansharpening Techniques with Explanation 20
2.2 Summary of the Survey 33

3 Hilbert Vibration Decomposition Based Image Fusion/Pansharpening Schemes **39**
3.1 Introduction 40
3.2 Overview of HVD 41
3.3 Proposed Pansharpening Scheme-I 43
3.3.1 Simulation Results 47
3.4 Proposed Pansharpening Scheme-II 58
3.4.1 Simulation Results 61
3.5 Proposed Image Fusion Scheme 63
3.5.1 Simulation Results 66
3.6 Conclusions 72

4 Fractional Fourier Transform Based Image Fusion/Pansharpening Schemes **75**
4.1 Introduction 76
4.2 Review of FRFT and PSO 77
4.2.1 FRFT 77
4.2.2 PSO 79
4.3 Proposed Pansharpening Scheme-I 80
4.3.1 Simulation Results 85
4.4 Proposed Pansharpening Scheme-II 92
4.4.1 Simulation Results 96
4.5 Proposed Image Fusion Scheme using FRFT 104
4.5.1 Simulation Results 106
4.6 Conclustions 112

5 Graph Signal Processing Based Image Fusion/Pansharpening Schemes **115**
5.1 Introduction 116
5.2 Review of SGWF 117
5.3 Spectral Graph Wavelet Filterbank Based Proposed Pansharpening Algorithm . 119
5.3.1 Simulation Results 122
5.4 Proposed image fusion scheme 129
5.4.1 Simulation Results 130
5.5 Comparison of the Proposed Schemes 136
5.5.1 Pansharpening Schemes 136
5.5.2 Image Fusion Schemes 138
5.6 Conclusions 142

6 Conclusions and Future Scope **145**
6.1 Summary of the Significant Findings 146
6.2 Future Scope of the Research Work 148

Bibliography **149**

Publications **175**

List of Figures

1.1 For IKONOS image satellite dataset (a) PAN image, (b) MS image, (c) Pansharpened image. . . . 3
1.2 (a) MMW, (b) visible source images and (c) fused image . . . 4
1.3 (a) MRI, (b) CT source images and (c) fused image . . . 4
1.4 (a) and (b) Multi-focus clock source images, (c) fused image . . . 5
1.5 (a) IR, (b) visible source images and (c) fused image . . . 6

3.1 Block diagram of the HVD method . . . 42
3.2 (a) Rectangular pulse, (b) Hilbert vibration decomposition of rectangular pulse and (c) Low pass filtering of rectangular pulse, . . . 44
3.3 Block diagram of the proposed pansharpening scheme-I . . . 45
3.4 PAN and EXP images for Pleiades, IKONOS and GeoEye-1 satellite datasets are (a) and (b), (c) and (d), (e) and (f) respectively. . . . 48
3.5 Pansharpened images using different pansharpening methods for Pleiades satellite dataset are (a) Proposed HVD_F1 ($\alpha = 0.6628$), (b) OMF, (c) AIHS, (d) Indusion, (e) ATWTM2 and (f) MTF-GLP methods. . . . 49
3.6 Pansharpened images using different pansharpening methods for IKONOS satellite dataset are (a) Proposed HVD_F1 ($\alpha = 0.4972$), (b) OMF, (c) AIHS, (d) Indusion, (e) ATWTM2 and (f) MTF-GLP methods. . . . 50
3.7 Pansharpened images using different pansharpening methods for GeoEye-1 satellite dataset are (a) Proposed HVD_F1 ($\alpha = 0.4564$), (b) OMF, (c) AIHS, (d) Indusion, (e) ATWTM2 and (f) MTF-GLP methods. . . . 51
3.8 Quality/distortion indexes for increasing amounts of aliasing, measured by the amplitude at nyquist frequency of the Gaussian-like low-pass filter simulating the modulation transfer functions of the multispectral instrument using image Fig.3.6. . . . 54
3.9 Quality/distortion indexes for increasing amounts of misregistration between MS and PAN images. Misregistration is measured in meters (32m=2 pels for IKONOS MS data at degraded spatial scale) using image Fig.3.6. . . . 55
3.10 Pansharpened images for GeoEye-1 satellite dataset using (a) Proposed HVD_F1 ($\alpha = 0.4564$), (b) GLF and (c) DWT. . . . 56

3.11 Pansharpened images using different pansharpening methods for AVIRIS HS satellite dataset are (a) Reference image, (b) EXP image, (c) Proposed HVD_F1 ($\alpha = 0.6$), (d) GS, (e) PCA and (f) GFPCA methods. 57
3.12 Block diagram of the proposed pansharpening scheme-II 59
3.13 Pansharpened images obtained using proposed and existing pansharpening methods for GeoEye-1 satellite dataset are (a) Proposed HVD_F2, (b) HVD_F1, (c) OMF, (d) AIHS, (e) Indusion, (f) ATWTM2 methods. 61
3.14 Block diagram of the proposed fusion scheme 64
3.15 (a) MMW and (b) visible source images, fused image obtained by the (c) Proposed HVD_FS1, (d) Proposed HVD_FS2, (e) ASR and (f) DCHWT schemes . 67
3.16 (a) IR and (b) visible source images, fused image obtained by the (c) Proposed HVD_FS1, (d) Proposed HVD_FS2, (e) ASR and (f) DCHWT schemes 67
3.17 (a) MRI and (b) CT source images, fused images obtained by the (c) Proposed HVD_FS1, (d) Proposed HVD_FS2, (e) ASR and (f) DCHWT schemes 68
3.18 (a) and (b) Multi-focus Book source images, fused images obtained by the (c) Proposed HVD_FS1, (d) Proposed HVD_FS2, (e) ASR and (f) DCHWT schemes 68
3.19 (a) and (b) Multi-focus Clock source images, fused images obtained by the (c) Proposed HVD_FS1, (d) Proposed HVD_FS2, (e) ASR and (f) DCHWT schemes 69

4.1 Time-frequency plane and a set of coordinates (u, v) rotated by an angles α and β relative to the original coordinates (u', v'). 78
4.2 (a) Rectangular pulse, (b) Fractional Fourier transform of rectangular pulse, (c) Low pass filtering of rectangular pulse 81
4.3 Block diagram of the proposed panshapening scheme 82
4.4 For IKONOS satellite dataset obtained the pansharpened images using proposed and existing pansharpening schemes are (a) Proposed 2D-DFRFT_F1, (b) OMF, (c) AIHS, (d) indusion, (e) ATWTM2 and (f) MTF-PP schemes. . . . 86
4.5 For GeoEye-1 satellite dataset obtained the pansharpened images using proposed and existing pansharpening schemes are (a) Proposed 2D-DFRFT_F1, (b) OMF, (c) AIHS, (d) indusion, (e) ATWTM2 and (f) MTF-PP schemes. . . . 87
4.6 Convergence plot (ERGAS versus number of iterations) of PSO in the proposed pansharpening scheme for (a) IKONOS and (b) Geoeye-1 satellite images. . . . 88
4.7 Quality/distortion indices for increasing amounts of (a) aliasing, measured by the amplitude at nyquist frequency of the Gaussian-like low-pass filter simulating the modulation transfer functions of the multispectral instrument, (b) misregistration between MS and PAN images using image shown in Fig.4.4. . . 90
4.8 For GeoEye-1 satellite dataset (a) Filtered PAN (P) image using 2D-DFRFT, (b) Spatial details extracted from PAN (P) image using 2D-DFRFT, (c) Pansharpened image using 2D-DFRFT, (d) filtered PAN image using GLF, (e) Spatial details extracted from PAN image using GLF, (f) Pansharpened image using GLF. 91

4.9 Block diagram of the proposed panshapening method 93
4.10 Spatial information image I''_{α_1,β_1} for IKONOS satellite dataset at different values of angle parameters of the 2D-DFRFT are (a) α_1=β_1=$0.94\pi/2$, (b) α_1=β_1=$0.96\pi/2$, (c) α_1=β_1=$0.98\pi/2$, (d) α_1=β_1=$1\pi/2$, (e) α_1=β_1=$1.02\pi/2$, (f) α_1=β_1=$1.04\pi/2$. 98
4.11 Pansharpend images of the proposed scheme for IKONOS satellite dataset at different values of angle parameters of the 2D-DFRFT are (a) α_1=β_1=$0.94\pi/2$, (b) α_1=β_1=$0.96\pi/2$, (c) α_1=β_1=$0.98\pi/2$, (d) α_1=β_1=$1\pi/2$, (e) α_1=β_1=$1.02\pi/2$, (f) α_1=β_1=$1.04\pi/2$. 99
4.12 Pansharpened images using different pansharpening methods for IKONOS satellite dataset are (a) Proposed 2D-DFRFT_F2, (b) HVD_F1, (c) OMF (d) AIHS, (e) Indusion and (f) ATWTM2 methods. 100
4.13 Pansharpened images using different pansharpening methods for GeoEye-1 satellite dataset are (a) Proposed 2D-DFRFT_F2, (b) HVD_F1, (c) OMF (d) AIHS, (e) Indusion and (f) ATWTM2 methods. 101
4.14 Block diagram of the proposed fusion scheme 105
4.15 (a) MMW and (b) visible source images, fused image obtained by the (c) Proposed 2D-DFRFT, (d) ASR, (e) DCHWT and (f) CBF based schemes 107
4.16 (a) IR and (b) visible source images, fused image obtained by the (c) Proposed 2D-DFRFT, (d) ASR, (e) DCHWT and (f) CBF based schemes 108
4.17 (a) MRI and (b) CT source images, fused image obtained by the (c) Proposed 2D-DFRFT, (d) ASR, (e) DCHWT and (f) CBF based schemes 108
4.18 (a) and (b) Multi-focus Book source images, fused image obtained by the (c) Proposed 2D-DFRFT, (d) ASR, (e) DCHWT and (f) CBF based schemes . . . 109
4.19 (a) and (b) Multi-focus Clock source images, fused image obtained by the (c) Proposed 2D-DFRFT, (d) ASR, (e) DCHWT and (f) CBF based schemes . . . 109

5.1 Critically sampled two-channel graph filterbank. 117
5.2 Block diagram of the proposed panshapening method 119
5.3 SGWF decomposition 120
5.4 Input images for GeoEye-1 satellite dataset are (a) PAN image, (b) EXP MS images. 122
5.5 The Spectral quality assessments of the pansharpened images obtained by the proposed method using multistage multichannel decomposition are (a) $M_2 = 2, M_3 = 0, M_4 = 0$, (b) $M_2 = 3, M_3 = 0, M_4 = 0$, (c) $M_2 = 4, M_3 = 0, M_4 = 0$, (d) $M_2 = 2, M_3 = 2, M_4 = 0$, (e) $M_2 = 2, M_3 = 3, M_4 = 0$, (f) $M_2 = 3, M_3 = 3, M_4 = 0$, (g) $M_2 = 3, M_3 = 4, M_4 = 0$, (h) $M_2 = 2, M_3 = 3, M_4 = 4$, (i) $M_2 = 2, M_3 = 2, M_4 = 2$, (j) $M_2 = 3, M_3 = 3, M_4 = 3$, (k) $M_2 = 4, M_3 = 4, M_4 = 4$. 123
5.6 Pansharpened images obtained by the proposed pansharpening scheme using different filterbanks (a) SWF, (b) MHWF, (c) MWF, (d) SPWF. 124

5.7 Pansharpened images obtained using proposed and existing pansharpening schemes (a) Proposed MHWF, (b) ATWT, (c) AWLP, (d) ATWTM2, (e) MTF-GLP, (f) GLP-PP, (g) GLP-HPM, (h) GLP-CBD. 125
5.8 Quality index (a) for increasing amounts of aliasing, measured by the amplitude at nyquist frequency of the Gaussian-like low-pass filter simulating the modulation transfer functions of the multispectral instrument, and (b) for increasing amounts of misregistration between MS and PAN images. 128
5.9 Block diagram of the proposed fusion scheme 129
5.10 (a) MMW and (b) visible source images, fused image obtained by the (c) Proposed MHWF, (d) ASR, (e) DCHWT and (f) CBF based schemes 131
5.11 (a) IR and (b) visible source images, fused image obtained by the (c) Proposed MHWF, (d) ASR, (e) DCHWT and (f) CBF based schemes 131
5.12 (a) MRI and (b) CT source images, fused image obtained by the (c) Proposed MHWF, (d) ASR, (e) DCHWT and (f) CBF based schemes 132
5.13 (a) and (b) Multi-focus Book source images, fused image obtained by the (c) Proposed MHWF, (d) ASR, (e) DCHWT and (f) CBF based schemes 132
5.14 (a) and (b) Multi-focus Clock source images, fused image obtained by the (c) Proposed MHWF, (d) ASR, (e) DCHWT and (f) CBF based schemes 133
5.15 Pansharpened images obtained for GeoEye-1 satellite dataset using proposed pansharpening schemes are (a) HVD_F1, (b) HVD_F2, (c) 2D-DFRFT_F1, (d) 2D-DFRFT_F2, (e) MHWF 136
5.16 (a) MMW and (b) visible source images, fused image obtained by the proposed schemes using (a) HVD_FS1, (b) 2D-DFRFT, (c) MHWF 138
5.17 (a) IR and (b) visible source images, fused image obtained by the proposed schemes using (a) HVD_FS1, (b) 2D-DFRFT, (c) MHWF 139
5.18 (a) MRI and (b) CT source images, fused image obtained by the proposed schemes using (a) HVD_FS1, (b) 2D-DFRFT, (c) MHWF 139
5.19 (a) and (b) Multi-focus Book source images, fused image obtained by the proposed schemes using (a) HVD_FS1, (b) 2D-DFRFT, (c) MHWF 139
5.20 (a) and (b) Multi-focus Clock source images, fused image obtained by the proposed schemes using (a) HVD_FS1, (b) 2D-DFRFT, (c) MHWF 140

List of Tables

3.1 The Spectral quality assessment of the pansharpened images for Pleiades data set ($\alpha = 0.6628$) . . . 52
3.2 The Spectral quality assessment of the pansharpened images for IKONOS data set ($\alpha = 0.4972$) . . . 53
3.3 The Spectral quality assessment of the pansharpened images for GeoEye-1 dataset ($\alpha = 0.4564$) . . . 53
3.4 The Spectral quality assessment of the pansharpened images for GeoEye-1 dataset ($\alpha = 0.4564$) . . . 56
3.5 The Spectral quality assessment of the pansharpened images for AVIRIS HS satellite dataset ($\alpha = 0.6$) . . . 58
3.6 The Spectral quality assessment of the pansharpened images for GeoEye-1 dataset 62
3.7 Performance comparison of fused images . . . 70
3.8 Performance comparison of fused images . . . 71

4.1 Parameter settings of PSO in the proposed pansharpening algorithm . . . 88
4.2 The Spectral quality assessment of the fused images for IKONOS dataset at degraded and full scale optimized 2D-DFRFT angle parameters $\alpha_1 = 0.0689\pi/2$ and $\beta_1 = 0.0710\pi/2$. . . . 89
4.3 The Spectral quality assessment of the fused images for GeoEye-1 dataset at degraded and full scale optimized 2D-DFRFT angle parameters $\alpha_1 = 0.0851\pi/2$ and $\beta_1 = 0.0991\pi/2$. . . . 90
4.4 The Spectral quality assessment of the pansharpened images for GeoEye-1 dataset 92
4.5 The quality assessment of the pansharpened images of the proposed scheme using different values of the angle parameters (α_1, β_1) of the 2D-DFRFT for IKONOS satellite dataset. . . . 97
4.6 The Spectral quality assessment of the pansharpened images for IKONOS dataset at degraded and full scale optimized 2D-DFRFT angle parameters $\alpha_1 = 0.98\pi/2$ and $\beta_1 = 0.98\pi/2$. . . . 102
4.7 The Spectral quality assessment of the pansharpened images for GeoEye-1 dataset at degraded and full scale optimized 2D-DFRFT angle parameters $\alpha_1 = 0.98\pi/2$ and $\beta_1 = 0.98\pi/2$. . . . 103

4.8 Performance comparison of fused images 110
4.9 Performance comparison of fused images 111

5.1 The quality assessment of the pansharpened images obatined using multistage multichannel decomposition at degraded scale. 126
5.2 The quality assessment of the pansharpened images obatined using different filterbanks at degraded and full scale. 126
5.3 The quality assessment of the pansharpened images using proposed and existing pansharpening schemes at degraded and full scale. 127
5.4 Performance comparison of fused images 134
5.5 Performance comparison of fused images 135
5.6 The quality assessment of the pansharpened image for proposed pansharpening schemes at degraded and full scale for GeoEye-1 satellite dataset 137
5.7 Performance comparison of fused images 140
5.8 Performance comparison of fused images 141

Abbreviations

FRFT	**Fractional Fourier Transform**
GSP	**Graph Signal Processing**
SGWF	**Spectral Graph Wavelet Filterbank**
PAN	**Panchromatic**
MS	**Multispectral**
PSO	**Partical Swarm Optimization**
ERGAS	**Relative Dimensionless Global Error**
SW	**Spline Wavelet**
MHW	**Mexican-hat wavelet**
MW	**Meyer Wavelet**
SPW	**Simple Tight Frame Wavelet**
Q4	**Q- index**
SAM	**Spectral Angle Mapper**
QNR	**Quality with No-Reference**
MSD	**Multiscale Decomposition**
MRA	**Multi-resolution Decomposition**
ANN	**Artificial Neural Networks**
EMD	**Empirical Mode Decomposition**
LDR	**Low Dynamic Range**
HDR	**High Dynamic Range**

BEMD	**Bi-Dimensional Empirical Mode Decomposition**
DCHWT	**Discrete Cosine Harmonic Wavelet Transforms**
CBF	**Cross Bilateral Filter**
HVD	**Hilbert Vibration Decomposition**
DSP	**Digital Signal Processing**
MRA	**Multi Resolution Analysis**
DWT	**Discrete Wavelet Transform**
DTCWT	**Dual Tree Complex Wavelet**
CT	**Computed Tomography**
MDCT	**Multiresolution Discrete Cosine Transform**
HWT	**Harmonic Wavelet Transform**
FT	**Fourier Transform**
FFT	**Fast Fourier transform**
DFT	**Discrete Fourier transform**
DCT	**Discrete Cosine Transform**
RGB	**Red Green Blue**
CS	**Component Substitution**
IHS	**Intensity Hue Saturation**
PCA	**Principal Component Analysis**
GS	**Gram Schmidt**
BT	**Brovey Transform**
IR	**Infrared**
MMW	**Millimeter Wave**
PET	**Positron Emission Tomography**
MRI	**Magnetic Resonance image**
FLIR	**Forward-looking infrared**
API	**Average Pixel Intensity**
SD	**Standard deviation**

AG	**Average Gradient**
H	**Entropy**
FS	**Fusion Symmetry**
MI	**Mutual Information**
CC	**Correlation Coefficient**
SF	**Spatial Frequency**
STFT	**Short Time Fourier Transform**
HT	**Hilbert Transform**
FIR	**Finite Impulse Response**
IIR	**Infinite Impulse Response**
HS	**Hyper-spectral**
OMF	**Optimal Filter**

Symbols

F	Fused Image
U and V	Source images
MI_{UF}	Mututal information between F and U images
MI_{VF}	Mututal information between F and V images
$Q^{UV/F}$	Amount of edge information from source images to fused image
$L^{UV/F}$	Amount of loss edge information from source images to fused image
$N^{UV/F}$	Amount of Noise or artifacts added in fused image
D_λ	Spectral distortion
D_S	Spatial distortion
$\widetilde{MS}_r$	rth MS images interpolated at the scale of PAN image
I	Intensity image
G_r	Injection coefficients
MS_r	MS image
$\widehat{MS}_r$	Pansharpened MS image
α, β, γ	Tunning factors
P	PAN image
N	Number of bands in the MS images
P_{hvd}	HVD of PAN image
$\hat{I}_{\alpha_1,\beta_1}$	Magnitude of the 2D-DFRFT domain representation of image I
$\hat{P}_{\alpha_1,\beta_1}$	Magnitude of the 2D-DFRFT domain representation of image P

$\overline{MS}_{r(\alpha_1,\beta_1)}$	Pansharpened image applied at the degraded scale
(I_{hvd_1})	HVD of the Intensity Image
UV	Maximum selection rule applied on U and V images
I_{α_1,β_1}	Highpass filtered $\hat{I}_{\alpha_1,\beta_1}$ image
P_{α_1,β_1}	Highpass filtered $\hat{P}_{\alpha_1,\beta_1}$ image
I'_{α_1,β_1}	2D-IDFRFT domain representation of filtered image I_{α_1,β_1}
P'_{α_1,β_1}	2D-IDFRFT domain representation of filtered image P_{α_1,β_1}
P_L	Output image after the SGWF decomposition
$K-1$	Total stages in the SGWF decomposition
M_{k+1}	Number of channels at kth stage in the SGWF decomposition.

Chapter 1

Introduction

Image fusion is a well-recognized and a conventional field of image processing. It is designed to combine multiple input images into a fused image, which is expected to be more informative for human or machine perception as compared to any of the input images. The main objective of any image fusion is to improve the visual appearance, increase reliability, give robust system performance, provide compact representation of information in different applications like medical imaging [1], remote sensing [2], biometrics [3] and military [4] etc. Many applications that require analysis of two or more images of a scene have benefited from image fusion. For instance, in remote sensing applications, the synthesis of a low resolution multispectral (MS) image and a high resolution panchromatic (PAN) images are used to obtain a fused/pansharpened image for achieving the goal of high spatial and spectral resolution in a single image, many pansharpening schemes have been proposed [5, 6, 7]. The pansharpening scheme refers to the fusion of information derived from PAN and MS images captured simultaneously over the same area [7, 8]. In medical imaging applications, images from multiple modalities can be fused together for a more reliable and accurate medical diagnosis. In surveillance applications, image fusion can fuse the information across the electromagnetic spectrum, (e.g., visible and infrared band) for night vision. In response to the requirements in real applications, the researchers

have been very active in proposing more effective image fusion methods. The advancement in the image fusion can be attributed to the evolution of various signal processing and analysis theory techniques which include multi-scale decompositions (MSD) [9] , multi-resolution analysis (MRA) [10], intensity hue saturation (IHS) [11], principal component analysis (PCA) [12], dictionary learning [13], Brovey transform [6], hybrid methods [14], transform domain methods [15] and methods in other domains. In the beginning, in 1997, a general introduction to image fusion in the multisensor domain was given by Hall and Llinas [16]. In [17] Zhang and Blum gave a set of image fusion methods based on multi-scale decomposition. Then, providing a complete edge over multi-scale decomposition methods, the advantageous multi-resolution properties of wavelet transform made them extremely popular in image processing [18, 19]. To maintain the directional features of the images, the wavelet transform was further improvised in the form of discrete wavelet transform [20]. Wavelet decomposition is a widespread method used for image fusion [21]. Wavelet decomposition uses basis functions or different filters that are fixed and create influence in the fused image. In [21], the wavelet transforms experience problems when analyzing high frequency content, thus tending to lose spatial information. The artificial neural networks (ANN) and image blocking algorithms have also been exploited in terms of image fusion [22]. The Shearlet and counterlet transform have been very efficiently used in non-sub-sampled domain in the context of image fusion [23, 24]. Along with developing mathematical tools and fusion rules, the image fusion methods are continually being renewing.

1.1 Applications of Image Fusion

In recent years, image fusion has been attracting a large amount of attention in a wide variety of applications such as concealed weapon detection (CWD), remote sensing, medical diagnosis and military surveillance. Some applications of image fusion are given below:

- In the remote sensing application using image fusion/pansharpening improves the spectral and spatial resolution of the fused image. Fig. 1.1(a) shows a high spatial resolution panchromatic (PAN) image. Fig. 1.1(b) shows a low spatial resolution multispectral (MS) image of the same scene. Using image fusion or pansharpening, we can obtain a high resolution MS image which combines the spectral characteristic of the low-resolution MS image with the spatial resolution of the PAN image, as shown in Fig. 1.1(c).

(a) (b) (c)

FIGURE 1.1: For IKONOS image satellite dataset (a) PAN image, (b) MS image, (c) Pansharpened image.

- Concealed weapon detection (CWD) application is an important topic in the general area of law enforcement, and it appears to be a critical technology for dealing with terrorism, which seems to be the most significant law enforcement problem for the next decade. Since no single sensor technology can provide acceptable performance in CWD applications, image fusion has been identified as a key technology to achieve improved CWD procedures. Fig. 1.2 shows a pair of visual and 94 GHz MMW images. The visual image provides the outline and the appearance of the people while the MMW image shows the existence of a gun. From the fused image, there is considerable evidence to suspect that the person on the right has a concealed gun underneath his clothes.

- Medical diagnosis application, medical imaging has a positron emission tomography (PET) and a magnetic resonance image (MRI) from the brain of the same patient. The

(a) (b) (c)

FIGURE 1.2: (a) MMW, (b) visible source images and (c) fused image

first is a functional image displaying the brain activity, but without anatomical information, while the second provides anatomical information but without functional activity. Moreover, although the two images come exactly from the same brain area, the PET has less pixels than the MRI, i.e. we can say that the first has less spatial resolution than the second. The goal of fusion scheme for the proposed example is to achieve a unique image with functional and anatomical information with the best resolution [25, 26, 27]. Fig. 1.3 shows an example of MRI and computed tomography (CT) image fusion.

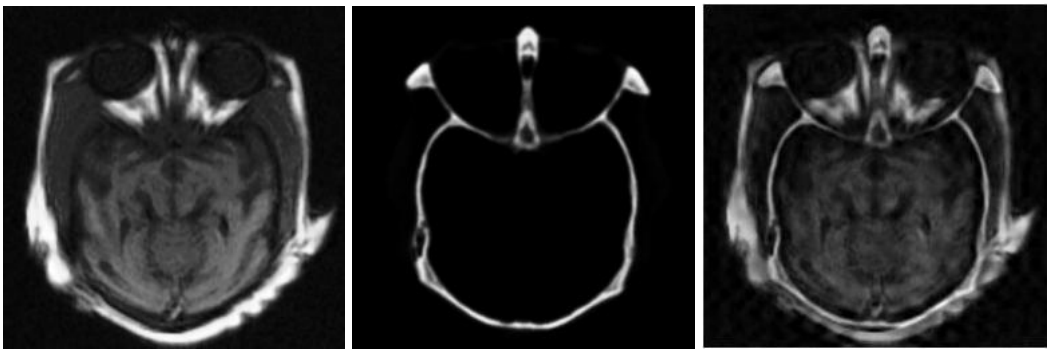

(a) (b) (c)

FIGURE 1.3: (a) MRI, (b) CT source images and (c) fused image

- Multifocus image fusion application is useful to enhance digital camera images. Inexpensive cameras may have difficulty in obtaining images which are in-focus everywhere in some situations due to the limited depth-of-focus of the employed lenses. To overcome

this problem, we can take several images with different focus points and combine them together into a single composite image using fusion. Fig. 1.4 shows a pair of digital camera images. In one image, the focus is on the left clock. In the other image, the focus is on the right clock. In the fused image, both the clocks are in focus.

(a) (b) (c)

FIGURE 1.4: (a) and (b) Multi-focus clock source images, (c) fused image

- Military surveillance application is a head-tracked vision system for night vision applications. The multiple imaging sensors employed can enhance a driver's overall situational awareness. Fig. 1.5 shows a scene captured by the head-tracked vision system during a field exercise. This scene includes a person, a road, a house, grass, and trees. Fig. 1.5(a) shows the corresponding thermal imaging forward-looking-infrared (FLIR) sensor image of the scene and Fig. 1.5(b) shows the image intensified charged coupled device (IICCD)/visual sensor image of the same scene. These images contain complementary features as illustrated by the fused image shown in Fig. 1.5(c).

1.2 Image Registration

Image registration is an essential part of image fusion. In a majority of image fusion research, it is assumed that the source images are perfectly aligned. In fact, this is difficult to achieve

(a) (b) (c)

FIGURE 1.5: (a) IR, (b) visible source images and (c) fused image

in many practical situations. The task of image registration is to align the reference images to one another images. During the image fusion process, it is difficult to align the images. It is overcome, by insuring the accurate registration between source images during preprocessing of image fusion. Over the years, a broad range of techniques have been developed for various types of sensors and applications. There are two general types of differences between the images to be registered. The first type is due to changes in acquisition, which cause the images be spatially misaligned. In the second type, the difference cannot be modeled by a spatial transform alone. The differences which are not due to spatial misalignment can be attributed to factors such as lighting changes, using different types of sensors, using similar sensors but with different parameters, object movements, or scene changes. Registration will not remove the differences which are not due to spatial misalignment, but they make the registration more difficult as there is no longer an exact match between two images, even after spatial transformation. Existing image registration techniques can be classified into two categories: intensity-based methods, and feature-based methods. In the intensity-based methods, the images are essentially registered by selecting many windows in high-variance areas of one image, locating the corresponding windows in the other image, and using the window geometric centers or mass centers as control points to determine the registration parameters. Feature-based methods extract and match the common features from the source images. Frequently used features include edges, corners, and contours. The feature-based approach has received more attention for the

purpose of multisensor image registration.

1.3 Performance Parameters

Performance parameters [28, 29], [30] are used to compare the effectiveness of the fusion scheme which are discussed below.

- Average Pixel Intensity (API) or mean ($\bar{F}$) calculate the contrast level in the image is given by [28, 29]

$$API = \bar{F} = \frac{1}{MN}\sum_{m=1}^{M}\sum_{n=1}^{N} F(m,n), \tag{1.1}$$

  where $F(m,n)$ is pixel intensity at (m,n) and $M \times N$ is the image size.

- Standard Deviation (SD) is the square root of the variance which reflects the spread in data. Standard deviation measures the contrast in the fused image. An image with high contrast would have a high standard deviation and is given by [28, 29]

$$SD = \frac{1}{\sqrt{MN}}\sqrt{\sum_{m=1}^{M}\sum_{n=1}^{N}(F(m,n)-\bar{F})^2}, \tag{1.2}$$

- Average gradient (AG) measures the degree of clarity and sharpness and is given by [28, 29]

$$AG = \frac{1}{MN}\sum_{m=1}^{M}\sum_{n=1}^{N}\sqrt{(F(m,n)-F(m+1,n))^2+(F(m,n)-F(m,n+1))^2}, \tag{1.3}$$

- Entropy (H) estimates the amount of information present in the image. A higher value of entropy implies that the fused image is better than the reference image and is given by

[28, 29]

$$H = -\sum_{k=0}^{255} p_k \log_2 (p_k), \tag{1.4}$$

where p_k is the probability of intensity value k in an 8-bit image.

- Mutual information (MI) is used to measure the similarity of image intensity between the fused and source images [29], which is given by

$$MI = MI_{UF} + MI_{VF}, \tag{1.5}$$

where $MI_{UF} = \sum_k \sum_l p_{U,F(k,l)} \log_2 \left(\frac{p_{U,F(k,l)}}{p_{U(k)} p_{F(k)}} \right)$ is the mutual information between source image U and fused image F, and $MI_{VF} = \sum_k \sum_l p_{V,F(k,l)} \log_2 \left(\frac{p_{V,F(k,l)}}{p_{V(k)} p_{F(k)}} \right)$ is the mutual information between source image V and fused image F.

- Information symmetry or fusion symmetry (FS) is an indication of how symmetric the output image is with the input image. If the final fused image is equally symmetric to both the source images, value of fusion symmetry will be closer to 2 and the quality of fusion will be better and is given by [28, 29]

$$FS = 2 - |\frac{MI_{UF}}{MI} - 0.5| \tag{1.6}$$

- Correlation coefficient (CC) measures the relevance of fused image to source images. The value of CC should be close to +1, which indicates that the reference and fused images are same. Variation increases when the value of CC is less than 1 and is given by [28, 29]

$$CC = (r_{UF} + r_{VF})/2, \tag{1.7}$$

where

$r_{UF} = \frac{\sum_m \sum_n \left(U(m,n) - \bar{U}\right)\left(F(m,n) - \bar{F}\right)}{\sqrt{\left(\sum_m \sum_n \left(U(m,n) - \bar{U}\right)^2\right)\left(\sum_m \sum_n \left(F(m,n) - \bar{F}\right)^2\right)}}$ and

$r_{VF} = \frac{\sum_m \sum_n \left(V(m,n) - \bar{V}\right)\left(F(m,n) - \bar{F}\right)}{\sqrt{\left(\sum_m \sum_n \left(V(m,n) - \bar{V}\right)^2\right)\left(\sum_m \sum_n \left(F(m,n) - \bar{F}\right)^2\right)}}$,

- Spatial frequency (SF) is computed by calculating the row frequency and column frequency of the fused image. Higher value of SF indicates that the input images and the fused image are similar and is computed as [28, 29]

$$SF = \sqrt{RF^2 + CF^2}, \tag{1.8}$$

where $RF = \sqrt{\frac{1}{mn}(\sum_m \sum_n (F(m,n) - F(m,n-1))^2)}$ and
$CF = \sqrt{\frac{1}{mn}(\sum_m \sum_n (F(m,n) - F(m-1,n))^2)}$

- $Q^{UV/F}$ [30], metric measures the amount of edge information from source images to fused image, and is given by [30]

$$Q^{UV/F} = \frac{\sum_{m=1}^{M} \sum_{n=1}^{N} (Q^{UF}(m,n) w^U(m,n) + (Q^{VF}(m,n) w^V(m,n))}{\sum_{m=1}^{M} \sum_{n=1}^{N} (w^U(m,n) + w^V(m,n))}, \tag{1.9}$$

where Q^{UF} indicates the similarity between two images U and F in terms of width and direction of edge and $Q^{VF}(m,n)$ indicates the similarity between two images V and F in terms of width and direction of edge. The closer the value to 1, the higher the quality of the composite image.

- $L^{UV/F}$ [30], metric measures the amount of loss edge information from source images to fused image.

- $N^{UV/F}$ [30], metric measures the amount of Noise or artifacts added in fused image due to fusion process.

It is to be noted that total fusion performance Q^{UF}, fusion loss $L^{UV/F}$ and fusion artifacts $N^{UV/F}$ are complimentary indicating that the sum of all these should result in unity.

$$Q^{UV/F} + L^{UV/F} + N^{UV/F} = 1 \tag{1.10}$$

1.3.1 Quantitative Assessment of Remote Sensing Image Fusion

Accurate quantitative assessment is difficult when a reference high-resolution MS image does not exist in remote sensing fusion applications. However some metrics have been in use to measure the quantitative quality of fused images using with or without the reference image. The quality metrics generally provide two types of assessment: (i) Degraded scale assessment, (ii) Full scale assessment.

1.3.1.1 Degraded Scale Assessment

As per Wald's protocol [31] the PAN and MS images are degraded to a lower resolution to compare the fused image with the reference original MS image [32]. Therefore the PAN image is degraded in resolution such that the resulting pansharpening image has the same size as MS image and used as a reference.

- The Universal Image Quality Index (UIQI) or Q-index [33], measures the degree of linear correlation, closeness of the mean luminance and the contrasts of the images M_r and F_r. It is given by [33]

$$Q(M_r, F_r) = \frac{\sigma_{M_r F_r}}{\sigma_{M_r}\sigma_{F_r}} \frac{2\bar{M}_r\bar{F}_r}{(\bar{M}_r)^2 + (\bar{F}_r)^2} \frac{2\sigma_{M_r}\sigma_{F_r}}{(\sigma_{M_r})^2 + (\sigma_{F_r})^2}, \tag{1.11}$$

  where $\sigma_{M_r F_r}$ is the sample covariance of M_r and F_r, $\bar{M}_r$ and $\bar{F}_r$ are the sample mean of M_r and F_r respectively. The Q-index varies in the range [-1, 1], with 1 denoting the best fidelity to reference [33].

- The Spectral Angle Mapper (SAM) [34] index determines the spectral similarity between two spectral vectors as a spectral angle and it is given by [34]

$$SAM(M_{\{r\}}, F_{\{r\}}) = arccos(\frac{\langle M_{\{r\}}, F_{\{r\}}\rangle}{\|M_{\{r\}}\|.\|F_{\{r\}}\|}), \tag{1.12}$$

where $M_{\{r\}} = [M_{1,\{r\}}, M_{2,\{r\}}, ..., M_{N,\{r\}})]$ and $F_{\{r\}} = [F_{1,\{r\}}, F_{2,\{r\}}, ..., F_{N,\{r\}})]$ are the two pixel vectors of the input MS image and fused image respectively, and SAM value for the whole image is obtained by averaging the single measures over all the pixels. The optimal value of the SAM index is zero [34].

- The relative dimensionless global error in synthesis (ERGAS) is a normalized version of root mean square error (RMSE) designed to calculate the spatial distortion [31] and is expressed as

$$ERGAS = 100\frac{h}{l}\sqrt{\frac{1}{N}\sum_{r=1}^{N}(\frac{RMSE(M_r, F_r)}{\mu(M_r)})^2}, r = 1, 2, ..., N, \tag{1.13}$$

where, h/l is the ratio of resolution of PAN and MS images, $\mu(r)$ is the mean of the rth band. It is used to compute the quality of fused image in terms of normalized average error of each band of processed image [31]. Increase in the value of ERGAS indicates distortion in the fused image, lower value of ERGAS indicates that the fused image is similar to the reference image [31].

- The peak signal to noise ration (PSNR) measures the spatial reconstruction quality [35, 36] and it is given by

$$PSNR_i = 10\ log_{10}(\frac{MAX_i^2}{MSE_i}), \tag{1.14}$$

where MAX_i is the maximum pixel value in the ith band image and

$$MSE_i = \frac{1}{N}\sum_{r=1}^{N}(M_r - F_r)^2{}_{i,r}, \tag{1.15}$$

where index (i, r) indicates the rth pixel in the ith band. A larger PSNR value indicates a higher spatial reconstruction quality.

1.3.1.2 Full Scale Assessment

The quality with-no reference (QNR) protocol calculates the quality of the pansharpened images without requiring a high-resolution reference MS image [37]. The QNR comprises two indexes, one pertaining to spectral distortion and other to spatial distortion. The two distortions may be combined together to yield a unique quality index [37].

- The spectral distortion D_λ is calculated between the low-resolution MS images and the fused MS images [37] using

$$D_\lambda = \sqrt[p]{\frac{1}{N(N-1)} \sum_{l=1}^{N} \sum_{r=1}^{N} |Q(M_r, M_L) - Q(F_r, F_L)|^p}. \tag{1.16}$$

- The spatial distortion D_S is determined by calculating Q-index between each MS band and the PAN image degraded to the resolution of MS (P_L) and again between fused MS and full resolution PAN (P) [37] and computed as

$$D_S = \sqrt[q]{\frac{1}{N} \sum_{r=1}^{N} |Q(M_r, P_L) - Q(F_r, P)|^q}. \tag{1.17}$$

The exponent p and q in (1.16) and (1.17) are generally chosen as one [37].

- The QNR index is defined as [32]

$$QNR = (1 - D_\lambda)^u (1 - D_S)^v, \tag{1.18}$$

where u and v are the weighted coefficients which are usually taken as unity [37]. The higher the QNR index, the better the quality of the fused product. The maximum theoretical value of this index is 1, when both D_λ and D_S are equal to zero [37].

1.4 Challenges of the Image Fusion Schemes

After an in-depth and critical literature survey, the present study found that to design an image fusion scheme one needs to take care of the following Challenges:

- The fusion process should maximize the amount of relevant information in the fused image while minimizing the amount of irrelevant details, uncertainty, and redundancy in the fused image.
- Incorporate essential information from different modality sensors into a composite image to obtain both high spatial and spectral resolution in a single image.
- Provide an effective way of reducing the increasing volume of information while at the same time extracting all the useful information from the source images.
- The generated fused image is more suitable for human/machine perception, and for further image-processing tasks such as segmentation, object detection or target recognition.

1.5 Motivation

For many applications the information provided by individual sensors is incomplete, inconsistent, or imprecise and additional sources may provide complementary data. Fusion of different information results in better understanding of the observed site thus decreasing the uncertainty related to the single sources. Over a period of a decade, remote sensing, medical imaging, surveillance systems, etc. are a few applications areas that were benefited by these multi-sensors. As the number of sensors increases in an application, the proportionate amount of image data collected. A sensor grabs multiple images of a location, and one of them can be considered for analysis. However, the considered image may not have good spatial and spectral resolution. To overcome this and to generate a fused image with high spatial and spectral

resolution, this thesis identifies the need for image fusion/pansharpening by developing new methods to improve the performance of existing fusion methods which are given below:

- Recently, Hilbert vibration decomposition (HVD) has been proposed by M. Feldman et al. [38], for analyzing non-linear and non-stationary signals. It decomposes a wideband input signal into many signals in a decreasing order of the energy in terms of instantaneous amplitude and frequency components. The HVD estimates the frequency of a signal by averaging the instantaneous frequency of the signal components [38]. The HVD has higher frequency resolution than the empirical mode decomposition (EMD) based approaches for a given signal [38]. Since most of the sensors or image acquisition devices are sensitive to energy as well as frequency of the signals, it would be interesting to investigate the use of HVD for image fusion/pansharpening of images.

- The fractional Fourier transform (FRFT), which is a generalized version of the conventional Fourier transform. It provides representation in these intermediate domains, and the 2D discrete FRFT (2D-DFRFT) of a signal provides infinite representations of the given signal in different DFRFT domains for corresponding angles, and the DFRFT provides a free degree of freedom in terms of its angle parameters. The 2D-DFRFT has been applied in many image processing applications [39, 40, 41, 42, 43, 44, 45, 46, 47] but the use of discrete fractional Fourier transform (DFRFT) in image fusion/pansharpening has not been investigated so far.

- The graph signal processing (GSP) and the spectral graph wavelet filterbank (SGWF) have been shown to be promising in many areas [48, 49] utilizing the ability to decompose images into different subbands via the spectral characteristics of the images in the graph domain. The GSP exploits internode/interpixel dependence and it can be the reason for the improved results with the GSP. The time-frequency localization property and filterbanks of conventional wavelet transform have also been extended to GSP as SGWF

and associated filterbanks but its use in image fusion/pansharpening has not been investigated so far.

1.6 Problem Statement

Fused/pansharpened images obtained by the existing fusion/pansharpening schemes may suffer from the spatial and spectral distortion problems. Existing fusion schemes improve the spatial quality and reduce the spectral distortion in the fused image obtained by performing filtering in time domain or joint time-frequency domains [50, 51]. For attaining these objectives, some new image fusion/pansharpening algorithms are developed using three techniques in this thesis, that are as follows:

- Investigating the image fusion/pansharpening schemes based on the use of Hilbert vibration decomposition (HVD).
- Investigating the image fusion/pansharpening schemes based on the use of two dimensional discrete fractional Fourier transform (2D-DFRFT).
- Investigating the image fusion/pansharpening schemes based on the use of graph signal processing (GSP)/spectral graph wavelet filterbank (SGWF).

1.7 Thesis Contribution

The original contribution made in this thesis is to develop new pansharpening methods for remote sensing applications based on HVD, 2D-DFRFT and GSP techniques for improving the spatial quality and reduce the spectral distortion in the pansharpened image to make it more suitable for human/machine perception, and for further image-processing tasks such as segmentation, object detection or target recognition. For medical diagnosis, concealed weapon

detection (CWD), military surveillance, etc. applications also develop image fusion schemes based on HVD, 2D-DFRFT, and GSP which have maximum information of the source images taken by the different sensors or cameras while minimizing the amount of irrelevant details, uncertainty, and redundancy in the fused image.

1.8 Organization of Thesis

Chapter 2 introduces the background of the image fusion/pansharpening schemes for different types of applications like medical images, remote sensing images etc.

Chapter 3 proposes three approaches for image fusion/pansharpening. The proposed techniques are based on the recently developed signal decomposition technique known as Hilbert vibration decomposition (HVD). In the proposed pansharpening methods, PAN and MS images are decomposed into many instantaneous amplitude and frequency components in the decreasing order of energy using the HVD. The instantaneous amplitude of the first component (having highest energy) in a decomposition of the PAN and MS images are used to generate the pansharpened image using pansharpening model. Experimental results of the proposed technique are presented for AVIRIS, Pleiades, IKONOS and GeoEye-1 satellite images and compared with existing pansharpening methods in terms of both visual perception and objective metrics such as Q-index, spectral angle mapper, relative dimensionless global error, peak signal-to-noise ratio and quality with no-reference (QNR).

It is observed that the proposed pansharpening schemes have improved spectral and spatial quality as compared to the existing schemes. The effects of aliasing and misregistration errors in the proposed methods are also investigated and it is observed that the proposed methods are robust against aliasing and misregistration errors as compared to other existing methods. In the image fusion technique, the HVD decomposes the source images into instantaneous amplitude and frequency components with decreasing energy values. Amplitude components

of the first and second signals in the decomposition of the source images are used to generate the fused images using appropriate fusion rule. Performance evaluation of fused images is done by computing fusion quality metrics and the fusion results are compared with other existing fusion schemes. It is seen that the performance of the proposed scheme is better as compared to the existing fusion schemes.

In **Chapter 4**, three approaches for image fusion/pansharpening based on 2D-discrete fractional Fourier transform (2D-DFRFT) are proposed. In the proposed pansharpening methods, PAN and MS images are transformed using the 2D-DFRFT and further used to generate the pansharpened image using appropriate pansharpening rule. The angle parameters associated with the 2D-DFRFT provide additional degrees of freedom which are optimized for finding better pansharpening results. Simulation results of the proposed technique carried out in MATLAB are presented for IKONOS and GeoEye-1 satellite images and compared with existing fusion methods in terms of both visual perception and objective metrics such as Q-index (Q), spectral angle mapper (SAM), relative dimensionless global error (ERGAS) and quality with-no reference (QNR).

It is observed that the proposed pansharpening scheme provides improved spectral and spatial quality as compared to the existing schemes. The effects of aliasing and mis-registration errors on the proposed methods are also investigated and compared to existing pansharpening methods. It is seen that the proposed methods are robust against aliasing and mis-registration errors. In the proposed image fusion scheme, input source images are transformed using 2D-DFRFT and then subtracted from the respective source images to obtain the detail images. The detail images are further used to generate the fused image using appropriate fusion rule. An additional degree of freedom in terms of its angle parameters associated with the 2D-DFRFT is exploited for obtaining better results in the proposed fusion scheme. Performance evaluation of fused images is done by computing fusion quality metrics and the fusion results are compared to other existing fusion schemes. It is seen that performance of the proposed scheme is better in terms of the fusion quality metrics as compared to the existing fusion schemes.

In **Chapter 5**, two novel image fusion/pansharpening approaches based on graph signal processing GSP/spectral graph wavelet filterbank (SGWF) are proposed. In the proposed pansharpening method, the PAN image is decomposed by the multistage M-channel SGWF, and then the weighted combination of lowpass component signals in the multistage SGWF decomposition are used to generate the pansharpened image using appropriate pansharpening rule. Simulation results of the proposed technique using different wavelets such as spline wavelet (SW), mexican-hat wavelet (MHW), meyer wavelet (MW) and simple tight frame wavelet (SPW) for GeoEye-1 satellite images are also presented and compared with existing pansharpening methods in terms of both visual perception and objective metrics such as Q-index (Q), spectral angle mapper (SAM), relative dimensionless global error (ERGAS) and quality with-no reference (QNR).

It is observed that the proposed pansharpening scheme provides better pansharpening results using MHW filterbank as compared with some of the existing schemes. In the proposed image fusion scheme, input source images are decomposed by the multistage M-channel SGWF and the weighted combination of lowpass component signals in the multistage SGWF decomposition are added to the respective source images to obtained the detail images. The detail images are further used to generate the fused image using appropriate fusion rule. Simulation results of the proposed technique are obtained using mexican-hat wavelet (MHW) filterbank and compared with existing fusion methods. Performance evaluation of fused images is done by computing fusion quality metrics and the fusion results are compared with other existing fusion schemes. It is seen that the performance of proposed scheme is better in terms of the fusion quality metrics as compared to the existing fusion schemes.

Chapter 6 concludes all the proposed image fusion/pansharpening schemes. Simulation results of the proposed technique based on SGWF provide better results as compared to the HVD and 2D-DFRFT based proposed techniques in terms of qualitative and quantitative analysis.

Chapter 2

Literature Review

This chapter represents past research efforts in the area related to image fusion. An extensive study of the existing literature which forms the guidelines for the development of new methodologies discussed in the image fusion has been performed. We begin with the definition of the process of fusion and discuss some of the nomenclatures in the field of image fusion. An overview of various techniques of image fusion is also presented. The purpose of this chapter is to study and document the different methodologies used for image fusion, although not necessarily for remote sensing applications alone. This chapter also explores the existing performance measures for an assessment of fusion techniques.

During the past century, we have witnessed a rapid growth in the advancement of technology. The invention of a vast number of sensors has resulted in high volumes of data collection. These datasets, obtained from multiple sensors provide complementary information about the scene or objects being imaged. The performance of many intelligent systems and devices has significantly improved with the availability of the multi-sensor input. However, instead of processing individual data from all the sensors, it would be desirable to extract and merge the useful information from the set of sensors and process this particular information to achieve

higher throughput [52]. The primary objective of fusing images is to obtain an image that is more useful and more significant to the particular application [53].

2.1 Classification of Image Fusion and Pansharpening Techniques with Explanation

The classification of techniques helps in understanding the concepts related to fusion in a better manner. We discuss some of the fusion categories here.

Based on Processing Level

An image assists in providing a decision, such as diagnosis of a disease, presence of security threatening objects, or existence of water bodies within some areas. Accordingly, images can be fused at pixel-level, feature-level, or decision-level. We can categorize fusion techniques concerning the level of processing at which the actual fusion takes place. This categorization is particularly important because it decides the level of image representation where the actual fusion takes place.

General data can be analyzed and fused at the signal level which is the most fundamental level of understanding and processing the data. The pixel level fusion regarded as the counterpart of signal level operations in the field of data fusion is the lowest level of image fusion. Images from multiple sensors capture their observations in the form of pixels which are then combined to produce a single output image. Thus, the pixel-level fusion algorithms operate directly on input images.

Feature level fusion requires feature extraction from input images with the use of advanced image processing operations such as region characterization, segmentation, and morphological

operations to locate the features of interest. The choice of features plays an important role here, which is primarily decided by the end application. The regions or features are represented using one or more sets of descriptors. Multiple sets of such descriptors provide complementary information, which is then combined to form a composite set of features. These techniques are less sensitive to pixel-level noise [54].

For a decision level fusion, the input images and/or feature vectors are subjected to a classification system which assigns each detected object to a particular class (known as the decision). The classifier systems associate objects to the particular class from a set of pre-defined classes. Decision fusion combines the available information for maximizing the probability of correct classification of the objects in the scene which is achieved using statistical tools such as Bayesian inference.

Based on Domain

This type of categorization is of two types: Spatial domain and Transform domain. A fusion algorithm can operate over the spatial data, fusion rules are directly applied into the images on the basis of pixel level and feature level. In the spatial domain methods, gradient basis [55], principal component analysis [56], singular value decomposition [57], empirical mode decomposition [58], etc. are used in the image fusion. Alternatively, using different transforms such as Fourier transform, one may transform the set of input images into frequency domain. The fusion algorithm processes the frequency domain data to produce the result of fusion in the frequency domain. This result requires a reverse transformation such as inverse Fourier transform to obtain the fused image. In the transform domain methods, discrete cosine transform [59], wavelet transform [60], curvelet transform [15], etc. are used for image fusion.

Based on Nature of Images

This categorization is somewhat different from the previous ones. Here one is more concerned about the type of the data rather than type or technique of fusion. The sources of images can be very different. Most of the real world scenes encompass a very high dynamic range (HDR). Most of the digital cameras are not able to capture these scenes due to their limited dynamic range. However, one can capture multiple images of the location with varying exposure settings of the camera. This set of low dynamic range (LDR) images when appropriately fused, generates a single image that provides an HDR-like appearance [61, 62]. Such type of fusion is often regarded as multi-exposure image fusion. Similarly, the finite size of the aperture of the camera leads to defocused objects in the image. Due to the physics behind the camera lens, only the regions at a certain distance from the focal plane of the camera can be captured in focus for a given setting of the camera focus. To obtain a single image where all objects are in focus, we may capture multiple images by suitably varying the focus of the camera, and fuse them later. This multi-focus image fusion operates on different principles than those of multi-exposure images due to the difference in the formation of these images.

In remote sensing, one often comes across multispectral image fusion where typically 4-10 bands of a multispectral image are combined to yield a compact description of the scene. Advanced hyperspectral imaging sensors capture the scene information in hundreds of bands depicting the spectral response of the constituent materials of the scene. Hyperspectral image fusion refers to the combining of these bands into a single image that retains most of the features from input hyperspectral bands. The medical community makes use of images obtained from different sensors (e.g., Positron emission, X-rays) providing complementary information about the scene. The fused image which has proved to be quite useful in medical diagnosis combines and enhances features from the input images. This class of fusion is referred to as multi-modal image fusion. The medical community has greatly benefited from the feature enhancement characteristics of image fusion. Medical diagnosis can be improved by the use of

complementary information provided by the multimodal images such as computed tomography (CT), magnetic resonance imaging (MRI), and Positron emission tomography (PET). Fusion helps in enhancing features which are impossible to detect from a single image, and thus improves the reliability of the decisions based on the composite data [45].

Based on Resolution

Remote sensing images are characterized by four types of resolution: spatial resolution, spectral resolution, radiometric resolution, and temporal resolution.

- Spatial resolution: In digital image sensors, the analog images produced by the optical system are spatially sampled by the detector. Spatial resolution is a measure of the optical sensor's ability to record closely spaced objects such that they are distinguished as separate objects. If the imaging scenes are oversampled with a spatial frequency higher than the Nyquist frequency, it results in a high resolution image.

- Spectral resolution: Spectral resolution refers to the frequency or spectral resolving power of a sensor and is defined as the smallest resolvable wavelength difference by the sensor. Spectral resolution represents the width of the band within the electromagnetic spectrum that can be sensed by a sensor. As the bandwidth becomes narrower, the spectral resolution becomes higher. The spectral resolution plays an important role in satellite imaging. High spectral resolution images captured by remote sensing camera provide more detailed information about mineral resources and geographical structures of the earth or any other planet under observation.

- Radiometric resolution: Pixels carry information of the image intensity in form of binary digits called 'bits'. The intensity at any location in a real world scene may vary from zero to infinity. However in digital image it is not possible to represent this entire range. A binary image has two levels-black and white, hence requires only one bit for each pixel.

A gray scale image is usually quantized using 256 grey levels with each level represented using 8 bits. Similarly, if each color plane of an RGB image requires 8 bits then at least 24 bits are needed for representing each pixel.

- Temporal resolution: The term temporal resolution is related to video signals. A video of an event is a sequence of images (frames) captured at regular and short time interval between them. Temporal resolution, also known as frame rate, is the measure of the capability of displaying smallest movement/ motion of the moving objects in the video. Thus it refers to the number of frames captured per second. A video captured with low temporal resolution exhibits flicker or transitions of the moving objects in the scene/event. With high temporal resolution, the movement of the moving objects appears smooth and continuous. For a given duration of time, a high temporal resolution video requires more memory for storage and large bandwidth for transmission. In remote sensing, temporal resolution refers to the frequency at which a given geographical area is imaged. Higher temporal resolution enables monitoring the occurrence of rapid changes such as forests, floods, etc. This also improves the probability of obtaining cloud-free imagery over areas that experience frequent cloud cover.

Based on Methodology

In the remote sensing based on methodology, image fusion/pansharpening schemes are most commonly classified into four categories:

- **Component substitution (CS) method:** The CS approach relies on the substitution of a component (obtained by a spectral transformation of the input image) of the MS images by the PAN image. The CS based pansharpening methods based on intensity-hue-saturation (IHS) transformation, Gram-Schmidt (GS) orthogonalization and principal component analysis (PCA), Brovey transform (BT), etc. are discussed in [5, 63, 64, 65].

These approaches usually provide high spatial details in the fused image [66] and they are, in general, fast and easy to implement. However, these are not able to account for local dissimilarities between the PAN and MS images originated by the spectral mismatch between the PAN and MS channels of the instruments [32, 67].

- **Multiresolution analysis (MRA) method:** The MRA approach is based on the injection of the spatial details which are obtained through filtering of the PAN image into the MS images. These algorithm limits the spectral distortion of the fused image which can be quantified by the spectral angle between fused and interpolated MS, and belong to the spectral distortion minimization family [32, 68]. The MRA based pansharpening schemes using wavelet packet, nonsubsampled shearlet transform have also been presented in [69, 70].

- **Hybrid analysis method:** The hybrid pansharpening methods make use of the advantages of both CS and MRA techniques by combining them as discussed in [71], [72], etc.

- **Model based methods:** The model based pansharpening methods based on online coupled dictionary learning (OCDL), spatial correlation modeling, MRF model, compressive sensing-based (CS) technique, etc. are discussed in [73, 74, 75, 76].

The most direct or easy technique of fusion is to sum and average the input images. The averaging method explicitly assumes an equal amount of information to be present in the input images. It is computationally most efficient. However, it fails to produce an output of the desired quality [77]. The infrared (IR) image brings out very different information from the scene that does not get captured by a standard RGB camera. However, an average-based fusion would superimpose the features in IR image by the RGB image, and thus, reduce the contrast and information content. Therefore, an averaging-based fusion works well only when both the inputs are similar, and lacks contrast when the inputs are different. This information from multiple images causes a destructive interference which reduces the contrast. Therefore, despite

its simplicity and computational efficiency, this method is rarely used in practice. Fusion would be effective when the important spatial and radiometric features from the constituent images get retained, or are appropriately enhanced during the process of fusion. Thus, one needs to extract the spatial features from images as the first step.

To capture the unique features in an input image, Toet proposed the use of a Laplacian pyramid [78, 79]. The authors have proposed a hierarchical technique which decomposes each of the input images into a set of primitives defined by perceptually relevant patterns. This technique generates a pyramidal decomposition of each of the input images through filtering and subsampling. The successive images in the pyramid are the reduced versions of the input image, and hence this representation is also referred to as the multi-resolution representation. The successive levels of the image pyramid represent image details and features with coarser approximations. The pyramidal representations of all the input images are then appropriately combined at every level using a pre-defined fusion rule. The fusion rule might be the same or different at every level, however, typically, one comes across two sets of rules. A fusion rule defined for all but the highest level of the pyramid is the same, and a different fusion rule is established for the final or the first level image in the corresponding image pyramid. However, it is possible to have a combination of more fusion rules. The combining process generates an image pyramid where each level represents the fusion of images at that particular level. The final resultant image can then be reconstructed by applying the reverse transformation on the fused image pyramid.

Another popular pyramidal structure is obtained by convolving the current approximation of the image with the Gaussian filter. The pyramid so obtained is called a Gaussian pyramid. In [66], the filtering and sampling have been combined into a single operation resulting in the Gaussian weighted average. However, in [78], it has been argued that the linear filters alter the intensities of the pixels near the object boundary, and therefore, their applicability is limited when the precise measurements of the shape and size of the objects are needed. Their scheme employs a morphological multi-resolution decomposition of images using size-selective filters.

It is claimed that morphological filters are more suitable for shape extraction of the objects in the fused image due to their property of removing the image details without adding any gray level bias. In [77], proposed a generalized multisensor fusion using the gradient pyramid where an image pyramid has been created by the pyramid transform. Using the basis functions of gradient-of-Gaussian pattern, the pyramid transform is applied to the input images. Two fusion rules are used to combine the information of the multiple decompositions at the locations where the source images are similar; the fusion is achieved by averaging two images, while if the images are significantly different, the fusion rule selects the feature pattern with maximum saliency and copies it for the fused image.

In [80], the use of a steerable pyramid for fusion of remote sensing images has been demonstrated. The steerable pyramid is a multi-scale and multi-orientation decomposition with translation and rotation invariant sub-bands [81]. The low frequency or the coarsest approximation is fused based on the magnitude of the images at the corresponding locations. A region-based technique in a multi-resolution framework as an extension of the pixel-based technique [54]. This work provides multi-resolution fusion techniques. The input images are first segmented which is a preparatory step toward the actual fusion. The other quantity is the match measure which quantifies the similarity between the corresponding coefficients of the transformed images. This structure encompasses most of the pixel-based and region-based multi-resolution techniques. For an efficient fusion, the salient features from multi-scale image decomposition are extracted. The wavelet transform has proved to be a highly popular tool for fusion. A discrete wavelet transform (DWT) based fusion technique offers distinct advantages such as orthogonality, compactness, and directional information [21]. This technique is superior to the Laplacian pyramid-based techniques. It does not produce any visible artifacts in the fused image. Similar to the multi-resolution fusion approaches, the wavelet-based fusion techniques first decompose the set of input images into different multi-resolution coefficients that preserve image information. These coefficients are appropriately combined at each level to obtain new coefficients of the resultant image. This image is then recovered via an inverse discrete wavelet

transform (IDWT) to generate the final fused image. In [78, 79], the fusion rule has been defined to select the maximum of the corresponding coefficients of the ratio pyramid of input images, while the fusion rule that selects the maximum across discrete wavelet coefficients of the input images has been proposed in [21].

Wavelets have probably been the most successful family of fusion techniques. Wavelet-based fusion techniques have been implemented for various other application areas. In [82], several applications of DWT-based fusion for forensic science have been demonstrated. Another application of wavelet decomposition for fusion of multi-focus images using the log-Gabor wavelets has been described by Redondo et al. [83]. The wavelet-based fusion techniques have also proved to be useful for fusion of medical images. Performance of various multi-resolution techniques for fusion of retinal images has been analyzed in [25, 26]. In [27], wavelets have been shown to be useful for fusion of CT and MRI images. The $\grave{a}$ trous wavelet transform (ATWT) is a non-orthogonal undecimated multiresolution decomposition. It is used by several pansharpening techniques [84] to avoid injection of undesired spatial details in the pansharpened image by context driven thresholding of correlation coefficients between the images to be fused in the wavelet domain [84]. The undecimated wavelet decompositions (UDWT) and Laplacian pyramids have proven to be effective is implementing fusion at different resolutions [71, 84]. Wavelet decomposition is a widespread method used for image fusion [21]. Wavelet decomposition uses basis functions or different filters that are fixed and create influence in the fused image. In [21], the wavelet transforms experience problems when analyzing high frequency content, thus tending to lose spatial information.

Another technique, empirical mode decomposition (EMD) proposed by Huang et al. [85], adaptively decomposes a signal into the simplest intrinsic oscillatory components. In [86], the EMD based image fusion method has been shown to give excellent performance as compared to the wavelet and PCA based approaches, particularly in retaining edge-based information from the different image modalities. The empirical mode decomposition (EMD) is however incapable of separating frequencies components which are closely spaced or weak at high frequencies.

Recently a fast Fourier transform (FFT) based pansharpening scheme was proposed in [87]. This method is based on IHS transform with FFT filtering of both the PAN image and intensity image component of the original MS images. It may be mentioned here that due to finite spatial size of MS and PAN images, these images will not be band limited in FFT domain and therefore FFT based pansharpening may not be suitable in such cases. The compressive sensing-based fusion technique can greatly reduce the processing time and guarantee the quality of the fused image using fewer non-zero coefficients. However, directly fusing sensing measurements may bring greater uncertain results with high reconstruction error. Moreover, using single fusion rule may result in the problems of blocking artifacts and poor fidelity.

In [76], a novel image fusion approach based on compressive sensing is introduced to solve these problems. In this fusion framework, in the first step, the multi-scale transform is performed on each of the preregistered source images to obtain their low-pass and high-pass coefficients. In the second step, the low-pass bands are merged with a sparse representation based fusion method while the high-pass bands are fused using the absolute values of coefficients as activity level measurement. Finally, the fused image is obtained by performing the inverse multi-scale transform on the merged coefficients. This method is superior to the individual multi-scale transform or sparse representation based methods.

In [88], a remote sensing image fusion method based on the ripplet transform and the compressed sensing theory to minimize the spectral distortion in the pansharpened MS bands with respect to the original ones is proposed. Authors extracted the spatial details from the PAN image by means of ripplets and then injected them into MS bands by the proposed injection model named compressed sensing based injection. Authors in [89] designed an optimal filter that is able to extract relevant and non-redundant information from the PAN image. Compared with other kernels such as wavelets, the optimal filter coefficients extracted from statistical properties of images are more consistent with type and texture of remotely sensed images.

An online coupled dictionary learning (OCDL) approach for image fusion has been introduced in [73]. The OCDL makes full use of the available lower spatial resolution MS image and the

high spatial resolution PAN image to decrease the spectral distortion and preserve the spatial information of the MS image. A superposition strategy is adopted in the OCDL method to produce two intermediate images for the coupled dictionary construction for each band. An iterative update method is utilized to update the coupled dictionaries, which can be referred to as an online dictionary learning process.

In remote sensing images, demands for spectral and spatial resolution vary from region to region. Regions with abundant texture and well-defined boundaries (like residential areas and roads) need more spatial details to provide better descriptions of various ground objects while regions such as farmland and mountains are mainly discriminated by spectral characteristic. However, most existing fusion algorithms for remote sensing images execute a unified processing in the whole image, leaving those important needs out of consideration. The employment of diverse fusion strategy for regions with different needs can provide an effective solution to this problem. In [90], proposes a new saliency-driven fusion method based on complex wavelet transform. Firstly, an adaptive saliency detection method based on clustering and spectral dissimilarity to generate saliency factor for indicating diverse needs of the two kinds of resolutions in regions. Secondly, they combine nonlinear intensity–hue–saturation transform with multiresolution analysis based on dual-tree complex wavelet transform in order to complement each other's advantages. Finally, saliency factor is employed to control the detail injection in the fusion, helping to satisfy different needs of different regions.

In [91], the fuzzy c-means algorithm based pansharpening scheme is proposed to reduce color distortion. This scheme consider mixed pixels not belonging to any distinct class. Here multispectral images are clustered into several classes using spectral and spatial features, and then linear regression with non-negative coefficients is used to calculate summation weights for each class of pixels.

In [92] proposes a fusion scheme to combine Landsat and MODIS remote sensing data at the decision level. Multiresolution segmentations on the two kinds of remote sensing data are performed to identify the landscape objects and are used as fusion units in subsequent steps.

Then, fuzzy classifications are applied to each of the two different resolution data sets and the classification accuracies are evaluated. According to the performance of two data sets in classification evaluation, a simple weight assignment technique based on the weighted sum of the membership of imaged objects is implemented in the final classification decision. The weighting factors are calculated based on a confusion matrix and the heterogeneity of detected land cover. The algorithm is capable of integrating the time-series spectral information of MODIS data with spatial contexts extracted from Landsat data, thus improving the land-cover classification accuracy.

Deep convolutional neural networks (DCNNs) have recently emerged as the highest performing approach for a number of image classification applications, including automated land cover classification of high-resolution remote-sensing imagery. In [93] investigate a variety of fusion techniques to blend multiple DCNN land cover classifiers into a single aggregate classifier. While feature-level fusion is widely used with deep neural networks. Here train three different DCNNs: CaffeNet, GoogLeNet, and ResNet50 dataset is used. The effectiveness of various information fusion methods, including voting, weighted averages, and fuzzy integrals, is evaluated.

To address the problem of change detection for remote sensing images from the perspective of visual saliency computation. In [94] method incorporates low-rank-based saliency computation and deep feature representation. Firstly, multilevel convolutional neural network (CNN) features are extracted for superpixels generated using saliency map indicating change (SLIC), in which a fixed-size CNN feature can be formed to represent each superpixel. Secondly, low-rank decomposition is applied to the change features of the two input images to generate saliency maps that indicate change probabilities of each pixel. Finally, binarized change map can be obtained with a simple threshold. To deal with scale variations, a multiscale fusion strategy is employed to produce more reliable detection results.

In [95] based on the deep convolutional neural network, a remote sensing image fusion method that can adequately extract spectral and spatial features from source images is proposed. The

major innovation of this study is that the fusion method contains a two branches network with the deeper structure which can capture salient features of the MS and PAN images separately. This method mainly consists of two procedures. First, spatial and spectral features are respectively extracted from the MS and PAN images by convolutional layers with different depth. Second, the feature fusion procedure utilizes the extracted features from the former step to yield fused images.

In the proposed method [96], the spatial details are first extracted from the multispectral (MS) and panchromatic (PAN) images through à trous wavelet transform and multiscale guided filter. Different from the traditional detail injection scheme, the extracted details are then sparsely represented to produce the primary joint details by dictionary learning from the sub-images themselves. To obtain the refined joint details information, subsequently design an adaptive weight factor considering the correlation and difference between the previous joint details and PAN image details. Therefore, the refined joint details are injected into the MS image using modulation coefficient to achieve the fused image.

Recently, approaches based on fully convolutional networks (FCN) [97] have achieved state-of-the-art performance in the semantic segmentation of very high resolution (VHR) remotely sensed images. One central issue in this method is the loss of detailed information due to downsampling operations in FCN. To solve this problem, introduce the maximum fusion strategy that effectively combines semantic information from deep layers and detailed information from shallow layers. Furthermore, this letter develops a powerful backend to enhance the result of FCN by leveraging the digital surface model, which provides height information for VHR images.

In the field of pan-sharpening, only limited studies have been undertaken in recent years to introduce deep learning models. Examples are the sparse deep neural network [98] and the pan-sharpening neural network (PNN) [99] that have achieved impressive performance gains. Along with being developing of mathematical tools and fusion rules, image fusion methods are continually being renewed.

2.2 Summary of the Survey

Fusion scheme	Advantage	Disadvantage
Averaging techniques [77, 171, 172]	Computationally most efficient, easy to implement, easy to understand	It reduces the resultant image quality consequently by introducing noise into fused image. It leads to unwanted side effects like reduced contrast.
Maximum Pixel Value Technique [171, 172], Max- Min Technique [170], Simple Block Replace Algorithm [170]	Easy to implement	These methods produce blurred output which in turn affects the contrast of the image. Therefore these techniques are not suitable for real time applications.
Weighted averaging technique [169]	Improves the detection reliability	It can increase the signal to noise ratio (SNR) of the fused image
Principal component analysis algorithm [56, 167, 168]	Very simple, computationally efficient, faster processing time and high spatial quality	Results in spectral distortion

Fusion scheme	Advantage	Disadvantage
IHS based scheme [172]	Very simple, computationally efficient, faster processing and high sharpening ability	It only processes three multispectral bands and results in spectral distortion
Brovey transform [171]	Very simple, computationally efficient and faster processing time. It produces RGB images with higher degree of contrast	Spectral distortion in the fused image
Guided filtering [162]	Very simple, computationally efficient, suitable for real applications	Spectral distortion in the fused image
Discrete cosine transform (DCT) method [166]	It reduces the complexity and decomposed images into series of waveform. This algorithm can be used for real applications	Fused image is not of good quality if block size is less than 8x8 or equivalent to the image size itself
Discrete Wavelet Transform (DWT) with Haar based fusion [163, 164, 165]	It provides a good quality fused image and better Signal to Noise Ratio. It also minimizes spectral distortion	The fused image has less spatial resolution.

Fusion scheme	Advantage	Disadvantage
Stationary Wavelet Transform (SWT) [159, 161]	This method provides good result at level two of decomposition	It is time-consuming
Fusion using Laplacian/ Gausian Pyramid [78, 79, 157, 158]	Pyramid methods provide good visual quality of the image for multi-focus images.	The number of decomposition levels affects image fusion result.
Discrete wavelet decomposition based image fusion [21]	Provides high spatial and spectral quality at low frequency	Basis functions or different filters that are fixed and create influence in the fused image, experience problems when analyzing high frequency content, lose spatial information
Empirical mode decomposition (EMD) based fusion scheme [86]	Gives excellent performance particularly in retaining edge-based information from the different image modalities	Loses spatial information at high frequencies
Fast Fourier transform (FFT) based scheme [87]	Reduces noise in the fused images	Multispectral images will not be band limited in FFT domain and therefore FFT based fusion scheme provides spectral distortion

Fusion scheme	Advantage	Disadvantage
Compressive sensing based fusion technique [76, 88]	Minimize spectral distortion in the fused image, greatly reduce the processing time	Problems of blocking artifacts and poor fidelity
Optimal filter based fusion [89]	High spatial resolution	Spectral distortion in fused image
An online coupled dictionary learning (OCDL) approach for image fusion [73]	Decrease spectral distortion and preserve the spatial information of the MS image	High execution time, require large dataset
Fuzzy c-means algorithm based pansharpening scheme [91]	Reduce color distortion in the image	Requires more computation time
The weight assignment using fuzzy algorithm technique based scheme [92]	Improve the classification accuracy	Requires more computation time
The deep convolutional neural networks (DCNNs) based scheme [93, 95]	High spatial and spectral detail in fused image	Large training dataset required, takes more computation time

Fusion scheme	Advantage	Disadvantage
Multilevel convolutional neural network (CNN) based method [94]	Incorporates low computation, reliable results	
The dictionary learning based scheme [96]	High spatial detail image	Spectral distortion in the fused image
Fully convolutional networks (FCN) [97] based scheme	Very high resolution (VHR) image	Loss of detailed information
Neural network based fusion scheme [98, 99]	High spatial and spectral resolution fused image	Requires iterative computing, which is time-consuming and may cause incidental errors, especially for the images with a large size

Chapter 3

Hilbert Vibration Decomposition Based Image Fusion/Pansharpening Schemes

In this chapter, a recently developed signal decomposition technique known as the Hilbert vibration decomposition (HVD) based image fusion/pansharpening schemes is presented. The objective of these research work is to develop efficient image fusion/pansharpening techniques which have high spatial and spectral quality of the fused image. For attaining these goals, initially, the HVD technique is used for developing three image fusion/pansharpening algorithms in which two pansharpening and one image fusion techniques are presented. The structure of this chapter is as follows: in section 3.1, introduction and a brief literature review is presented; in Section 3.2, details of the HVD method is explained; Section 3.3 provides details of the proposed pansharpening scheme-I and simulation results which provides a comparative analysis of the proposed scheme with existing schemes; Section 3.4 describes aspects of the proposed pansharpening scheme-II with simulation results; Section 3.5 describes the proposed image fusion method with simulation results which gives a comparative analysis of the proposed scheme with existing schemes. Conclusions are drawn in Section 3.6.

3.1 Introduction

Remote sensing satellites capture many types of images using different types of cameras/sensors such as panchromatic (PAN), hyperspectral (HS) and multispectral (MS) images [100]. It is a well known fact that PAN images have high spatial and low spectral resolution while MS (few bands) and HS (more than one hundreds bands) images have low spatial and high spectral resolution [31]. In addition, the HS images provide more accurate spectral information than MS images which is necessary for applications such as change detection [101, 102], object recognition [103, 104], visual image analysis [105] and scene interpretation [106], etc. High spatial resolution images give information of the shape and structure of the objects and high spectral resolution provides information about the details of land coverage. Images having both high spatial and spectral resolution are generally not provided by the satellite imaging systems. Due to this limitation, many of the pansharpening techniques have been investigated and presented in the literature [5, 6, 107]. With the increased availability of hyperspectral systems, these methods are now extended to the fusion of hyperspectral and panchromatic images [32, 100].

A fast Fourier transform (FFT) based pansharpening scheme is proposed in [87]. This method is based on IHS transform with FFT filtering of both the PAN image and intensity image component of the original MS images. However, the Fourier transform is suitable for stationary signal only [108]. The bi-dimensional empirical mode decomposition (BEMD) based image fusion method is presented in [109] and it has better performance as compared to the wavelet and PCA based approaches, particularly in retaining edge-based information from the different image modalities. The empirical mode decomposition (EMD) is however incapable of separating frequencies components which are closely spaced or weak at high frequencies.

3.2 Overview of HVD

The Fourier Transform (FT) converts a time domain signal into its frequency domain representation. However, this method is applicable for stationary signals [108]. To overcome this drawback, short time Fourier transform (STFT) is proposed which maps a signal into a two-dimensional function of time and frequency [110]. The STFT extracts time and frequency information of a signal, but the disadvantage is that the size of the window and hence, the time and frequency resolution is fixed for all frequencies [111]. The wavelet analysis represents a windowing technique with variable time frequency resolution of the signals but it varies with the wavelet function chosen [111]. The EMD, which has been recently introduced, is an adaptive method, which provides a powerful tool to extract intrinsic mode functions (IMF) from a wideband signal [85]. The EMD decomposes a wideband signal into IMFs in the decreasing order of frequency, i.e., from high frequency to low frequency, but it does not take into account the energy of IMFs into account [112]. These characteristics bring on the incapability of separating components which include closely spaced frequencies or weak high frequencies.

The HVD decomposes a non-stationary wideband signal into many signal components with slow varying instantaneous amplitudes and frequencies in the decreasing order of energy [38]. The HVD has much higher frequency resolution than the EMD based approaches for signal decomposition [113].

The HVD decomposition is based on the facts that, (a) the underlying signal is formed by a superposition of symmetric quasi-harmonic functions; (b) the envelopes of each oscillating component differ from each other; (c) the total length of each component spans several periods of the corresponding slowest components [38]. The HVD can be described as an iterative method as shown in Fig.3.1. The first step in the HVD is estimation of instantaneous frequency (IF) $\omega(t)$ of the signal.

This is done using the analytical signal representation of a given real signal [114]. The analytical signal Z(t) of a real signal H(t) is a complex signal as given by [114]

$$Z(t) = H(t) + H_H(t) = A(t)e^{i\phi(t)}, \tag{3.1}$$

where the real part corresponds to the original signal $H(t)$ and the imaginary part $H_H(t)$ is the Hilbert Transform of $H(t)$. From (3.1), the instantaneous amplitude $A(t)$ and instantaneous phase $\phi(t)$ are obtained as

$$A(t) = \sqrt{H(t)^2 + H_H(t)^2}, \tag{3.2}$$

$$\phi(t) = tan^{-1}\left(\frac{H_H(t)}{H(t)}\right). \tag{3.3}$$

The instantaneous frequency $\omega(t)$ is the derivative of $\phi(t)$ in (3.3) expressed as

$$\omega(t) = \frac{d}{dt}\phi(t) = \frac{H(t)\dot{H}_H(t) - \dot{H}(t)H_H(t)}{H^2(t) - H_H^2(t)}. \tag{3.4}$$

The signal $\omega(t)$ is lowpass filtered to obtain the signal $\omega_1(t)$. Using $\omega_1(t)$, the instantaneous

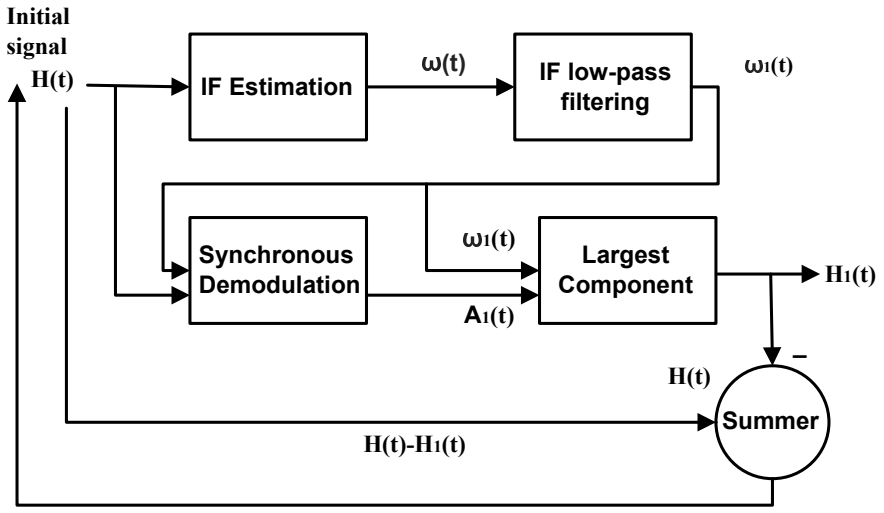

FIGURE 3.1: Block diagram of the HVD method

amplitude (IA) of the highest component in the decomposition, i.e., $A_1(t)$ is determined using synchronous demodulation procedure [114]. Finally the highest energy component is generated with $A_1(t)$ and $\omega_1(t)$, and a new signal is obtained by subtracting the highest component from the original signal and the process is repeated iteratively. After jth iteration, the decomposition of the signal $h\,(t)$ using HVD can be expressed as

$$h\,(t) = \sum_{j} A_j\,(t) \cos\left(\int \omega_j\,(t)\,dt\right), \tag{3.5}$$

where $A_j\,(t)$ is instantaneous amplitude (IA) and $\omega_j(t)$ is the instantaneous frequency (IF) of j components.

3.3 Proposed Pansharpening Scheme-I

The basic purpose of the image fusion or pansharpening methods are to improve the spatial quality and reduce the spectral distortion in the fused image. Some of the pansharpening schemes achieve this objective by performing filtering in time domain or joint time-frequency domains [50, 51]. In this chapter, HVD based pansharpening approach is proposed to improve the spatial and spectral quality of the fused image which is closer to the filtering/MRA based approach used in many of the existing pansharpening schemes given in [87], [115], [50]. The operation of obtaining instantaneous amplitude components of the signal through HVD can be considered as a filtering operation on the input signal.

In fact, the instantaneous amplitude of the first signal in the decomposition obtained through HVD is similar in shape to the lowpass filtered version of a signal. To explain the point further, the rectangular pulse and first instantaneous amplitude component of its HVD are shown in Fig.3.2 (a) and 3.2(b) respectively. The output of the Butterworth lowpass filter with rectangular pulse as input is shown in Fig.3.2(c). It is clear from these figures that the shape of the signals in Fig.3.2(b) and 3.2(c) are very close to each other. This lowpass signal obtained

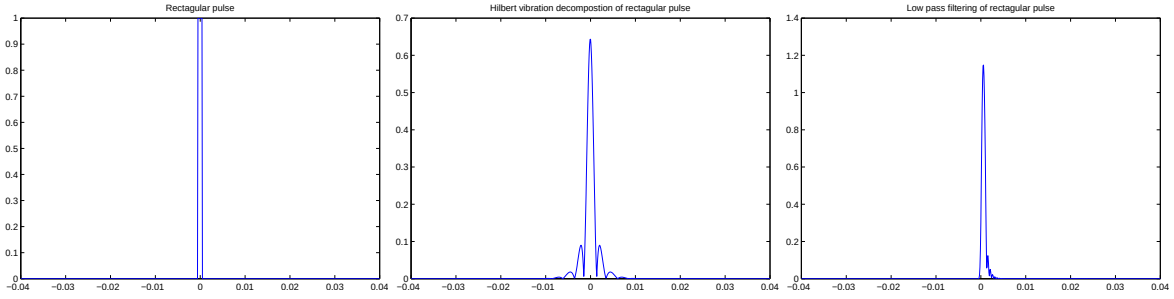

(a) (b) (c)

FIGURE 3.2: (a) Rectangular pulse, (b) Hilbert vibration decomposition of rectangular pulse and (c) Low pass filtering of rectangular pulse,

through the HVD happens to be the highest energy component of the original signal and it is instantaneous frequency based lowpass filtering of the signal. On the other hand, output signal obtained through the conventional lowpass filtering does not take the energy of the input/output signal into account and is based on frequency content of the input signal only. This signal energy dependent and instantaneous based filtering are the main advantages of the HVD over conventional lowpass filtering based pansharpening approaches.

The filtered PAN signal (first instantaneous amplitude component) can be used for injecting additional spatial information from PAN image into the MS/HS images for pansharpening purpose similar to other MRA based approaches. It may be observed that in the MRA based pansharpening approaches one has to take decisions regarding the choice of the wavelet function to be used and the type of filters (such as FIR/IIR) whereas in the proposed technique no such decisions are to be taken.

The block diagram of proposed scheme is shown in Fig.3.3. First MS/HS input image is co-registered to the PAN image and re-sampled to the pixel spacing of the PAN image by using interpolation [116].

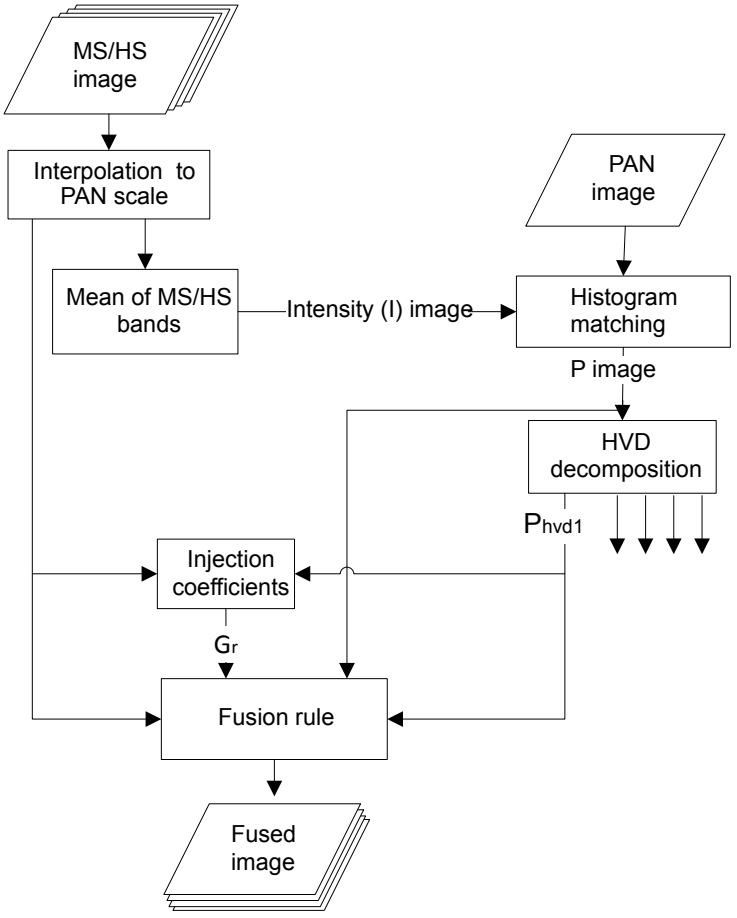

FIGURE 3.3: Block diagram of the proposed pansharpening scheme-I

Using given MS/HS images, the intensity (I) image is obtained by

$$I = \sum_{r=1}^{N} \frac{1}{N} \widetilde{MS}_r, \tag{3.6}$$

where $\widetilde{MS}_r$ are the rth MS images interpolated at the scale of PAN image and N denotes the total number of band images (the value of N is usually four to combine red, blue, green and infrared component images). The high spatial resolution PAN image is histogram matched with the I component of MS/HS image obtained by (3.6) to eliminate the effect of atmosphere, illumination, or sensor differences and the resulting histogram matched image P is obtained. Histogram matched image P is then converted into 1D vectors H_P by column ordering. The

vector H_P is decomposed using discretized version of (3.5) as given by

$$H_P(i) = \sum_j A_{P_j}(i) \cos(\sum_j \omega_{P_j}(i)), \tag{3.7}$$

where A_{P_j} is the instantaneous amplitude and ω_{P_j} is the instantaneous frequency (IF) of jth component.

Using (3.7), the first energy component of $H_P(i)$ vector is obtained as given below

$$H_{P_1}(i) = A_{P_1}(i) \cos\left(\sum \omega_{P_1}(i)\right). \tag{3.8}$$

Now convert the amplitude vector A_{P_1} appearing in (3.8) into images P_{hvd_1}, where P_{hvd_1} is the first image amplitude component of P image. Injection coefficients G_r are obtained from the regression coefficients between each of the MS bands and image P_{hvd_1}. The injection coefficients G_r are calculated as [66]

$$G_r = \frac{cov(\widetilde{MS}_r, P_{hvd_1})}{var(P_{hvd_1})}, r = 1, 2, ..., N, \tag{3.9}$$

where $var(P_{hvd_1})$ is the variance of P_{hvd_1} image and $cov(\widetilde{MS}_r, P_{hvd_1})$ indicates the covariance between two images $\widetilde{MS}_r$ and P_{hvd_1}.

Using (3.9), we propose the HVD based pansharpening model as follows

$$\widehat{MS}_r = \widetilde{MS}_r + \alpha\, G_r(P - P_{hvd_1}), r = 1, 2, ..., N, \tag{3.10}$$

where $\widehat{MS}_r$ is the pansharpened image with high spatial and spectral details and α is the tunning factor. Thus the relevant and additional spatial details available in the PAN image P are injected into the MS/HS image controlled by the tunning factor α giving us improved spatial

and spectral details as compared to the existing fusion techniques. The tunning factor α appearing in (3.10) can be optimized by single objective optimization technique using fitness function involving the quality metrics such as relative dimensionless global error in synthesis (ERGAS), spectral angle mapper (SAM) [31], [34], etc. In this scheme, we have used particle swarm optimization (PSO) technique and ERGAS as quality metric in the fitness function. The ERGAS is a measure of spatial distortion between the MS/HS and pansharpened images. Therefore the objective of optimization is to minimize the ERGAS metric to obtain the pansharpened image with minimum spatial distortion.

The steps of the proposed algorithm are summarized below.

Algorithm 1 HVD based pansharpening algorithm-I

1: Obtain up-sampled MS/HS images of the size of PAN image;
2: Compute the intensity image (I) using up-sampled MS/HS images by averaging;
3: Obtain histogram matched image (P) using input PAN and intensity image;
4: Compute the image P_{hvd_1} using HVD of P image;
5: Calculate the regression coefficients G_r for use in pansharpening model;
6: Obtained the high spatial and spectral resolution MS/HS image using pansharpening model $\widehat{MS}_r = \widetilde{MS}_r + \alpha\, G_r(P - P_{hvd_1}), r = 1, 2, ..., N$, where α is the tunning factor.
7: Optimize α using PSO for obtaining the minimum spatial distortion using objective function ERGAS.

3.3.1 Simulation Results

The simulations of the proposed pansharpening scheme for the multispectral and hyperspectral images are carried out in MATLAB and the results are given below:

Multispectral Pansharpening Results

To test the proposed HVD based pansharpening method, datasets collected by the Pleiades, IKONOS and GeoEye-1 satellites are used. The site locations selected for Pleiades, IKONOS,

(a) (b)

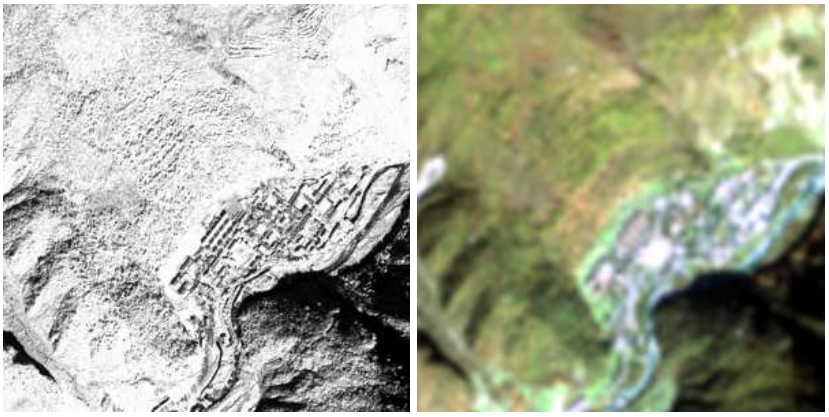

(c) (d)

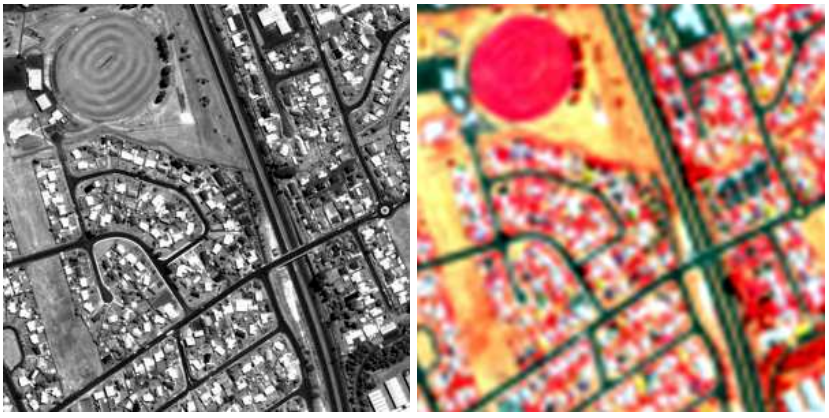

(e) (f)

FIGURE 3.4: PAN and EXP images for Pleiades, IKONOS and GeoEye-1 satellite datasets are (a) and (b), (c) and (d), (e) and (f) respectively.

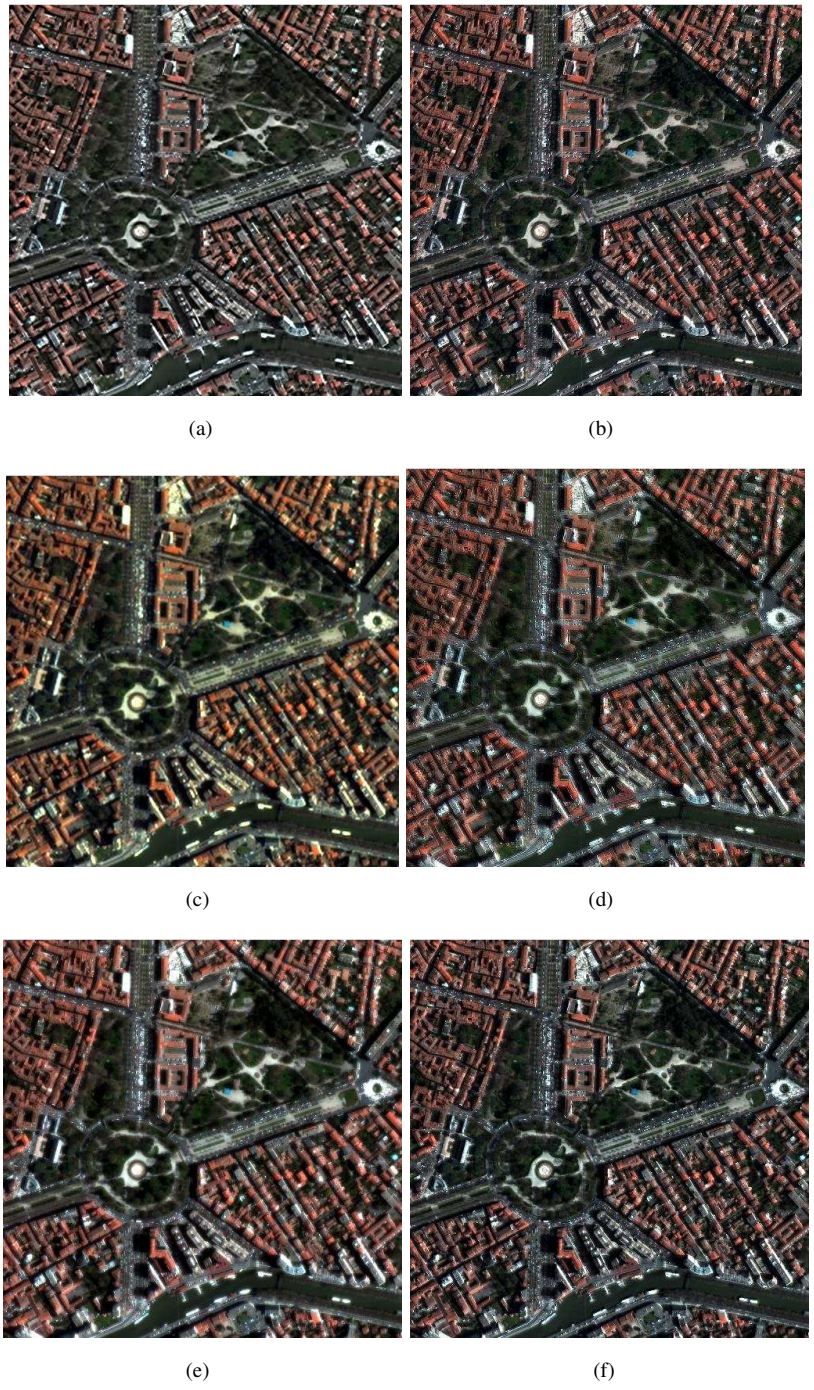

(a) (b)

(c) (d)

(e) (f)

FIGURE 3.5: Pansharpened images using different pansharpening methods for Pleiades satellite dataset are (a) Proposed HVD_F1 ($\alpha = 0.6628$), (b) OMF, (c) AIHS, (d) Indusion, (e) ATWTM2 and (f) MTF-GLP methods.

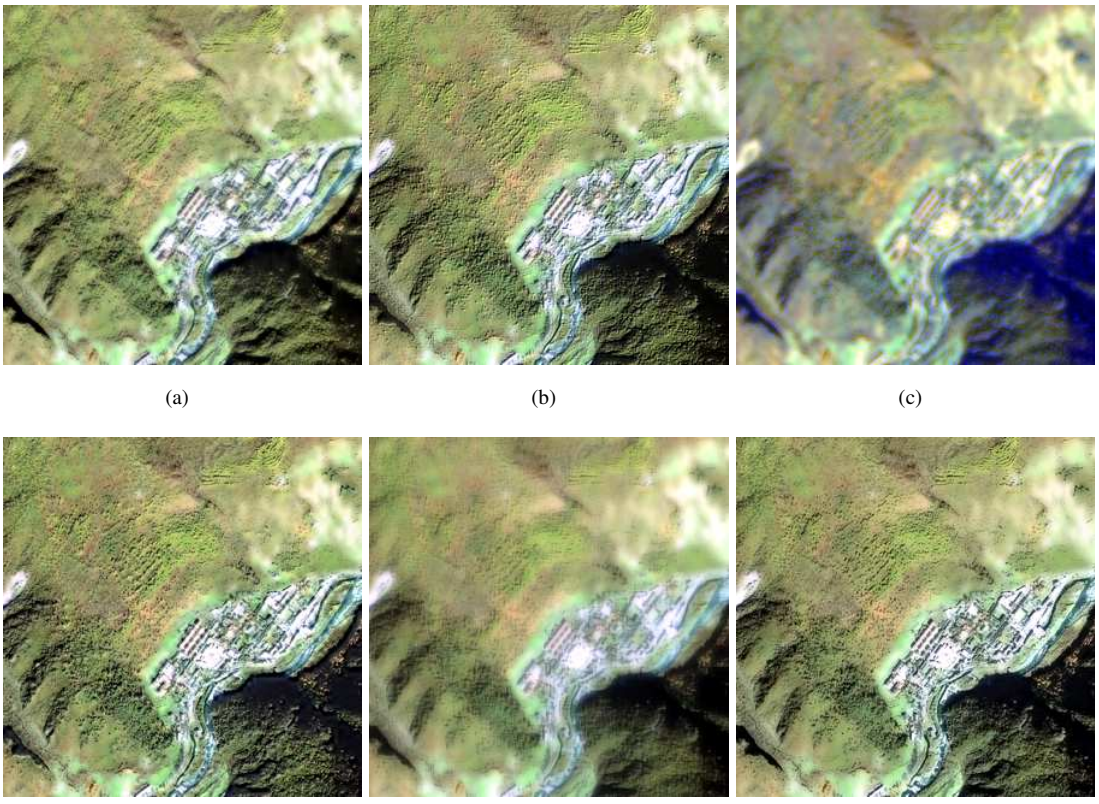

(a) (b) (c)

(d) (e) (f)

FIGURE 3.6: Pansharpened images using different pansharpening methods for IKONOS satellite dataset are (a) Proposed HVD_F1 ($\alpha = 0.4972$), (b) OMF, (c) AIHS, (d) Indusion, (e) ATWTM2 and (f) MTF-GLP methods.

GeoEye-1 satellite are Toulouse, France (2006) [32, 117], China-Sichuan (May, 2008) and Hobart, Tasmania, Australia (Feb, 2009) respectively. The spatial resolution of MS and PAN images for IKONOS satellite are 4 m and 1 m. Corresponding values for Pleiades and GeoEye-1 satellites are 60 cm and 80 cm, and 2 m and 0.5 m respectively. The size of MS images for IKONOS, Pleiades and GeoEye-1 satellites are 320×320, 1024×1024 and 320×320 respectively.

The tunning factor α in the proposed pansharpening model (3.10) is optimized by single objective PSO algorithm using fitness function involving quality metric ERGAS. The optimized

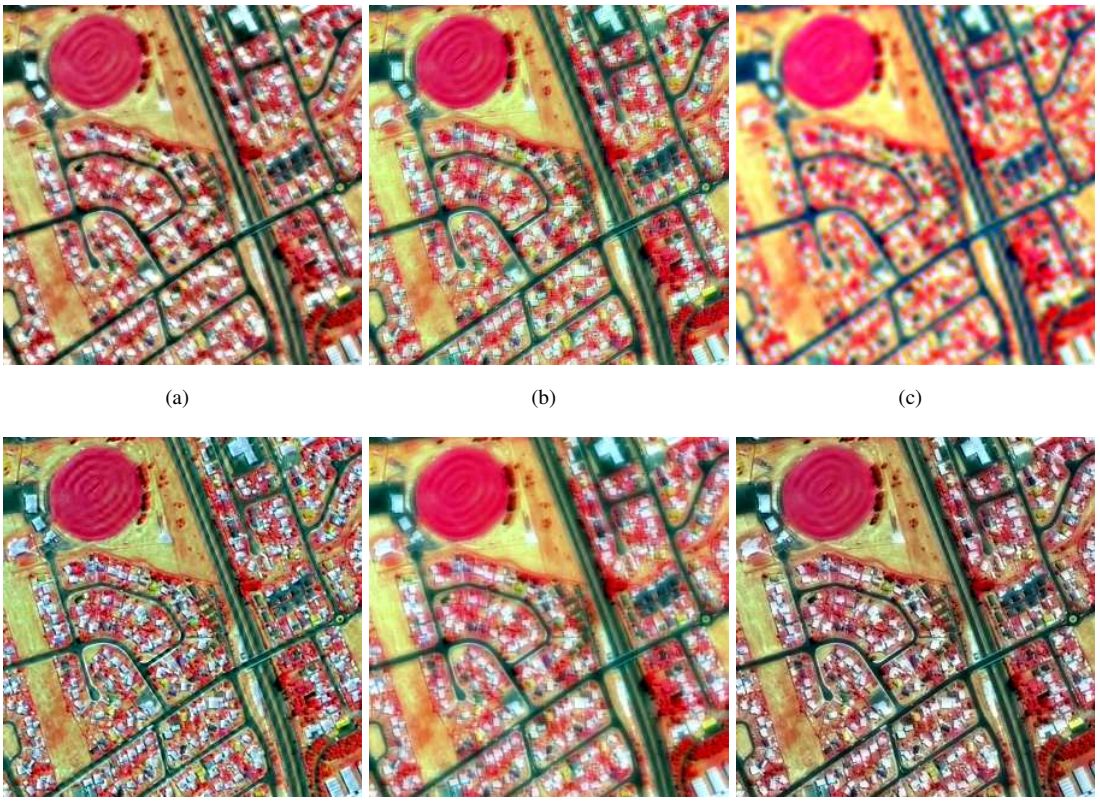

(a) (b) (c)

(d) (e) (f)

FIGURE 3.7: Pansharpened images using different pansharpening methods for GeoEye-1 satellite dataset are (a) Proposed HVD_F1 ($\alpha = 0.4564$), (b) OMF, (c) AIHS, (d) Indusion, (e) ATWTM2 and (f) MTF-GLP methods.

values of α obtained using PSO algorithm for Pleiades, IKONOS and GeoEye-1 satellite images are 0.6628, 0.4972 and 0.4564 respectively.

The input reference and the image obtained through the re-sampling of the MS image to the size of the PAN image using interpolation [116], labeled as EXP image, for Pleiades, IKONOS and GeoEye-1 satellites dataset are shown in the Fig.3.4(a)(b), 3.4(c)(d) and 3.4(e)(f) respectively. The pansharpened image obtained using proposed HVD scheme-I is labeled by HVD_F1 and these images obtained for Pleiades, IKONOS and GeoEye-1 satellites data set are shown in Fig.3.5(a), 3.6(a) and 3.7(a) respectively.

Simulations are also performed to compare the proposed pansharpening scheme with the existing pansharpening schemes based on optimal filter (OMF) [89], generalized Laplacian pyramid with modulation transfer function matched filter (GLP-MTF) [115], decimated wavelet transform using an additive injection model (Indusion) [118], adaptive IHS (AIHS) [5] and a trous wavelet transform using the model 2 (ATWTM2) [50]. The pansharpened images obtained by these methods are shown in Fig.3.5(b)-3.5(f), Fig.3.6(b)-3.6(f) and Fig.3.7(b)-3.7(f).

Qualitative observation of the pansharpened image shown in Fig.3.5(a) reveals additional spatial information than the pansharpened images obtained by the existing methods. Similarly spectral quality of the fused image shown in Fig.3.5(a) is better than the simulation results obtained by the other existing methods. Similar remarks hold good for the other set of images shown in Fig.3.6 and Fig.3.7. The proposed method generated fused images which are better matched in color information of the input MS images with improved edge information.

TABLE 3.1: The Spectral quality assessment of the pansharpened images for Pleiades data set ($\alpha = 0.6628$)

	Degraded scale			
	Q4	**SAM**	**ERGAS**	**Time(S)**
Ref.val.	1	0	0	0
HVD_F1	**0.9210**	4.7457	**4.1150**	19.97
OMF	0.8865	5.4812	4.7993	26.71
AIHS	0.8241	5.4395	5.8659	1.22
Indusion	0.8251	5.8322	5.6366	**1.06**
ATWTM2	0.8300	5.1505	5.4053	10.54
MTF-GLP	0.8786	5.2343	5.1103	6.78

The performance metrics Q-index, SAM, ERGAS and QNR for the images shown in Fig.3.5, 3.6 and 3.7 are computed and results obtained are tabulated in Tables 3.1, 3.2 and 3.3. It is seen from tabulated results using the proposed and existing techniques that the proposed method gives improved spatial as well as spectral quality of the MS image. The best values of the performance measures in tables are highlighted as bold face numerals.

TABLE 3.2: The Spectral quality assessment of the pansharpened images for IKONOS data set ($\alpha = 0.4972$)

	Degraded scale			Full scale		
	Q4	**SAM**	**ERGAS**	$\mathbf{D}_\lambda$	$\mathbf{D}_S$	**QNR**
Ref.val.	1	0	0	0	0	1
HVD_F1	**0.6583**	**3.0817**	**2.6049**	**0.1158**	**0.1409**	**0.7597**
OMF	0.5479	3.3195	3.0876	0.1548	0.2419	0.6407
AIHS	0.5245	4.4030	3.1710	0.2007	0.2125	0.6295
Indusion	0.5572	3.2295	2.9811	0.1728	0.2177	0.6472
ATWTM2	0.5968	3.2991	2.7752	0.1676	0.1930	0.6718
MTF-GLP	0.6287	3.2477	2.7783	0.2496	0.3606	0.4798

TABLE 3.3: The Spectral quality assessment of the pansharpened images for GeoEye-1 dataset ($\alpha = 0.4564$)

	Degraded scale			Full scale		
	Q4	**SAM**	**ERGAS**	$\mathbf{D}_\lambda$	$\mathbf{D}_S$	**QNR**
Ref.val.	1	0	0	0	0	1
HVD_F1	**0.7682**	**3.8888**	**2.8608**	0.0654	0.0976	**0.8434**
OMF	0.6656	4.4149	3.4972	**0.0412**	0.1243	0.8396
AIHS	0.5524	4.7684	3.3077	0.1401	0.1409	0.7388
Indusion	0.6420	4.2838	3.5680	0.0828	**0.0963**	0.8288
ATWTM2	0.6810	4.6050	3.1848	0.0840	0.1094	0.8157
MTF-GLP	0.7236	4.4309	3.1200	0.1984	0.2281	0.6188

Effect of Aliasing and Misregistration Errors

The effects of aliasing and mis-registration errors in the proposed methodology and existing pansharpening methods are evaluated for IKONOS satellite dataset given in Fig.3.5(b),(e) and the results are shown in Fig.3.8 and 3.9. It can be seen from Fig.3.8(a) that Q metric increases with increasing Nyquist frequency initially but becomes all most constant for higher Nyquist frequencies beyond 0.3 Hz. Similarly SAM in Fig.3.8(b) and ERGAS in Fig.3.8(c) varies upto the same Nyquist frequency of about 0.3 Hz but becomes insensitive to higher frequency values. For misregistration errors, it can be observed from Fig.3.9(a) that the parameter Q attains almost a constant value after the displacement error beyond 15m. On the other hand for parameter SAM shown in Fig.3.9(b) and ERGAS in Fig.3.9(c) the values have remained almost

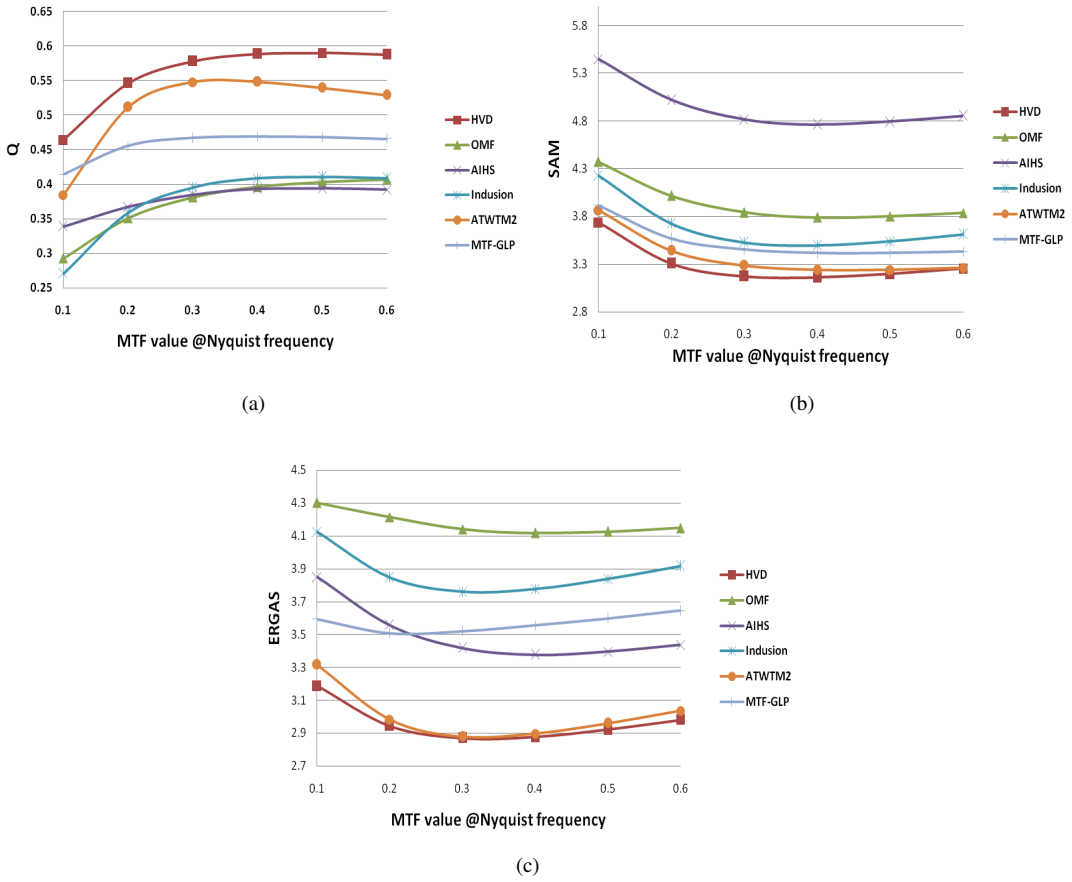

FIGURE 3.8: Quality/distortion indexes for increasing amounts of aliasing, measured by the amplitude at nyquist frequency of the Gaussian-like low-pass filter simulating the modulation transfer functions of the multispectral instrument using image Fig.3.6.

constant irrespective of displacement error. Thus it is observed that the proposed method provides better results and robustness against registration error and aliasing effect. The robustness of the proposed technique against misregistration and aliasing errors may be attributed to the higher energy in the first component of the HVD used in the pansharpening technique here.

To compare the HVD block in the proposed pansharpening scheme (shown in Fig.3.3) with other lowpass filtering techniques such as Gaussian lowpass filter (GLF) and the discrete wavelet transform (DWT) decomposition based lowpass signal (using Daubechies wavelet function).

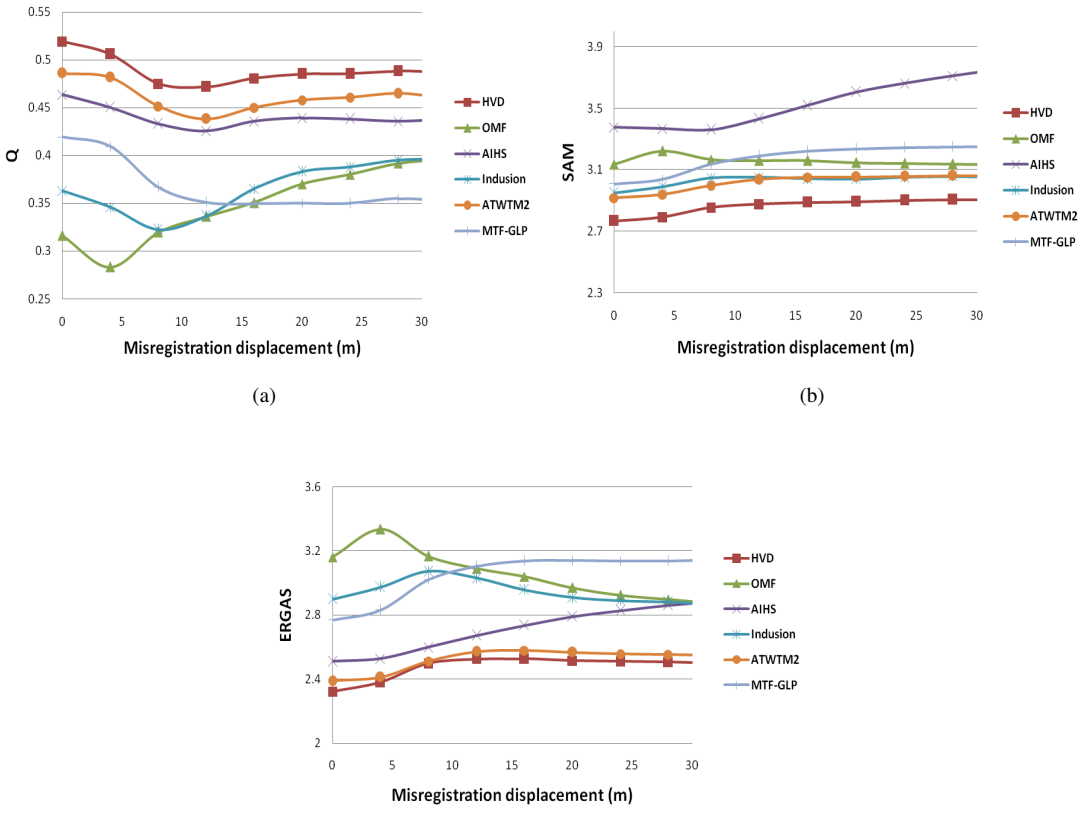

FIGURE 3.9: Quality/distortion indexes for increasing amounts of misregistration between MS and PAN images. Misregistration is measured in meters (32m=2 pels for IKONOS MS data at degraded spatial scale) using image Fig.3.6.

Simulation results have been performed for GeoEye-1 satellite dataset and obtained the pan-sharpened images using HVD, GLF and DWT in the proposed method are shown in Fig.3.10(a), 3.10(b) and 3.10(c) respectively. Qualitative observation of the image shown in Fig.3.10(a) reveals additional spatial information and spectral quality than the images obtained by the Fig.3.10(b)-3.10(c).

The performance metrics Q-index, SAM, ERGAS and QNR for the images shown in Fig.3.10 are computed, and results obtained are tabulated in Tables 3.4. It is seen that the proposed method provides better results in terms of all the quality metrics except QNR.

(a) (b) (c)

FIGURE 3.10: Pansharpened images for GeoEye-1 satellite dataset using (a) Proposed HVD_F1 ($\alpha = 0.4564$), (b) GLF and (c) DWT.

TABLE 3.4: The Spectral quality assessment of the pansharpened images for GeoEye-1 dataset ($\alpha = 0.4564$)

	Degraded scale			Full scale		
	Q4	**SAM**	**ERGAS**	$\mathbf{D}_\lambda$	$\mathbf{D}_S$	**QNR**
Ref.val.	1	0	0	0	0	1
HVD_F1	**0.7682**	**3.8888**	**2.8608**	0.0654	0.0976	0.8434
GLF	0.7378	3.9789	2.9238	0.0277	0.0425	0.9310
DWT	0.7020	4.1596	3.1382	**0.0081**	**0.0425**	**0.9497**

Hyperspectral Pansharpening Results

To test the proposed HVD based fusion method for HS image, the dataset collected by the Moffett field, CA, in 1994 by the JPL/NASA airborne visible/infrared imaging spectrometer (AVIRIS) [119] is used. The size of the reference image and spatial resolution are $185 \times 185 \times 176$ and 400 to 2500 nm respectively [35]. This image was initially composed of 224 bands that have been reduced to 176 bands after removing the water vapor absorption bands. This is a semisynthetic dataset where PAN image has been synthesized by averaging the first fifty bands of the reference image. The HS images for the pansharpening scheme have been generated by applying a Gaussian filter (with zero mean and standard deviation σ = 2.1) and downsampling operation into each band of the reference image [100].

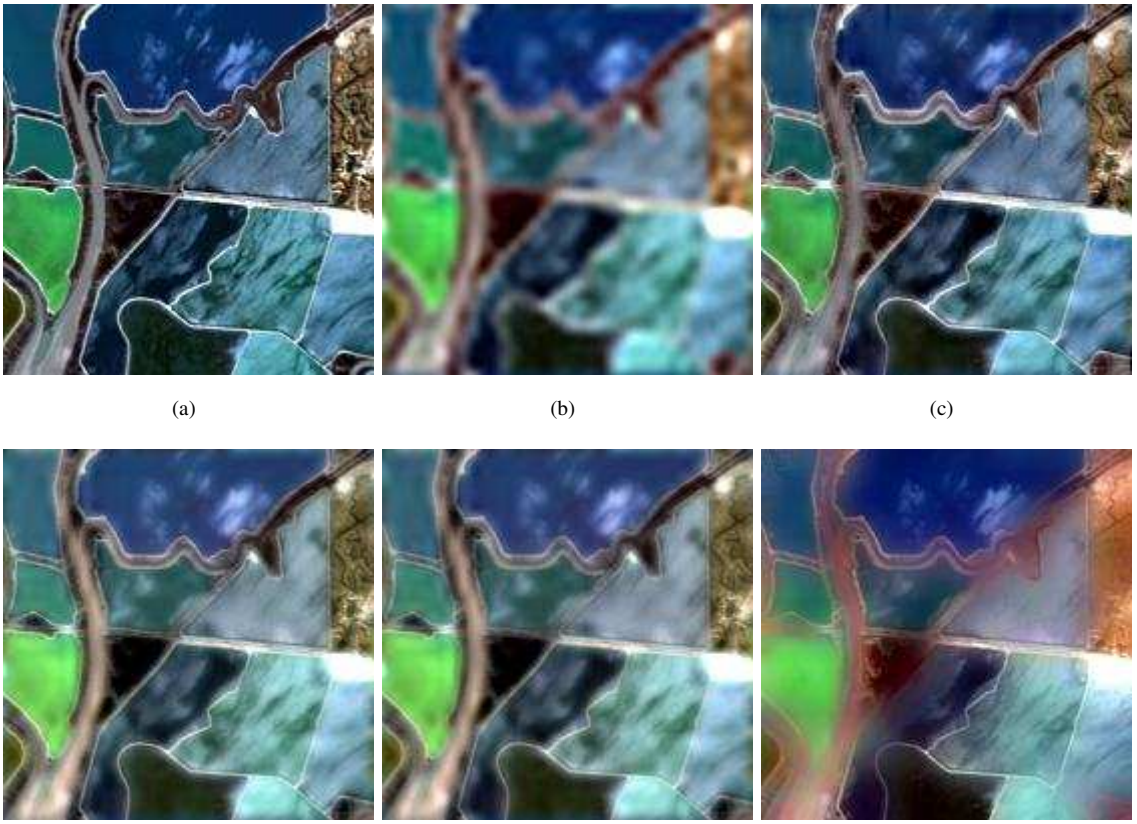

(a) (b) (c)

(d) (e) (f)

FIGURE 3.11: Pansharpened images using different pansharpening methods for AVIRIS HS satellite dataset are (a) Reference image, (b) EXP image, (c) Proposed HVD_F1 ($\alpha = 0.6$), (d) GS, (e) PCA and (f) GFPCA methods.

The optimized values of tunning factor α obtained using PSO algorithm is 0.6. The pansharpened image obtained using the proposed HVD method is labeled by HVD_F1 and image obtained through the re-sampling of the HS image to the size of the PAN image using interpolation [116] is labeled by EXP image. The input reference and EXP images for AVIRIS dataset are shown in the Fig.3.11(a) and 3.11(b) respectively.

Simulations are also performed to compare the proposed pansharpening scheme with the existing pansharpening schemes based on gram-schmidt transformation (GS) [63], principal component analysis (PCA) [64, 120] and guided filter PCA (GFPCA) [121]. Pansharpened images

for proposed and existing methods are shown in Fig.3.11(c) and Fig.3.11(d)-3.11(f) respectively. It can be observed from the image shown in Fig.3.11(c) that this pansharpened image provides additional spatial information than the pansharpened images obtained by the existing methods. Similarly spectral quality of the pansharpened image shown in Fig.3.11(c) is better than the simulation results obtained using other existing methods.

TABLE 3.5: The Spectral quality assessment of the pansharpened images for AVIRIS HS satellite dataset ($\alpha = 0.6$)

	Degraded scale		
	SAM	**ERGAS**	**PSNR**
HVD_F1	**12.1573**	**8.0314**	**28.3287**
GS	15.6685	10.6276	27.9004
PCA	16.8785	11.4708	27.7743
GFPCA	13.9946	12.0718	23.0541

The original HS images are used as reference for quality assessment. The quality metrics for evaluating the quality of the HS pansharpened images are SAM, ERGAS and PSNR, which are measured between reference images and the pansharpened images. The above mentioned performance metrics for the images shown in Fig.3.11 are computed and the results obtained are tabulated in Table 3.5. It is seen from tabulated results using the proposed and existing techniques that the proposed method gives improved spatial as well as spectral quality of the HS images. The best values of the performance measures are highlighted as bold face numerals. The proposed method generated pansharpened images which are better matched in spectral information with input HS images and provide improved spatial information.

3.4 Proposed Pansharpening Scheme-II

The basic objective of the pansharpening methods are to improve the spatial and spectral quality in the pansharpened image. In this section, HVD based hybrid pansharpening approach is proposed which is a modified scheme of HVD based pansharpening scheme-I [122]. The

work presented in the HVD based pansharpening scheme-I is based on multi-resolution analysis (MRA) approach whereas in the present methodology, it is based on hybrid approach of pansharpening scheme. The operation of obtaining instantaneous amplitude components of the

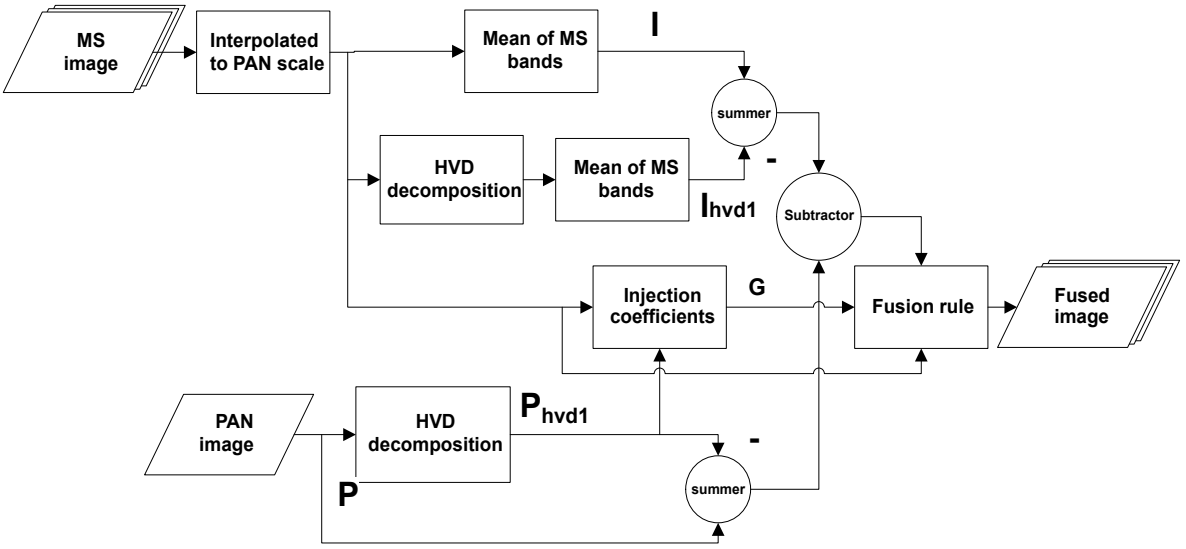

FIGURE 3.12: Block diagram of the proposed pansharpening scheme-II

signal through HVD can be considered as a lowpass filtered signal and has the highest energy of the original signal [122]. This is the main advantage of the HVD over conventional lowpass filtering. In the proposed scheme, the HVD filtered PAN and MS images (first instantaneous amplitude component) are used for injecting additional spatial information into the MS images for pansharpening purpose similar to the existing scheme [123].

The block diagram of the proposed scheme is shown in Fig.3.12. Here the input MS images are up-sampled and interpolated to the size of PAN image by using the scheme described in [116]. Using (3.6), intensity (I) image is obtained by given MS images. The interpolated MS images $\widetilde{MS}_r$ are converted into 1D vectors H_{MS_r} by column ordering and then vectors H_{MS_r} are decomposed using discretized version of (3.5) as given by

$$H_{MS_r}(i) = \sum_j A_{MS_{jr}}(i) \cos(\sum_j \omega_{MS_{jr}}(i)),\ r = 1, 2, ..., N, \tag{3.11}$$

where $A_{MS_{j_r}}$ are the instantaneous amplitudes and $\omega_{MS_{j_r}}$ are the instantaneous frequency (IF) of jth component.

Using (3.11), the first energy component of $H_{MS_r}(i)$ vectors are obtained as given below

$$H_{MS_{1_r}}(i) = A_{MS_{1_r}}(i) \cos\left(\sum \omega_{MS_{1_r}}(i)\right),\ r = 1, 2, ..., N. \tag{3.12}$$

Now the amplitude vectors $A_{MS_{1_r}}$ appearing in (3.12) are converted into images $\widetilde{M}_r$, where $\widetilde{M}_r$ images are the first amplitude component of $\widetilde{MS}_r$ images.

Using given $\widetilde{M}_r$ images, the intensity (I_{hvd_1}) image is obtained by

$$I_{hvd_1} = \sum_{r=1}^{N} \frac{1}{N} \widetilde{M}_r, \tag{3.13}$$

Similarly the HVD is applied on PAN image (P) using discretized version of (3.5) to obtain the first image amplitude component P_{hvd_1} of the P image. The injection coefficients G_r are obtained using (3.9).

Using (3.9), we propose the HVD based pansharpening model as follows

$$\widehat{MS}_r = \widetilde{MS}_r + \alpha\, G_r[(P - P_{hvd_1}) - \beta(I - I_{hvd_1})], r = 1, 2, ..., N, \tag{3.14}$$

where $\widehat{MS}_r$ is the pansharpened image with high spatial and spectral details and α, β are the tunning factors. Thus the relevant and additional spatial details are injected into the MS images controlled by the tunning factors α, β giving us improved spatial and spectral details as compared to the existing pansharpening techniques.

3.4.1 Simulation Results

The proposed pansharpening scheme tested on GeoEye-1 satellites dataset given in Fig.3.4(e)-(f) is used and for evaluating the pansharpening results, we follow the Wald's protocol [31]. The values of the tunning factor α, β in the proposed pansharpening rule (3.14) are 0.51, 0.55.

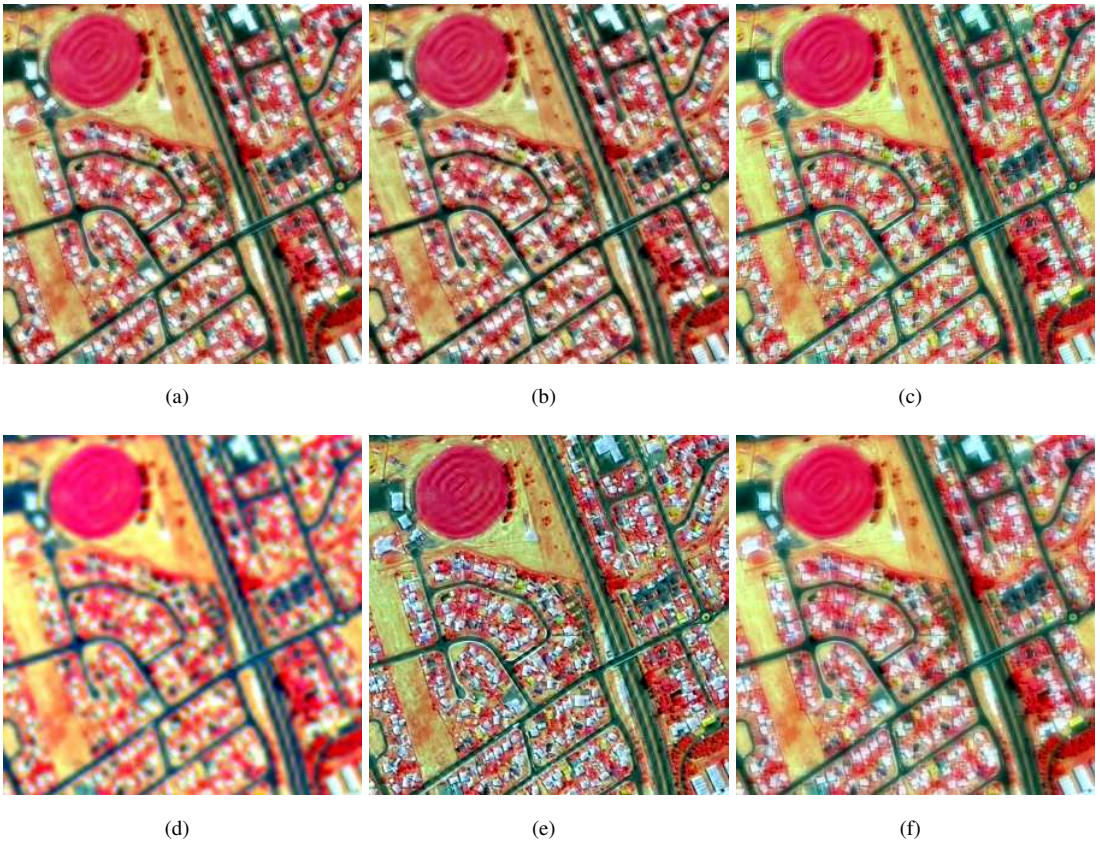

FIGURE 3.13: Pansharpened images obtained using proposed and existing pansharpening methods for GeoEye-1 satellite dataset are (a) Proposed HVD_F2, (b) HVD_F1, (c) OMF, (d) AIHS, (e) Indusion, (f) ATWTM2 methods.

They are obtained by the simulation trails. The input PAN and EXP images for GeoEye-1 satellite dataset are shown in Fig.3.4(e)-(f). The pansharpened image obtained using proposed scheme-II is labeled by HVD_F2.

Simulations are also performed to compare the proposed pansharpening scheme with the existing pansharpening schemes based on Hilbert vibration decomposition (HVD_F1) [122], optimal filter (OMF) [89], decimated wavelet transform using an additive injection model (Indusion) [118], adaptive IHS (AIHS) [5] and a trous wavelet transform using the model 2 (ATWTM2) [50]. The pansharpened images obtained by the proposed and existing methods are shown in Fig.3.13(a)-3.13(f). Qualitative observation of the pansharpened image shown in Fig.3.13(a) reveals that the fused image generated by the proposed method is better matched in color information of the input MS images with improved edge information.

TABLE 3.6: The Spectral quality assessment of the pansharpened images for GeoEye-1 dataset

	Degraded scale			Full scale		
	Q4	**SAM**	**ERGAS**	$\mathbf{D}_\lambda$	$\mathbf{D}_S$	**QNR**
Ref.val.	1	0	0	0	0	1
HVD_F2	**0.7693**	**3.8860**	**2.8589**	0.0798	0.1615	0.7716
HVD_F1	0.7682	3.8888	2.8608	0.0654	0.0976	**0.8434**
OMF	0.6656	4.4149	3.4972	**0.0412**	0.1243	0.8396
AIHS	0.5524	4.7684	3.3077	0.1401	0.1409	0.7388
Indusion	0.6420	4.2838	3.5680	0.0828	**0.0963**	0.8288
ATWTM2	0.6810	4.6050	3.1848	0.0840	0.1094	0.8157

The performance metrics Q4, SAM, ERGAS and QNR for the images shown in Fig.3.13 are computed and results obtained are tabulated in Table 3.6. It is seen from tabulated results using the proposed and existing techniques that the proposed method gives improved spatial as well as spectral quality of the MS image.

3.5 Proposed Image Fusion Scheme

The role of the image fusion in current image processing systems is increasing due to the growing variety of image acquisition techniques. Image Fusion is the process of combining substantial information from several sensors using mathematical techniques to create a single composite image that will be more comprehensive and thus, more useful for a human operator or other computer vision tasks. The latest technology in imaging sensors provides a broad kind of information that may be extracted from an located scene. Images which have been captured using different sensor modalities reveal numerous characteristics, such as a form of degradation, salient features, texture properties and many others. The automated procedure of conveying all the meaningful information from the input sensors to a final composite image is the goal of a fusion system, which appears to be an essential preprocessing stage for many applications, such as aerial and satellite imaging, medical imaging, robot vision and vehicle or robot guidance. In [77], proposed a generalized multisensor fusion using the gradient pyramid where image pyramid has been created by the pyramid transform. Using the basis functions of gradient-of-Gaussian pattern, the pyramid transform is applied to the input images. Two fusion rules are used to combine the information of the multiple decompositions at the locations where the source images are similar; the fusion is achieved by averaging two images, while if the images are significantly different, the fusion rule selects the feature pattern with maximum saliency and copies it for the fused image. In [80], author have demonstrated the use of a steerable pyramid for fusion of remote sensing images. The steerable pyramid is a multi-scale and multi-orientation decomposition with translation and rotation invariant sub-bands [81]. The low frequency or the coarsest approximation is fused based on the magnitude of the images at the corresponding locations. A region-based technique in a multi-resolution framework as an extension of the pixel-based technique [54]. This work provides multi-resolution fusion techniques. The input images are first segmented which is a preparatory step toward the actual fusion. The other quantity is the match measure which quantifies the similarity between

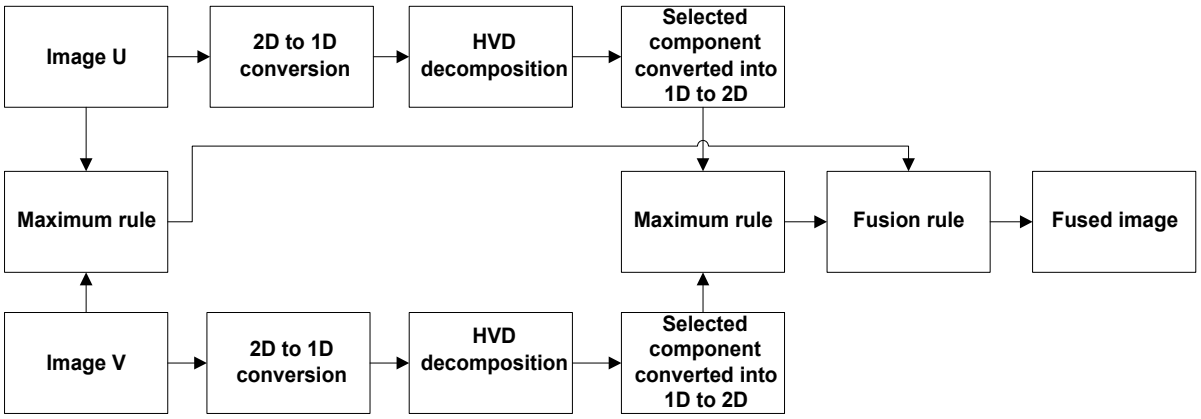

FIGURE 3.14: Block diagram of the proposed fusion scheme

the corresponding coefficients of the transformed images. This structure encompasses most of the pixel-based and region-based multi-resolution techniques. For an efficient fusion, the salient features from multi-scale image decomposition are extracted. The wavelet transform has proved to be a highly popular tool for fusion. A discrete wavelet transform (DWT)-based fusion technique offers distinct advantages such as orthogonality, compactness, and directional information [21]. Wavelet decomposition uses basis functions or different filters that are fixed and create influence in the fused image. In [21], the wavelet transforms experience problems when analyzing high frequency content, thus tending to lose spatial information. In [86], the EMD based image fusion method has been shown to give excellent performance as compared to the wavelet and PCA based approaches, particularly in retaining edge-based information from the different image modalities. A recent technique, Hilbert vibration decomposition (HVD) [38], analyses non-linear and non-stationary signals. It decomposes the input signal into amplitude and frequency components. The HVD method is based on the Hilbert transform (HT) presentation of the instantaneous frequency. The HVD has much higher frequency resolution than the EMD based approaches for signal decomposition [38, 117].

The block diagram of the proposed image fusion algorithm is illustrated in Fig.3.14, U and V source images are converted into column vectors H_U and H_V respectively. These vectors

are decomposed using discretized version of (3.5) as expressed by

$$H_U(n) = \sum_{m=1}^{2} A_{U_m}(n) \cos(\sum_{m=1}^{2} W_{U_m}(n)), \tag{3.15}$$

$$H_V(n) = \sum_{m=1}^{2} A_{V_m}(n) \cos(\sum_{m=1}^{2} W_{V_m}(n)), \tag{3.16}$$

where A_{U_m} and A_{V_m} are instantaneous amplitudes and W_{U_m} and W_{V_m} are the instantaneous frequencies (IF) of mth components of U and V images respectively. Using (3.15) and (3.16), the first and second components of each of the vectors, i.e., H_{U_1}, H_{U_2}, H_{V_1} and H_{V_2} are obtained.

The amplitude vectors A_{U_1}, A_{U_2}, A_{V_1} and A_{V_2} are converted into the images U_{hvd_1}, U_{hvd_2}, V_{hvd_1} and V_{hvd_2} respectively. Images U_{hvd_1} and V_{hvd_1} are the highest amplitude components of U and V images respectively which give most of the spatial information of the edges, while U_{hvd_2} and V_{hvd_2} images are the second highest amplitude components giving lesser spatial information of the edges as compared to first amplitude component. Now using the maximum selection rule on U_{hvd_1}, U_{hvd_2}, V_{hvd_1}, V_{hvd_2}, and U, V images as given by

$$UV_{hvd_l}(m,n) = \begin{cases} U_{hvd_l}(m,n), & if U_{hvd_l}(m,n) \geq V_{hvd_l}(m,n), l = 1,2 \\ V_{hvd_l}(m,n), & if U_{hvd_l}(m,n) < V_{hvd_l}(m,n) \end{cases} \tag{3.17}$$

$$UV(m,n) = \begin{cases} U(m,n), & if U(m,n) \geq (m,n), \\ V(m,n), & if U(m,n) < (m,n) \end{cases} \tag{3.18}$$

The fusion rule for obtaining fused images in the proposed method are given by

$$F(m,n) = UV(m,n) + \alpha UV_{hvd_l}(m,n), l = 1,2, \tag{3.19}$$

where F is the fused image and $\alpha = 0.01$. The fused image obtained by first decomposition component (l=1) is HVD_FS1 and for second decomposition component (l=2) is HVD_FS2.

3.5.1 Simulation Results

Simulation results of the proposed fusion method are obtained using MATLAB. It is applied on five pairs which are divided into two groups:

1. Multi-spectral images
    (a) Millimeter wave (MMW) and visible source images
    (b) Infrared (IR) and visible source images
    (c) MRI and CT source images
2. Multi-focus images and
    (a) Book source images
    (b) Clock source images

These image pairs are available at [124], which are widely used in different applications. These images are used to validate the efficacy of the proposed image fusion scheme. Simulation results of the proposed scheme are compared with existing image fusion schemes adaptive sparse representation (ASR) [125] and Discrete cosine harmonic wavelet transforms (DCHWT) [29] based image fusion schemes.

The first experiment is performed on multi-spectral images:

Concealed weapon detection (CWD) application is an important topic in the general area of law enforcement, and it appears to be a critical technology for dealing with terrorism, which seems to be the most significant law enforcement problem for the next decade. Since no single

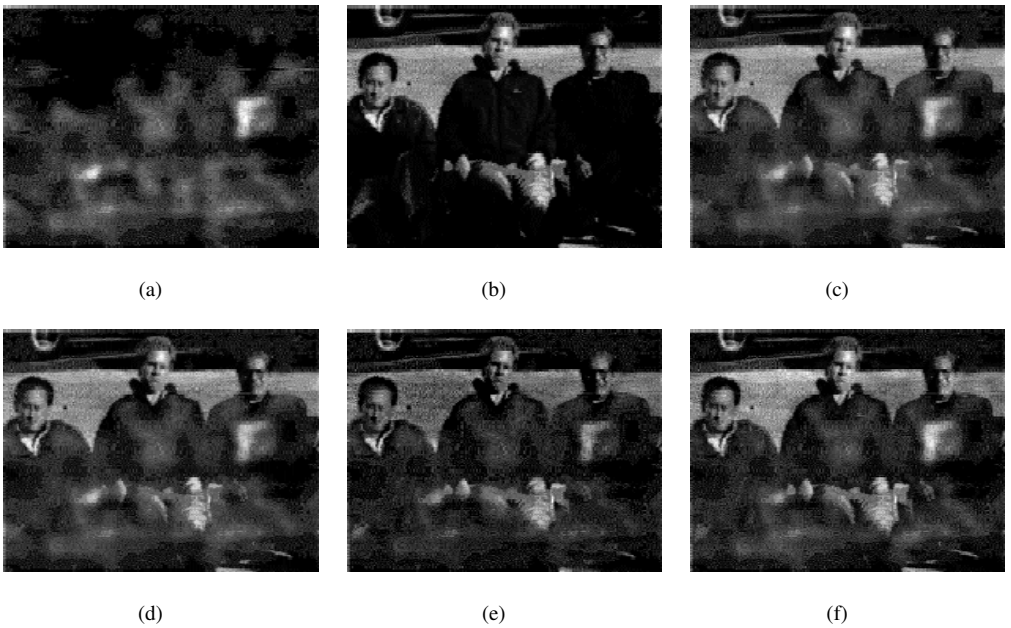

(a) (b) (c)

(d) (e) (f)

FIGURE 3.15: (a) MMW and (b) visible source images, fused image obtained by the (c) Proposed HVD_FS1, (d) Proposed HVD_FS2, (e) ASR and (f) DCHWT schemes

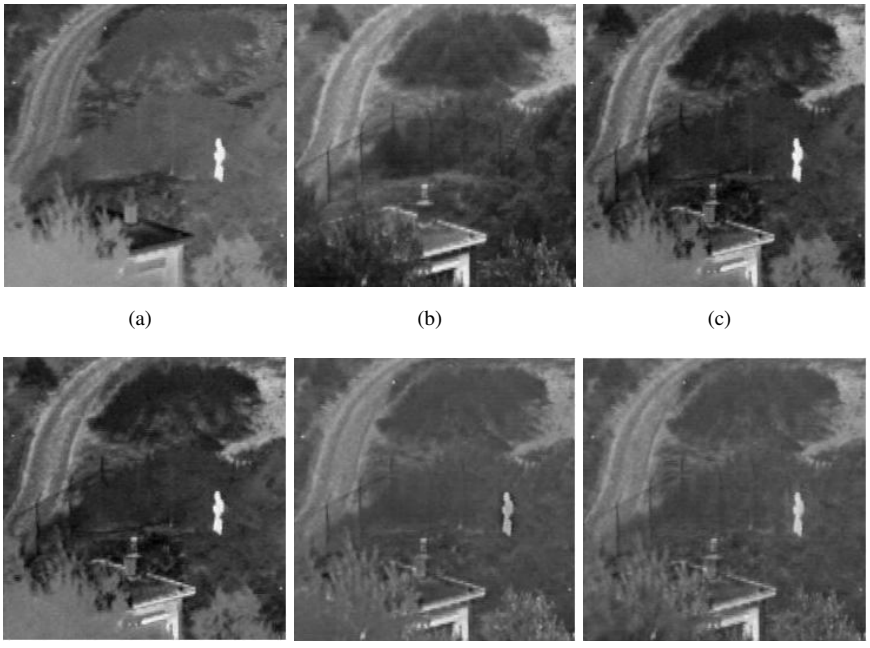

(a) (b) (c)

(d) (e) (f)

FIGURE 3.16: (a) IR and (b) visible source images, fused image obtained by the (c) Proposed HVD_FS1, (d) Proposed HVD_FS2, (e) ASR and (f) DCHWT schemes

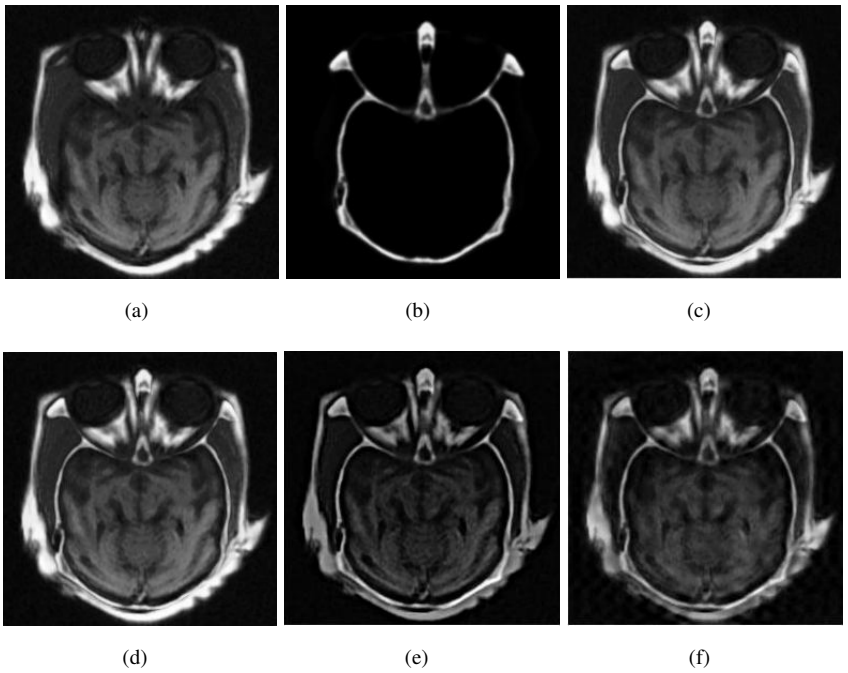

(a) (b) (c)

(d) (e) (f)

FIGURE 3.17: (a) MRI and (b) CT source images, fused images obtained by the (c) Proposed HVD_FS1, (d) Proposed HVD_FS2, (e) ASR and (f) DCHWT schemes

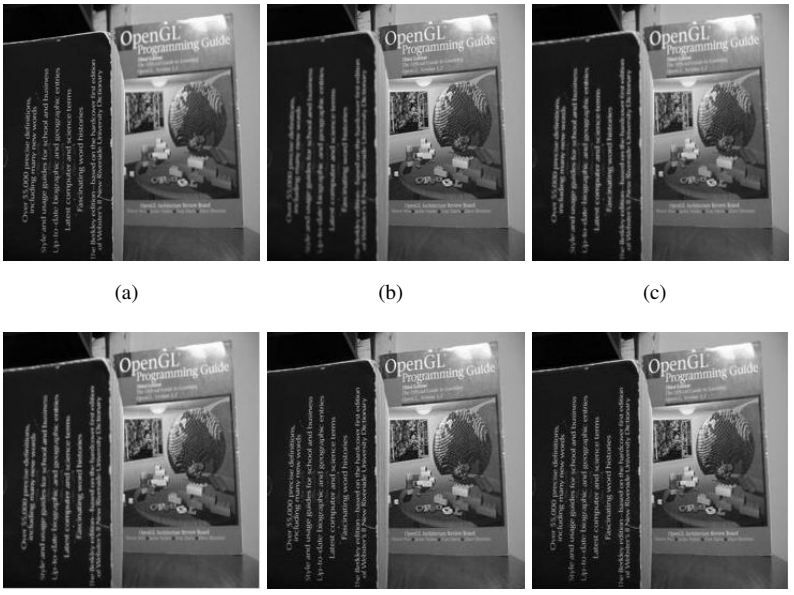

(a) (b) (c)

(d) (e) (f)

FIGURE 3.18: (a) and (b) Multi-focus Book source images, fused images obtained by the (c) Proposed HVD_FS1, (d) Proposed HVD_FS2, (e) ASR and (f) DCHWT schemes

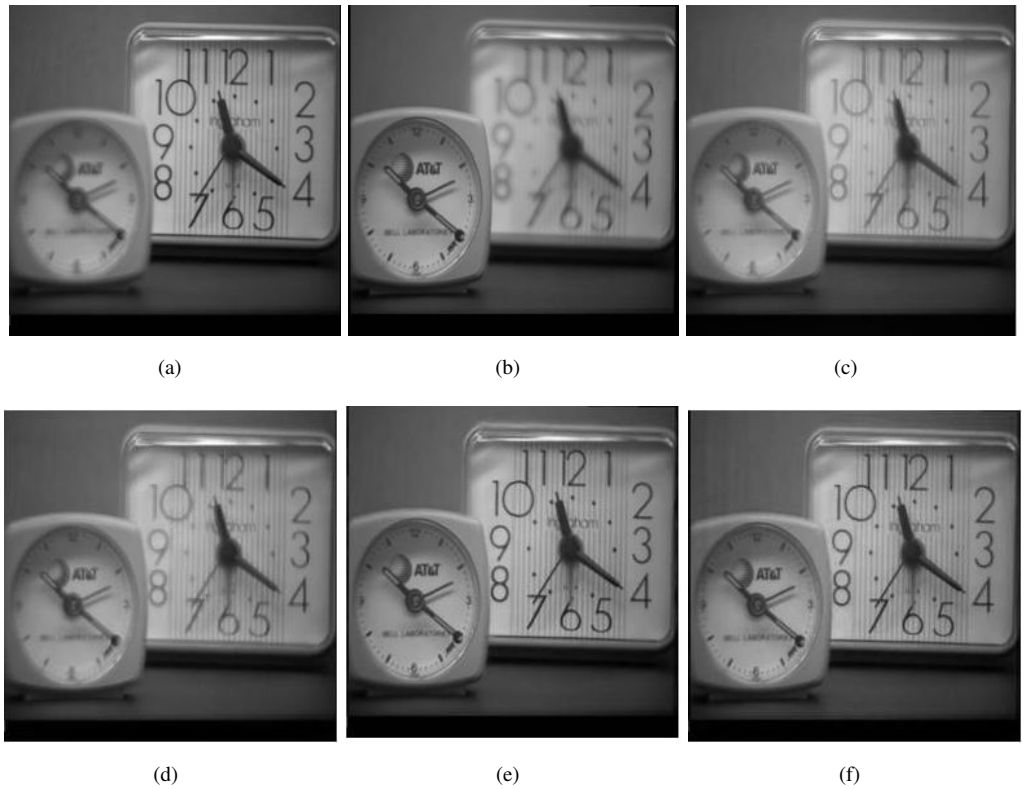

(a) (b) (c)

(d) (e) (f)

FIGURE 3.19: (a) and (b) Multi-focus Clock source images, fused images obtained by the (c) Proposed HVD_FS1, (d) Proposed HVD_FS2, (e) ASR and (f) DCHWT schemes

sensor technology can provide acceptable performance in CWD applications, image fusion has been identified as a key technology to achieve improved CWD procedures. Figs. 3.15(a), (b) show a pair of MMW and visual images. Fig.3.15(b) shows visual image, provides the outline and appearance of the people while the Fig.3.15(a) MMW image shows the existence of a gun. Fig.3.15(c)-(f)-the fused images obtained from the proposed and existing schemes show that there is considerable evidence to suspect that the person on the right has a concealed gun underneath his clothes. By observing Fig.3.15(c),(d), it is clear that the images obtained using the proposed fusion technique are better in visual appearance than the images obtained using the existing techniques.

Military surveillance application is a head-tracked vision system for night vision applications. The multiple imaging sensors employed can enhance a driver's overall situational awareness.

TABLE 3.7: Performance comparison of fused images

	API	SD	AG	H	MI	FS	CC	SF
MMW and visible source images								
HVD_FS1	**7.8499**	**6.5217**	**3.105**	**4.3959**	**3.3194**	1.9	0.668	**3.9212**
HVD_FS2	7.2199	6.084	3.0601	4.2804	3.8122	1.8919	0.6752	3.8754
ASR	4.183	3.953	2.6103	3.6018	1.6531	1.9122	**0.7009**	3.2981
DCHWT	5.4467	4.9544	2.7494	3.9545	1.7975	**1.9702**	0.6767	3.4529
IR and visible source images								
HVD_FS1	**122.8502**	**31.8585**	7.1818	**6.7979**	4.6808	**1.9289**	0.7712	9.8086
HVD_FS2	112.5993	30.0497	**7.214**	6.7159	**4.9378**	1.9239	0.7685	**9.8344**
ASR	90.7209	24.096	6.4558	6.3054	1.7018	1.8968	**0.7968**	9.1921
DCHWT	90.1042	24.696	6.7305	6.2967	1.6022	1.8344	0.7701	9.0485
MRI and CT source images								
HVD_FS1	**63.4209**	**63.2239**	**10.0173**	**6.7163**	4.6649	1.6188	0.6726	**17.8766**
HVD_FS2	58.7009	60.0945	9.9189	6.6073	**5.0771**	1.6205	0.6753	17.5533
ASR	31.4959	39.1903	8.3337	6.1865	2.7663	1.6602	**0.6919**	14.6749
DCHWT	38.0233	41.9861	8.0346	6.5888	1.9772	**1.7133**	0.6845	13.3888
Book source images								
HVD_FS1	**94.2561**	**63.7642**	14.6263	**7.473**	8.2588	1.9879	**0.9901**	23.7482
HVD_FS2	86.0642	59.2935	14.4392	7.3815	**8.5378**	1.986	0.99	23.4365
ASR	83.1806	59.3426	**16.7913**	7.3419	8.4621	**1.9904**	0.9893	**29.2452**
DCHWT	83.0109	59.1883	16.0855	7.3315	8.1143	1.9841	0.9901	27.7148
Clock source images								
HVD_FS1	**110.8424**	**54.152**	6.9568	**7.4939**	7.7809	**1.9862**	0.9869	10.5717
HVD_FS2	101.2756	50.4336	6.8822	7.3092	**7.8648**	1.9832	0.9874	10.515
ASR	96.9211	50.5028	**9.0741**	7.321	7.511	1.9579	0.9879	**15.4741**
DCHWT	96.6567	50.2248	8.8556	7.3868	7.0283	1.9693	**0.9888**	14.6276

Figs. 3.16(a), (b) image pair shows infrared (IR) and visible source images. In Figs. 3.16(a) scene includes a person, a road, a house, grass, and trees and shows the corresponding IR sensor image of the scene and Figs. 3.16(b) shows the visual sensor image of the same scene. These images contain complementary features as illustrated by the fused images shown in Figs. 3.16(c)-(f) which are obtained from the proposed and existing schemes. By observing Figs. 3.16(c),(d), it is clear that the image obtained using the proposed fusion technique is better in visual appearance than the images obtained using the existing techniques.

Medical diagnosis application, medical imaging has a computed tomography (CT) and magnetic resonance images (MRI) from the brain of the same patient. The goal of fusion scheme

TABLE 3.8: Performance comparison of fused images

	$Q^{UV/F}$	$L^{UV/F}$	$N^{UV/F1}$	ans
MMW and visible source images				
HVD_FS1	0.9043	0.0933	0.2216	1
HVD_FS2	0.9015	0.0972	0.1073	1
ASR	0.7907	0.2092	**0.0109**	1
DCHWT	**0.9241**	**0.0756**	0.0141	1
IR and visible source images				
HVD_FS1	0.6739	0.301	0.1768	1
HVD_FS2	0.6743	0.2962	0.195	1
ASR	**0.7345**	0.2621	**0.0166**	1
DCHWT	0.7335	**0.2612**	0.0189	1
MRI and CT source images				
HVD_FS1	0.8641	0.1249	0.5143	1
HVD_FS2	**0.8672**	**0.1223**	0.4241	1
ASR	0.8555	0.1426	**0.0286**	1
DCHWT	0.8145	0.182	0.0297	1
Book source images				
HVD_FS1	0.9791	0.0164	0.0174	1
HVD_FS2	0.9813	**0.0159**	0.0114	1
ASR	0.9704	0.0276	0.0077	1
DCHWT	0.978	0.0212	**0.0024**	1
Clock source images				
HVD_FS1	0.7354	0.2617	0.0199	1
HVD_FS2	0.735	0.2616	0.0214	1
ASR	0.9137	0.0833	**0.022**	1
CBF	**0.9257**	**0.0742**	5.67E-04	1

for the proposed example is to achieve a unique image with functional and anatomical information with the best resolution [25, 26, 27]. Figs. 3.17(a), (b) shows MRI and CT source image pairs. The fused images obtained using the proposed and existing schemes are shown in Figs. 3.17(c)-(f). From Figs. 3.17(c), (d), it is clear that in the proposed schemes the edges of the fused image are very clear and sharp as compared to the existing methods.

The second experiment is performed on multi-focus images:

Multifocus image fusion application is useful to enhance digital camera images. Figs. 3.18(a), (b) and Figs. 3.19(a), (b) show multi-focus book and clock image pairs of digital camera. In one image, the focus is on the left side. In the other image, the focus is on the right side. Figs. 3.18(c), (f) and Figs. 3.19(c), (f) show the fused images obtained using the proposed and existing schemes in which both the sides are in focus. By observing Fig.3.18(c), (d) and 3.19(c),

(d), it is clear that the fused images obtained using the proposed method are comparable to the images obtained using the existing techniques.

The performance of fused image is shown in Table 3.7 and 3.8. In section 2.6, performance parameters such as API, SD, AG, H, MI, FS, CC, SF, $Q^{UV/F}$, $L^{UV/F}$ and $N^{UV/F}$ are given. Using these parameters, the performance of the proposed and existing fusion methods is compared. In the Table 3.7 and 3.8, the best values of the performance measures are highlighted as bold-face numerals. It is observed from Table 3.7 and 3.8 that in majority of the experiments, the proposed scheme provides better results as compared to the existing schemes.

3.6 Conclusions

In this chapter, using the HVD technique two pansharpening and one image fusion schemes are presented. The proposed pansharpening scheme-I is also extended for the HS images and proposed scheme-II is the modified approach of scheme-I. The pansharpening scheme-I is based on multi-resolution analysis (MRA) approach whereas scheme-II is based on a hybrid approach. The tunning factor associated with the pansharpening model is optimized by single objective PSO algorithm. Experimental results of the proposed techniques demonstrate that the proposed fusion schemes have improved spectral and spatial quality as compared to the existing schemes. The effects of aliasing and misregistration errors on our proposed methods are also investigated and it is observed that the proposed methods are robust against aliasing and misregistration errors as compared to other existing methods. In the proposed image fusion scheme, first and second highest amplitude component of the decomposition of the source images are used to generate the fused image using fusion rule. It is seen that the performance of the proposed scheme provides better simulation results when the first highest amplitude component (l=1) is used to generate the fused image. Performance evaluation of fused images is done by computing fusion quality metrics and the results are compared with other existing fusion schemes and it is observed that the proposed image fusion scheme is an efficient technique for improving the

visual appearance and it provides a robust system performance, compact representation of information in different applications like remote sensing, medical imaging, military surveillance and concealed weapon detection, etc.

Chapter 4

Fractional Fourier Transform Based Image Fusion/Pansharpening Schemes

In this chapter, new approaches for fusion/pansharpening based on 2D-discrete fractional Fourier transform (2D-DFRFT) are proposed. The 2D-DFRFT is a generalized version of the conventional Fourier transform which provides the representation of a given signal in intermediate domains between spatial and fast Fourier transform (FFT) domains. The angle parameters associated with the 2D-DFRFT provide additional degrees of freedom. Smaller values of angle parameters of a signal are similar in shape to the low pass filtered version of a signal and hence it can be considered as fractional domain filtering of the signal. The 2D-DFRFT provides different representations of the given signal/image corresponding to different angles which can be optimized for better results. Using 2D-DFRFT, three novel image fusion/pansharpening approaches in which two pansharpening and one image fusion schemes are presented, which improves the spatial and spectral quality of the fused image. The structure of this chapter is as follows: In section 4.1, introduction and brief literature review is presented; in Section 4.2, the details of the FRFT and PSO methods are explained; Section 4.3 provides details of the proposed pansharpening scheme-I and simulation results which provides a comparative analysis

of the proposed scheme with existing schemes; Section 4.4 describes details of the proposed pansharpening scheme-II with simulation results; Section 4.5 describes the proposed image fusion method with simulation results which gives a comparative analysis of the proposed scheme with existing schemes. Conclusions are drawn in Section 4.6.

4.1 Introduction

Many of the remote sensing satellites, such as SPOT, IRS, Landsat 7, IKONOS, QuickBird, Pléiades, and Worldview-2, capture a lot of images for topographic mapping and map updating, land use, agriculture and forestry, flood monitoring, ice and snow monitoring etc. These images can be categorized into multi-spectral (MS) and panchromatic (PAN) images. The MS images have high spectral resolution and low spatial resolution while PAN image has high spatial resolution and low spectral resolution of the same captured area [126]. It is difficult to obtain an image directly from the satellite sensors having both high spatial and spectral resolution of the captured area due to some technical constraints [127]. Many pansharpening schemes have been proposed for achieving the goal of high spatial and spectral resolution in a single image [128]. A fast Fourier transform (FFT) based pansharpening scheme is proposed in [87]. This method is based on IHS transform with FFT filtering of both the PAN image and intensity image component of the original MS images; one of the drawbacks of this algorithm is that original MS images have to contain only three bands. It reduces the general applicability of this algorithm to very few cases like LANDSAT and SPOT satellite images in which multispectral sensor has three bands of the visible spectrum and a fourth band on the infrared. The infrared sensor has a spatial resolution much lower than the three visible sensors. It is usually discarded for tasks related to the production of visual products or applications [71]. It may be mentioned here that due to finite spatial size of MS and PAN images, these images will not be band limited in FFT domain and therefore FFT based pansharpening may not be suitable in such cases. In addition, the PAN and MS images collected through different sensors satellite environment suffer from different types of noise which may not be stationary in nature. Therefore conventional Fourier

transform is not suitable for handling such non-stationary signals and noise [129, 130]. The fractional Fourier transform (FRFT) is known to handle such non-stationary noise in a more effective way than the conventional Fourier transform [131]. It would, therefore, be interesting to investigate the intermediate domains (known as FRFT domains) between spatial and FFT domains for pansharpening purpose. The FRFT is a generalized version of the conventional Fourier transform. The angle parameter of 2D-DFRFT can be varied to provide infinite representations of the given signal in different 2D-DFRFT domains, each corresponding to different values of the angle parameter. The 2D-DFRFT provides a free degree of freedom in terms of its angle parameters. The 2D-DFRFT has been applied in many image processing applications [39, 40, 41, 42, 43, 44, 45, 46, 47] but the use of discrete fractional Fourier transform (DFRFT) in pansharpening has not been investigated so far.

4.2 Review of FRFT and PSO

4.2.1 FRFT

The fractional Fourier transform (FRFT) is a generalization of the conventional Fourier transform [132] and has attracted a lot of attention of the researchers in different applications [41, 42, 43]. The FRFT is a linear operator which provides a representation of the signal along the axis making an angle α with the time axis [133] and it reduces to conventional Fourier transform for an angle parameter equal to $\pi/2$.

The 2D continuous FRFT with the orders a'_u for the u' axis and a'_v for the v' axis, for $0 < |a'_u| < 2$ and $0 < |a'_v| < 2$, respectively, is defined as [132]

$$\mathcal{F}_{\alpha,\beta}(u,v) = \int_{-\infty}^{\infty}\int_{-\infty}^{\infty} f(u',v')K_{\alpha,\beta}(u',v',u,v)du'dv', \tag{4.1}$$

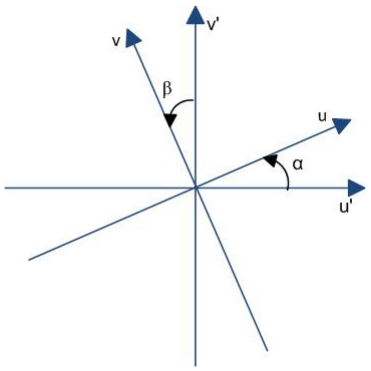

FIGURE 4.1: Time-frequency plane and a set of coordinates (u, v) rotated by an angles α and β relative to the original coordinates (u', v').

$$K_{\alpha,\beta}(u', v', u, v) = K_{\alpha}(u', u)K_{\beta}(v', v), \tag{4.2}$$

$$K_{\alpha}(u', u) = A_{\alpha}exp[i\pi(u'^2 cot\alpha - 2u'ucsc\alpha + u^2 cot\alpha)], \tag{4.3}$$

$$K_{\beta}(v', v) = A_{\beta}exp[i\pi(v'^2 cot\beta - 2v'vcsc\beta + v^2 cot\beta)], \tag{4.4}$$

$$A_{\alpha} = \frac{exp[-i(\pi\hat{\alpha}/4 - \alpha/2)]}{(|sin\alpha|)^{\frac{1}{2}}}, \tag{4.5}$$

$$A_{\beta} = \frac{exp[-i(\pi\hat{\beta}/4 - \beta/2)]}{(|sin\beta|)^{\frac{1}{2}}}, \tag{4.6}$$

where $\alpha = a'_u\pi/2$, $\beta = a'_v\pi/2$, $\hat{\alpha} = sgn(\alpha)$ and $\hat{\beta} = sgn(\beta)$. The angles α and β appearing in (4.1) provide additional degree of freedom in the 2D continuous FRFT domain representation of signals which can be optimized in specific applications.

The algorithms for 2D-discrete FRFT (2D-DFRFT) have also been proposed [132] and have obtained similar results as those of 2D continuous FRFT as given in (4.1).

The 2D-DFRFT transform of input image $h(i, j)$ of size $A \times B$ is computed as

$$H_{\alpha,\beta}(m,n) = \mathcal{F}_{\alpha,\beta}[h(i,j)] = \sum_{i=0}^{A-1}\sum_{j=0}^{B-1} h(i,j)\mathcal{R}_{\alpha,\beta}(i,j,m,n) \tag{4.7}$$

where $\mathcal{R}_{\alpha,\beta}(i,j,m,n)$ is the 2D transform kernel defined as

$$\mathcal{R}_{\alpha,\beta} = \mathcal{R}_{\alpha} \otimes \mathcal{R}_{\beta}, \tag{4.8}$$

where $\mathcal{R}_{\alpha}, \mathcal{R}_{\beta}$ are the 1D-DFRFT transformation matrix and symbol $\otimes$ denotes Kronecker product of matrices given in [134, 135]. The angle parameters α and β appearing in (4.7) can also be varied for obtaining better signal representation.

For $\alpha = \beta = \pi/2$, the 2D-DFRFT reduces to the conventional 2D-discrete Fourier transform (2D-DFT) while for $\alpha = \beta = 0$, the 2D-DFRFT provides the original signal itself.

The inverse 2D-DFRFT is computed as

$$h(i,j) = \sum_{m=0}^{A-1}\sum_{n=0}^{B-1} H_{\alpha,\beta}(m,n)\mathcal{R}_{-\alpha,-\beta}(i,j,m,n), \tag{4.9}$$

4.2.2 PSO

The particle swarm optimization (PSO) is a population based search algorithm similar to the other swarm techniques. It is inspired by the food searching techniques employed by birds. The main features of PSO technique include ease of implementation, robustness to control parameters, and computational efficiency as compared with other existing heuristic algorithms such as genetic algorithm in a continuous problem [136]. It is well-known that PSO technique can be applied to non-differentiable, non-linear, huge search space problems giving better results with good efficiency [136]. This optimization technique has been employed to solve complex problems in various application areas, such as image segmentation [137], image watermarking [138] and image pansharpening [139].

In this approach a set of random solutions are selected as particles and each particle is associated with certain velocity. The performance of each particle is evaluated based on some fitness function. Design of the algorithm begins with initialization of particles and let N_v denote the population size. The position and velocity of kth particle are D-dimensional vectors $P^k = (P_1^k, P_2^k, P_3^k, ...P_D^k)$ and $v^k = (v_1^k, v_2^k, v_3^k, ...v_D^k)$ respectively, where $k = 1, ...N_v$ and D the search space dimensionality. The velocity and position are updated in order to achieve an optimal solution using

$$v_j^k(t+1) = w.v_j^k(t) + c_1.r_1.(P_L(t) - P_j^k(t)) + c_2.r_2.(P_G(t) - P_j^k(t)), \tag{4.10}$$

$$P_j^k(t+1) = P_j^k(t) + P_j^k(t+1), j = 1, 2, ..D, \tag{4.11}$$

where w is the linear decreasing inertia weight [140], [136] controlling the influence of previous velocities on the current velocities, c_1 and c_2 are learning factors that control the contribution of cognitive and social information to the local and global solutions, respectively and r_1 and r_2 are random values distributed between 0 and 1, parameter t is the iteration counter, $v_j^k(t)$ and $P_j^k(t)$ are the current velocity and position of the kth particle and $v_j^k(t+1)$ and $P_j^k(t+1)$ are the updated velocity and position of the kth particle, $P_L(t)$ is the local best position of the kth particle and $P_G(t)$ is the global best position among the whole particles in the swarm. The design of the algorithm is based on both social and personal factors that decide the convergence [141, 142].

4.3 Proposed Pansharpening Scheme-I

The images captured from different sensors in remote sensing applications may suffer from spatial and spectral distortion problems. Some pansharpening schemes improve the spatial quality and reduce the spectral distortion in the pansharpened image obtained from the MS and PAN images by performing filtering in time domain or joint time-frequency domains [50].

These filtering based pansharpening schemes however assume that the image is band limited in conventional Fourier domains. However the finite size of the images acquired precludes this assumption to hold true. Therefore it would be interesting to extend the filtering based pansharpening approach to intermediate domains called FRFT domains.

In this section we present pansharpening scheme for remote sensing images using 2D-DFRFT based filtering scheme. The proposed technique is closer to the MRA approach and the filtering provided in the proposed method is totally different than conventional filtering approaches based on wavelet transform. The motivation for this also stems from the fact that the absolute value of 2D-DFRFT of a signal (for smaller values of angle parameters) is similar in shape to the low pass filtered version of a signal.

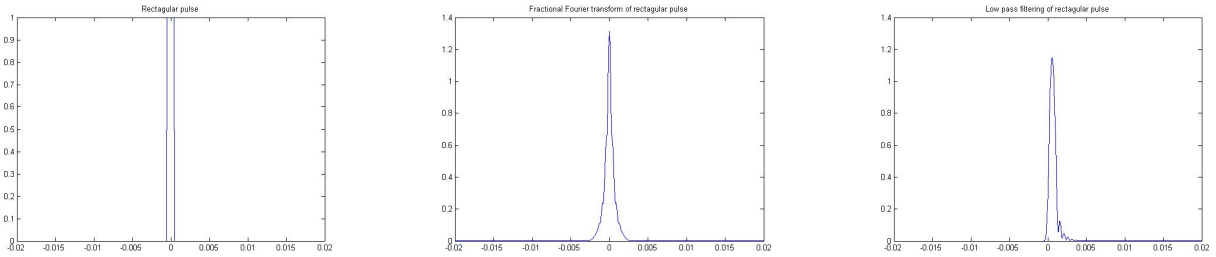

(a) (b) (c)

FIGURE 4.2: (a) Rectangular pulse, (b) Fractional Fourier transform of rectangular pulse, (c) Low pass filtering of rectangular pulse

To explain the point further, the rectangular pulse and absolute value of its 2D-DFRFT is shown in Fig.4.2 (a) and 4.2(b) respectively. The output of the Butterworth low pass filter with rectangular pulse as input is shown in Fig.4.2(c). It is clear from these figures that the shape of the signals in Fig.4.2(b) and (c) is very close to each other and hence low pass filtering can be implemented and approximated using the 2D-DFRFT technique. This lowpass filtering can also be considered as fractional domain filtering of the signal [131]. Thus fractional domain filtered PAN signal can be used for injecting additional spatial information from PAN image into the MS images for pansharpening purpose similar to other MRA based approaches.

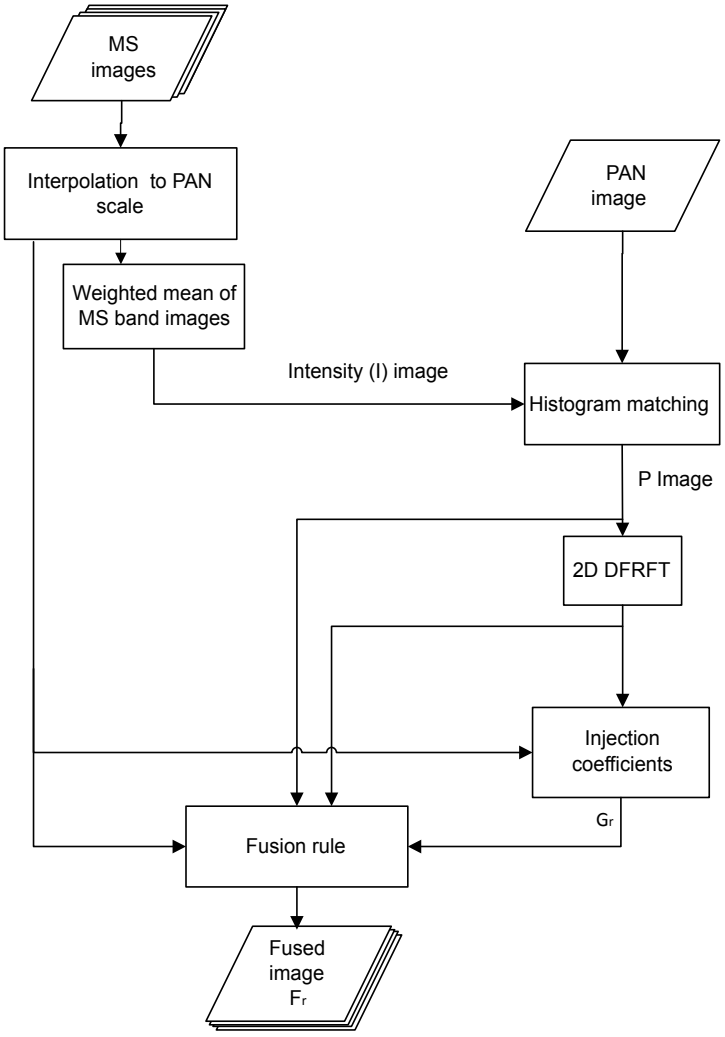

FIGURE 4.3: Block diagram of the proposed panshapening scheme

It is worthwhile to mention that in the wavelet based MRA approach the pansharpening results vary from the wavelet function chosen for filtering purpose. One has to take decisions regarding the filter specifications such as type of filters (FIR/IIR) whereas in the proposed technique no such decisions are to be taken. The additional advantage of 2D-DFRFT based pansharpening approaches is that different representations of the given signal/image corresponding to different angles can be used for obtaining better pansharpening results.

The block diagram of the proposed method is given in Fig.4.3. Here MS input images are up-sampled and interpolated to the size of PAN image by using the scheme described in [116].

Using these interpolated MS images, intensity (I) image is obtained from

$$I = \sum_{r=1}^{N} \alpha_r \widetilde{MS}_r, \tag{4.12}$$

where α_r are weighting coefficients and $\widetilde{MS}_r$ are the rth MS images interpolated at the scale of PAN image and N denotes the total number of band images (the value of N is usually four to combine red, blue, green and infrared component images). These weighting coefficients α_r can be selected in different ways as discussed in [32]. In the present work we have chosen to compute this weight coefficient using the method given in [5] because this method is known to provide improved spectral resolution.

The high spatial resolution PAN image is histogram matched with the I image for preserving radiometry [143] and the resulting histogram matched image is denoted by P. Histogram matched image P is then transformed using 2D-DFRFT defined in (4.7) as given below:

$$\hat{P}_{\alpha_1,\beta_1}(m,n) = \left|\mathcal{F}_{\alpha_1,\beta_1}[P(i,j)]\right| = \left|\sum_{i=0}^{A-1}\sum_{j=0}^{B-1} P(i,j)\mathcal{R}_{\alpha_1,\beta_1}(i,j,m,n)\right|, \tag{4.13}$$

where $\hat{P}_{\alpha_1,\beta_1}$ is the magnitude of the 2D-DFRFT domain representation of image P corresponding to angles $\alpha_1 = a_1\pi/2$ and $\beta_1 = b_1\pi/2$.

Using (4.13), we propose the following pansharpening rule as

$$\widehat{MS}_{r(\alpha_1,\beta_1)} = \widetilde{MS}_r + \gamma G_r(P - \hat{P}_{\alpha_1,\beta_1}),\ r = 1, ..., N, \tag{4.14}$$

where $\widehat{MS}_{r(\alpha_1,\beta_1)}$ is the fused image with high spatial and spectral details, γ is a constant whose value will be determined experimentally for images obtained from different satellites, G_r are the injection coefficients obtained from the regression between each MS band image and image

$\hat{P}_{\alpha_1,\beta_1}$ [32]. The injection coefficients are calculated using

$$G_r = \frac{cov(\widetilde{MS}_r, \hat{P}_{\alpha_1,\beta_1})}{max(var(\widetilde{MS}_r), var(\hat{P}_{\alpha_1,\beta_1}))}, r = 1, ..., N, \tag{4.15}$$

where $var(\widetilde{MS}_r)$ and $var(\hat{P}_{\alpha_1,\beta_1})$ are the variance of $\widetilde{MS}_r$ and $\hat{P}_{\alpha_1,\beta_1}$ images respectively and $cov(\widetilde{MS}_r, \hat{P}_{\alpha_1,\beta_1})$ indicates the covariance between two images $\widetilde{MS}_r$ and $\hat{P}_{\alpha_1,\beta_1}$. The quality of pansharpened image $\widehat{MS}_{r(\alpha_1,\beta_1)}$ depends not only on low pass filtered PAN image but on interpolated MS images. Therefore the variance of $\widetilde{MS}_r$ images can also play a role in the final quality of the pan-sharpened image.

In the proposed pansharpening rule given in (4.14) the pansharpened image is dependent on the angle parameters α_1, β_1 of the 2D-DFRFT. These angle parameters are optimized by single objective optimization technique using fitness function involving the quality metrics such as relative dimensionless global error in synthesis (ERGAS), spectral angle mapper (SAM) etc. [31], [34]. In this scheme we have used particle swarm optimization (PSO) technique and ERGAS as quality metric in the fitness function. The ERGAS is a measure of spatial distortion between the reference MS and pansharpened images. It is given by

$$ERGAS = 100\frac{h}{l}\sqrt{\frac{1}{N}\sum_{r}^{N}\left(\frac{RMSE(MS_r, \overline{MS}_{r(\alpha_1,\beta_1)})}{\mu(MS_r)}\right)^2}, \tag{4.16}$$

where $r = 1, ..., N,$, MS_r are the rth reference MS images and $\overline{MS}_{r(\alpha_1,\beta_1)}$ is the pansharpened image obtained using proposed pansharpening rule applied at the degraded scale as per the Wald's protocol [31]. Here h/l is the ratio of resolution of PAN and MS images, $\mu(MS_r)$ is the mean of the rth band, RMSE(A,B) stands for root mean square error between images A and B.

Therefore the task of optimization is to minimize the ERGAS metric to obtain the fused image with minimum spatial distortion. The fitness function f for the optimization problem is

formulated as

$$f = \underset{(\alpha_1,\beta_1)}{\text{minimize}} \left[ERGAS\right], \alpha_1 \neq 0, \beta_1 \neq 0 \tag{4.17}$$

The reason for excluding the values of $\alpha_1 = 0$ and $\beta_1 = 0$ in the fitness function in (4.17) is due to the fact that ERGAS reaches its minimum value of zero if no fusion is done and no additional information will be added to MS images from PAN image. Thus using (4.14) the relevant and additional spatial details available in the P image are injected into the MS image optimized by the α_1, β_1 giving us improved spatial and spectral details in the fused image as compared to the existing fusion techniques.

The steps of the proposed algorithm are summarized as below:

Algorithm 2 2D-DFRFT based pansharpening algorithm-I

1: Obtain up-sampled MS images of the size of PAN image;
2: Compute the intensity image (I) using up-sampled MS images by weighted mean;
3: Obtain histogram matched image (P) using input PAN and intensity image;
4: Compute the image $\hat{P}_{\alpha_1,\beta_1}$ using 2D-DFRFT corresponding to angles α_1 and β_1;
5: Calculate the regression coefficients G_r for use in fusion rule;
6: Obtain the high spatial and spectral resolution MS image using pansharpening rule
$\widehat{MS}_{r(\alpha_1,\beta_1)} = \widetilde{MS}_r + \gamma G_r(P - \hat{P}_{\alpha_1,\beta_1}),\ r = 1, ..., N,$
where $\gamma = 0.9, 1.2$ for IKONOS and GeoEye-1 images respectively.
7: Optimize angle parameters α_1 and β_1 using PSO associated with the 2D-DFRFT for obtaining the minimum spatial distortion using objective function ERGAS.

4.3.1 Simulation Results

The proposed 2D-DFRFT based pansharpening scheme is tested on IKONOS and GeoEye-1 satellites dataset given in Fig.3.4(c)-(d) and Fig.3.4(e)-(f) respectively, are used. To evaluate the pansharpening results, we follow the Wald's protocol [31].

Simulations are also performed to compare the proposed pansharpening scheme with the existing pansharpening schemes based on optimal filter (OMF) [89], adaptive IHS (AIHS) [5], decimated wavelet transform using an additive injection model (Indusion) [118], a trous wavelet

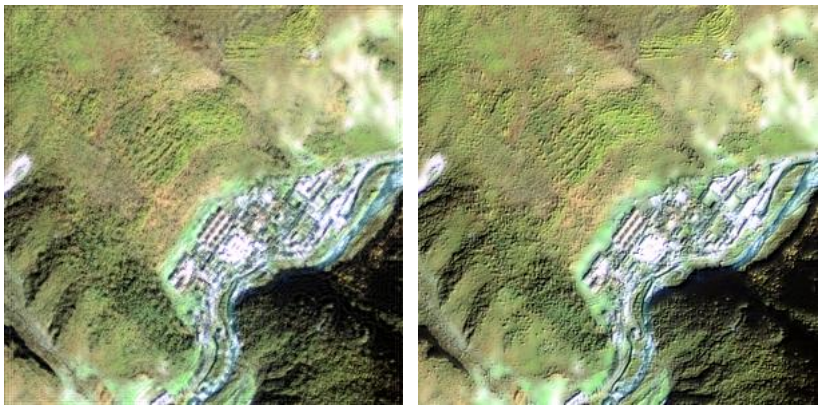

(a)

(b)

(c)

(d)

(e)

(f)

FIGURE 4.4: For IKONOS satellite dataset obtained the pansharpened images using proposed and existing pansharpening schemes are (a) Proposed 2D-DFRFT_F1, (b) OMF, (c) AIHS, (d) indusion, (e) ATWTM2 and (f) MTF-PP schemes.

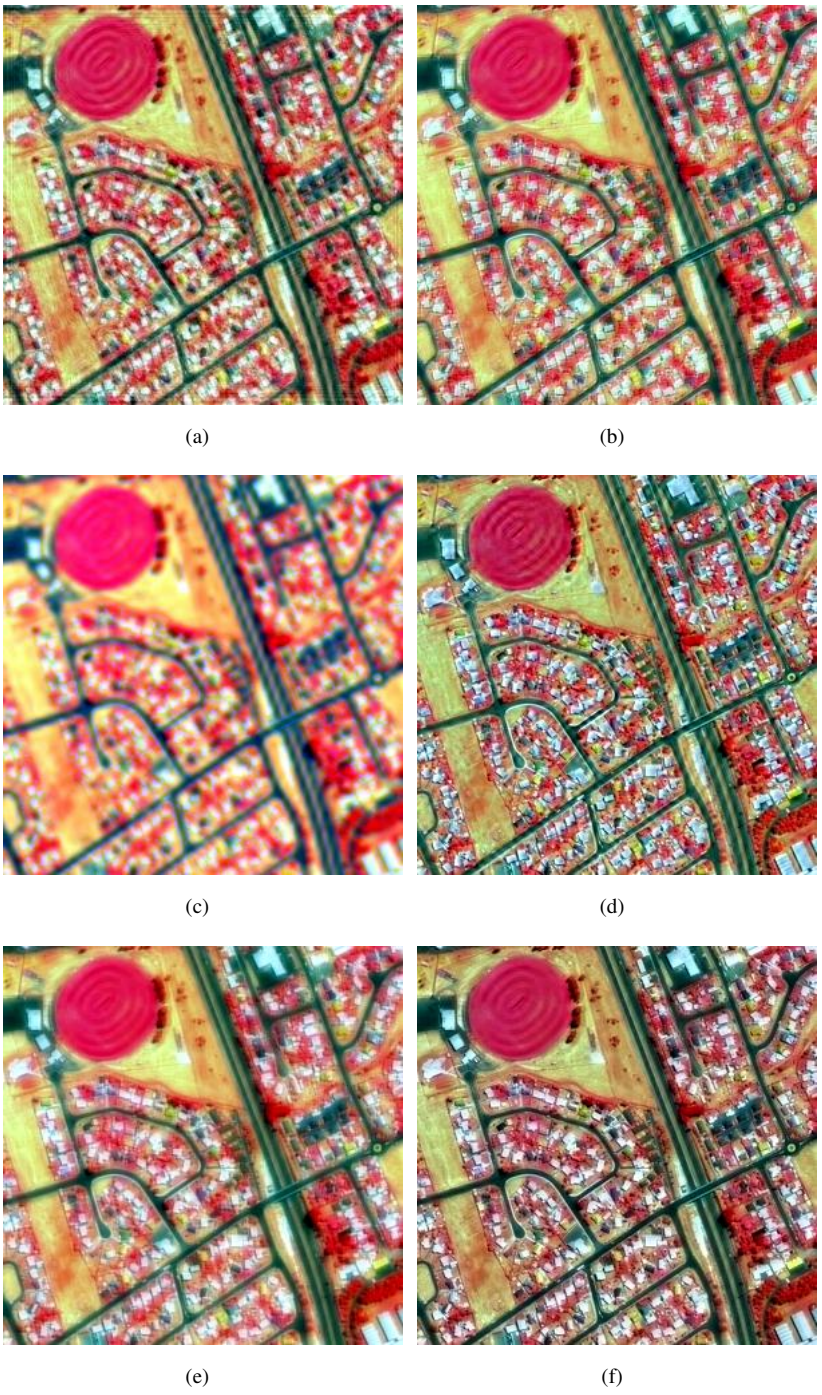

(a) (b)

(c) (d)

(e) (f)

FIGURE 4.5: For GeoEye-1 satellite dataset obtained the pansharpened images using proposed and existing pansharpening schemes are (a) Proposed 2D-DFRFT_F1, (b) OMF, (c) AIHS, (d) indusion, (e) ATWTM2 and (f) MTF-PP schemes.

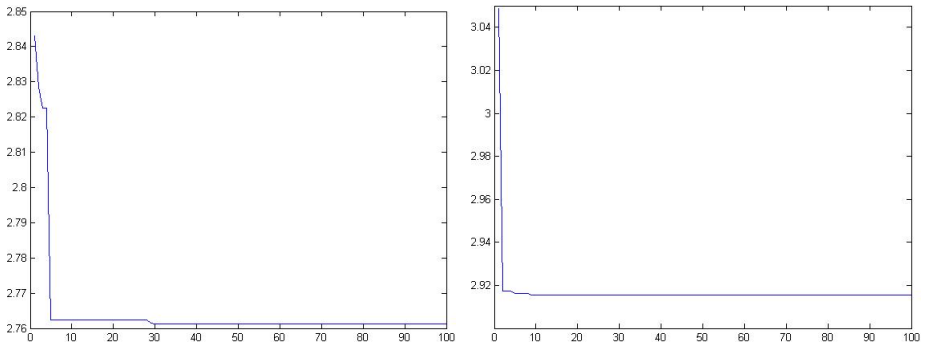

(a) (b)

FIGURE 4.6: Convergence plot (ERGAS versus number of iterations) of PSO in the proposed pansharpening scheme for (a) IKONOS and (b) Geoeye-1 satellite images.

transform using the model-2 (ATWTM2) [50] and generalized Laplacian pyramid with modulation transfer function matched filter and multiplicative injection model (MTF-PP) [115]. The pansharpened image obtained using proposed 2D-DFRFT scheme-I is labeled by 2D-DFRFT_F1.

The angles α_1, β_1 in (4.14) of the proposed method are optimized by single objective PSO algorithm using fitness function involving ERGAS. The details of the parameters chosen for PSO algorithm [136, 140] are given in Table 4.1. These parameters can be selected in different ways discussed in [136, 140, 144, 145]. In the present work we have computed these parameters given in [144] because these parameters provide better balance between the global and local search.

TABLE 4.1: Parameter settings of PSO in the proposed pansharpening algorithm

Parameters	**Value**
Particle numbers/Population	20
Iteration	100
c_1 and c_2	2
Inertia weights	Adaptive [0.9 0.4]

The optimized values of angle parameters (α_1,β_1) obtained using PSO algorithm for IKONOS

and GeoEye-1 satellite images are $(0.0689\pi/2, 0.0710\pi/2)$ and $(0.0851\pi/2, 0.0991\pi/2)$ respectively. To evaluate the convergence of PSO algorithm in the proposed method, the convergence plots (ERGAS versus number of iterations) for IKONOS and GeoEye-1 satellite images are shown in Fig.4.6(a) and Fig.4.6(b) respectively. It can be seen from the Fig.4.6(a) and 4.6(b) that the value of the ERGAS quality metric is almost constant after the twentieth iteration demonstrating its convergence.

The image obtained through the re-sampling of the MS image to the size of the PAN image using interpolation [116] is labeled by EXP image. The proposed method is given in (4.14) using $\gamma = 0.9$ and 1.2 for IKONOS and GeoEye-1 satellite images. The values of parameter γ have been selected experimentally by performing many simulation trials.

The input PAN and EXP images (having four bands red, blue, green and infrared) for IKONOS and GeoEye-1 data set are shown in the Fig.3.4(c),(d) and 3.4(e),(f) respectively. The pansharpened images obtained using the proposed method are shown in Fig.4.4(a) and 4.5(a), respectively. The pansharpened images obtained by the existing methods are shown in Fig.4.4(b)-4.4(f) and Fig.4.5(b)-4.5(f).

TABLE 4.2: The Spectral quality assessment of the fused images for IKONOS dataset at degraded and full scale optimized 2D-DFRFT angle parameters $\alpha_1 = 0.0689\pi/2$ and $\beta_1 = 0.0710\pi/2$.

	Degraded scale			Full scale		
	Q4	**SAM**	**ERGAS**	$\mathbf{D}_\lambda$	$\mathbf{D}_S$	**QNR**
Ref.val.	1	0	0	0	0	1
2D-DFRFT_F1	0.6003	**3.1918**	**2.7637**	0.1789	**0.1734**	**0.6787**
OMF	0.5478	3.3223	3.0877	0.1548	0.2395	0.6427
AIHS	0.5245	4.4030	3.1710	0.2007	0.2094	0.6320
Indusion	0.5573	3.2315	2.9799	0.1728	0.2153	0.6491
ATWTM2	0.5969	3.3004	2.7740	0.1676	0.1906	0.6738
MTF-PP	**0.6287**	3.2490	2.7778	0.2476	0.3524	0.4872

It can be observed from middle portion of the image shown in Fig.4.4(a) that this fused image reveals additional spatial information than the fused images obtained by the existing methods. Similarly spectral quality of the fused image shown in Fig.4.4(a) is better than the simulation

TABLE 4.3: The Spectral quality assessment of the fused images for GeoEye-1 dataset at degraded and full scale optimized 2D-DFRFT angle parameters $\alpha_1 = 0.0851\pi/2$ and $\beta_1 = 0.0991\pi/2$.

	Degraded scale			Full scale		
	Q4	**SAM**	**ERGAS**	**D_λ**	**D_S**	**QNR**
Ref.val.	1	0	0	0	0	1
2D-DFRFT_F1	**0.7515**	**4.0120**	**2.9165**	0.0781	**0.0466**	**0.8789**
OMF	0.6656	4.4149	3.4972	**0.0412**	0.1234	0.8405
AIHS	0.6950	4.6806	3.2969	0.1036	0.0999	0.8069
Indusion	0.6420	4.2838	3.5680	0.0828	0.0954	0.8296
ATWTM2	0.6809	4.6050	3.1848	0.0840	0.1086	0.8165
MTF-PP	0.7234	4.4309	3.1200	0.1953	0.2213	0.6266

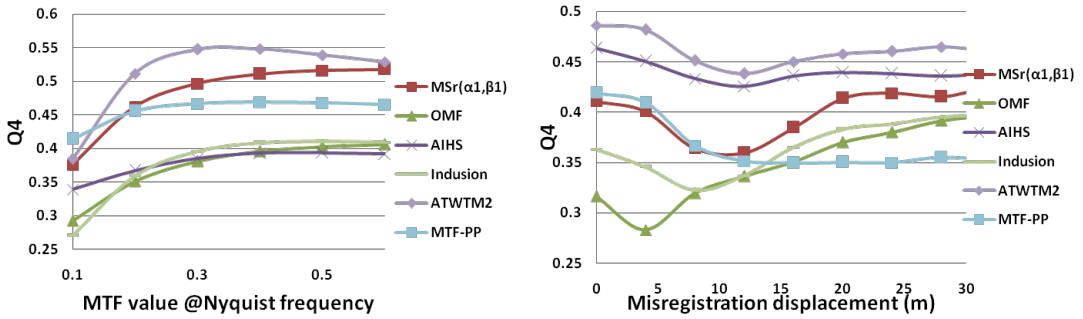

(a) (b)

FIGURE 4.7: Quality/distortion indices for increasing amounts of (a) aliasing, measured by the amplitude at nyquist frequency of the Gaussian-like low-pass filter simulating the modulation transfer functions of the multispectral instrument, (b) misregistration between MS and PAN images using image shown in Fig.4.4.

results obtained by the other existing methods. Similar remarks hold good for the other set of images shown in Fig.4.5 particularly the left corner portion of it.

Using the above pansharpened images shown in Fig.4.4(a) and 4.5(a) the quality metrics Q, SAM, ERGAS for degraded scale assessment and D_λ, D_S, QNR for full scale assessment are computed and the results are tabulated in Table 4.2 and 4.3.

It can be seen from the quantitative results (shown in boldface digits) given in Table 4.2 and 4.3 that the proposed method outperforms the other methods in terms of all the quality metrics

considered in this scheme except D_λ. The proposed method also provides pansharpened image which is better matched in color information of the input MS images with improved spatial details.

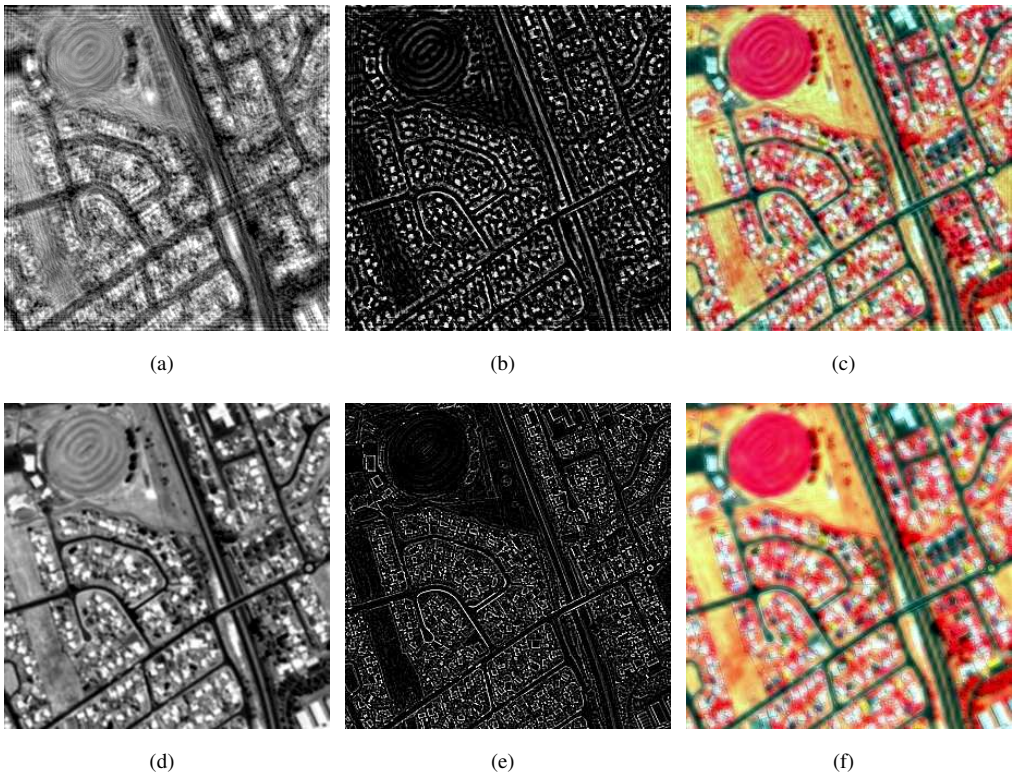

FIGURE 4.8: For GeoEye-1 satellite dataset (a) Filtered PAN (P) image using 2D-DFRFT, (b) Spatial details extracted from PAN (P) image using 2D-DFRFT, (c) Pansharpened image using 2D-DFRFT, (d) filtered PAN image using GLF, (e) Spatial details extracted from PAN image using GLF, (f) Pansharpened image using GLF.

The effects of aliasing and mis-registration on our proposed methods are evaluated for IKONOS data set given in Fig.3.4(c),(d) and the results are compared with existing pansharpening methods as shown in Fig.4.7(a),(b). It can be seen from Fig.4.7(a) that Q4 metric increases with increasing Nyquist frequency initially but becomes almost constant for higher Nyquist frequencies beyond 0.3 Hz. For misregistration errors, it can be observed from Fig.4.7(b), that the parameter Q4 has attained almost a constant value after the displacement error beyond 15m. Thus it is observed that the proposed method provides better results and robustness against

registration error and aliasing effect. This robustness of the proposed technique against mis-registration and aliasing errors may be attributed to the transform domain (fractional domain) filtering involved here.

To compare the 2D-DFRFT in the proposed pansharpening scheme (shown in Fig.4.3) with Gaussian lowpass filter (GLF) and performed the simulation results for GeoEye-1 satellite dataset. The filtered PAN (P) images extracted spatial details from the PAN (P) image and pansharpened images using 2D-DFRFT and GLF are shown in Fig.4.8(a)-4.8(f) respectively. The image shown in Fig.4.8(e) reveals additional spatial and spectral quality than the image obtained by the Fig.4.8(f).

TABLE 4.4: The Spectral quality assessment of the pansharpened images for GeoEye-1 dataset

	Degraded scale			Full scale		
	Q4	**SAM**	**ERGAS**	$\mathbf{D}_\lambda$	$\mathbf{D}_S$	**QNR**
Ref.Val.	1	0	0	0	0	1
2D-DFRFT_F1	**0.7515**	**4.0120**	**2.9165**	0.0781	0.0466	0.8789
GLF	0.7152	4.1467	3.0937	0.0220	**0.0314**	0.9473

The performance metrics Q-index, SAM, ERGAS and QNR for the images shown in Fig.4.8 are computed, and results obtained are tabulated in Tables 4.4. It is seen that the proposed method provides better results in terms of all the quality metrics except QNR.

4.4 Proposed Pansharpening Scheme-II

The images captured from different sensors in remote sensing applications may suffer from spatial and spectral distortion problems [32]. Pansharpening schemes improve the spatial quality and reduce the spectral distortion in the pansharpened image obtained from the MS and PAN images by performing filtering in time domain or joint time-frequency domains [50, 51]. These filtering based pansharpening schemes however assume that the image is band-limited

in conventional Fourier domains. However finite size of the images acquired precludes this assumption to hold true. In addition, the PAN and MS images collected through different sensors satellite environment suffer from different types of noise which may not be stationary in nature. Therefore conventional Fourier transform is not suitable for handling such non-stationary signals and noise [129, 130]. The FRFT is known to handle such non-stationary noise in a more effective way than the conventional Fourier transform [131]. The angle parameter of 2D-

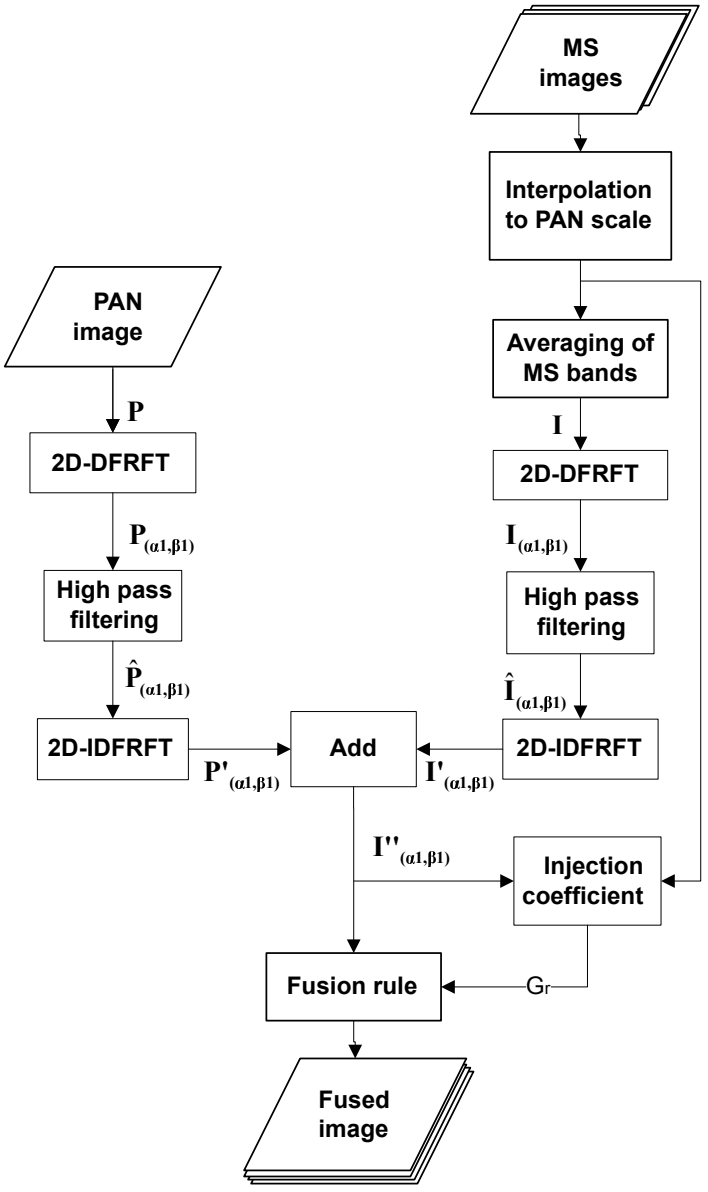

FIGURE 4.9: Block diagram of the proposed panshapening method

DFRFT can be varied to provide infinite representations of the given signal in different DFRFT domains each corresponding to different values of the angle parameter. The DFRFT provides a free degree of freedom in terms of its angle parameters. Therefore it would be interesting to extend the filtering based pansharpening approach to intermediate domains called FRFT domains.

In this section we present a generalization of fast Fourier transform (FFT) based pansharpening scheme proposed in [87]. This method is based on 2D-DFRFT filtering of both the PAN image and intensity image component of the original MS images.

The block diagram of the proposed method is given in Fig.4.9. In this method, low resolution MS input images are up-sampled to the size of PAN image by using interpolation scheme described in [116]. These up-sampled MS images are converted into the intensity image (I) using averaging operation. The intensity image (I) is transformed using 2D-DFRFT defined in (4.7) as given below

$$\hat{I}_{\alpha_1,\beta_1}(m,n) = \sum_{i=0}^{A-1}\sum_{j=0}^{B-1} I(i,j)\mathcal{R}_{\alpha_1,\beta_1}(i,j,m,n), \tag{4.18}$$

where $\hat{I}_{\alpha_1,\beta_1}$ is the 2D-DFRFT domain representation of image I corresponding to angles $\alpha_1 = a_1\pi/2$ and $\beta_1 = b_1\pi/2$.

The image $\hat{I}_{\alpha_1,\beta_1}$ given in (4.18) is filtered by the highpass filter and then the filtered image I_{α_1,β_1} is transformed using the inverse 2D-DFRFT (2D-IDFRFT) given in (4.9) to obtain

$$I'_{\alpha_1,\beta_1}(i,j) = \sum_{m=0}^{A-1}\sum_{n=0}^{B-1} I_{\alpha_1,\beta_1}(m,n)\mathcal{R}_{-\alpha_1,-\beta_1}(m,n,i,j). \tag{4.19}$$

where image I'_{α_1,β_1} is the 2D-IDFRFT domain representation of filtered image I_{α_1,β_1}.

The high resolution PAN image P is transformed using the 2D-DFRFT to obtain $\hat{P}_{\alpha_1,\beta_1}$ given in (4.13). The image $\hat{P}_{\alpha_1,\beta_1}$ is filtered by highpass filter and then the filtered image P_{α_1,β_1} is transformed using the inverse 2D-DFRFT (2D-IDFRFT) defined in (4.9) as given below

$$P'_{\alpha_1,\beta_1}(i,j) = \sum_{m=0}^{A-1}\sum_{n=0}^{B-1} \hat{P}_{\alpha_1,\beta_1}(m,n)\mathcal{R}_{-\alpha_1,-\beta_1}(m,n,i,j), \tag{4.20}$$

where image P'_{α_1,β_1} is the 2D-IDFRFT domain representation of the filtered image P_{α_1,β_1}.

The high frequency filtered P'_{α_1,β_1} image given in (4.20) and I'_{α_1,β_1} image given in (4.19) are added for obtaining the new image I''_{α_1,β_1} as given by

$$I''_{\alpha_1,\beta_1}(i,j) = P'_{\alpha_1,\beta_1}(i,j) + I'_{\alpha_1,\beta_1}(i,j), \tag{4.21}$$

In (4.21), image I''_{α_1,β_1} has spatial information of both the PAN and MS images.

Using image I''_{α_1,β_1}, we propose the following pansharpening rule as

$$\widehat{MS}_{(\alpha_1,\beta_1)r} = \widetilde{MS}_r + \beta\, G_r\, I''_{\alpha_1,\beta_1},\ r = 1,2,...,N, \tag{4.22}$$

where $\widehat{MS}_{(\alpha_1,\beta_1)r}$ is the high spatial and spectral pansharpened image, $\widetilde{MS}_r$ is the rth interpolated MS images in the given total number of N band images, β is the tunning factor obtained by the simulation trials and G_r are the injection coefficients obtained from the regression between each MS band image and image I''_{α_1,β_1} [32]. The injection coefficients are calculated using [66]

$$G_r = \frac{cov(\widetilde{MS}_r, I''_{\alpha_1,\beta_1})}{var(I''_{\alpha_1,\beta_1})}, r = 1,...,N, \tag{4.23}$$

where $var(I''_{\alpha_1,\beta_1})$ is the variance of I''_{α_1,β_1} image and $cov(\widetilde{MS}_r, I''_{\alpha_1,\beta_1})$ indicates the covariance between two images $\widetilde{MS}_r$ and I''_{α_1,β_1}.

Algorithm 3 2D-DFRFT based pansharpening algorithm

1: Obtain up-sampled MS images of the size of PAN image;
2: Obtain the IHS images using up-sampled MS images by RGB to IHS conversion;
3: Compute the image $\hat{I}_{\alpha_1,\beta_1}$ using 2D-DFRFT of I image corresponding to angles α_1, β_1;
4: Compute the image I_{α_1,β_1} using lowpass filtering;
5: Obtain the image I'_{α_1,β_1} using inverse 2D-DFRFT of I_{α_1,β_1} image;
6: Compute the image $\hat{P}_{\alpha_1,\beta_1}$ using 2D-DFRFT of P image corresponding to angles α_1, β_1;
7: Compute the image P_{α_1,β_1} using highpass filtering;
8: Obtain the image P'_{α_1,β_1} using inverse 2D-DFRFT of P_{α_1,β_1} image;
9: Obtain the I''_{α_1,β_1} by adding I'_{α_1,β_1} and P'_{α_1,β_1} images;
10: Calculate the injection coefficients G_r;
11: Obtained the high spatial and spectral pansharpened image $\widehat{MS}_{(\alpha_1,\beta_1)r}$ using pansharpening rule

$$\widehat{MS}_{(\alpha_1,\beta_1)r} = \widetilde{MS}_r + \beta\, G_r\, I''_{\alpha_1,\beta_1},\ r = 1, 2, ..., N,$$

where β is the tunning factor.

4.4.1 Simulation Results

The proposed 2D-DFRFT based pansharpening scheme using the IKONOS and GeoEye-1 satellites is given in Fig.3.4(c),(d) and Fig.3.4(e),(f) respectively. For obtaining the pansharpening results, we follow the Wald's protocol [31].

In the block diagram of the proposed scheme shown in Fig.4.9 using the highpass filters are chosen as first order Butterworth filters with cutoff radius 40 and 350 at degraded and full scale respectively, and the values of the tunning factor β are 2 and 4 for IKONOS and GeoEye-1 satellite images respectively. The selection of cutoff radius and tunning factor β have been done using the simulation trials. The input PAN and EXP images for IKONOS and GeoEye-1 satellite dataset are shown in the Fig.3.4(c),(d) and Fig.3.4(e),(f) respectively. The value of N is four in the MS images; it combines red, blue, green and infrared component images.

Simulation results of the spatial information image I''_{α_1,β_1} given in (4.21) in the proposed scheme using different values of the angle parameters (α_1, β_1) of the 2D-DFRFT for IKONOS satellite dataset are shown in Fig.4.10(a)-(f) and the pansharpened images using different values of

the angle parameters (α_1, β_1) of the 2D-DFRFT are shown in Fig.4.11(a)-(f). It can be seen from the Fig.4.10(c) and 4.11(c) for the values of the angle parameters $\alpha_1 = \beta_1 = 0.98\pi/2$ of the 2D-DFRFT provide the images with maximum spatial information as compared to the other images and Fig.4.10(d) and 4.11(d) for the angle parameters $\alpha_1 = \beta_1 = \pi/2$ of the 2D-DFRFT condition of the conventional Fourier transform provide the images with some spatial distortion. The quality assessment of the pansharpened images of the proposed scheme shown in Fig.4.11(a)-(f) using different values of the angle parameters (α_1, β_1) of the 2D-DFRFT is tabulated in the Table 4.5 in terms of Q4, SAM and ERGAS. It can be observed from the Table 4.5, for the values of the angle parameters $\alpha_1 = \beta_1 = 0.98\pi/2$ of the 2D-DFRFT quality metrics Q4, SAM and ERGAS provide the best results as compared to the other values of the angle parameters.

TABLE 4.5: The quality assessment of the pansharpened images of the proposed scheme using different values of the angle parameters (α_1, β_1) of the 2D-DFRFT for IKONOS satellite dataset.

	Degraded scale		
$(\boldsymbol{\alpha_1, \beta_1})$	**Q4**	**SAM**	**ERGAS**
Ref.val	1	0	0
$\boldsymbol{(0.94\pi/2, 0.94\pi/2)}$	0.5039	4.1241	4.2090
$\boldsymbol{(0.96\pi/2, 0.96\pi/2)}$	0.5975	3.3061	2.8762
$\boldsymbol{(0.98\pi/2, 0.98\pi/2)}$	**0.6448**	**3.0752**	**2.6041**
$\boldsymbol{(\pi/2, \pi/2)}$	0.6300	3.1214	2.7332
$\boldsymbol{(1.02\pi/2, 1.02\pi/2)}$	0.6429	3.0815	2.5920
$\boldsymbol{(1.04\pi/2, 1.04\pi/2)}$	0.5665	3.5869	3.1673

Simulation results are also performed to compare the pansharpened images using proposed pansharpening scheme for the values of the angle parameters $\alpha_1 = \beta_1 = 0.98\pi/2$ of the 2D-DFRFT with the existing pansharpening schemes based on Hilbert vibration decomposition (HVD_F) [122], optimal filter (OMF) [89], adaptive IHS (AIHS) [5], decimated wavelet transform using an additive injection model (Indusion) [118], and a trous wavelet transform using the model-2 (ATWTM2) [50]. The pansharpened images obtained by the scheme-II are labeled by 2D-DFRFT_F2.

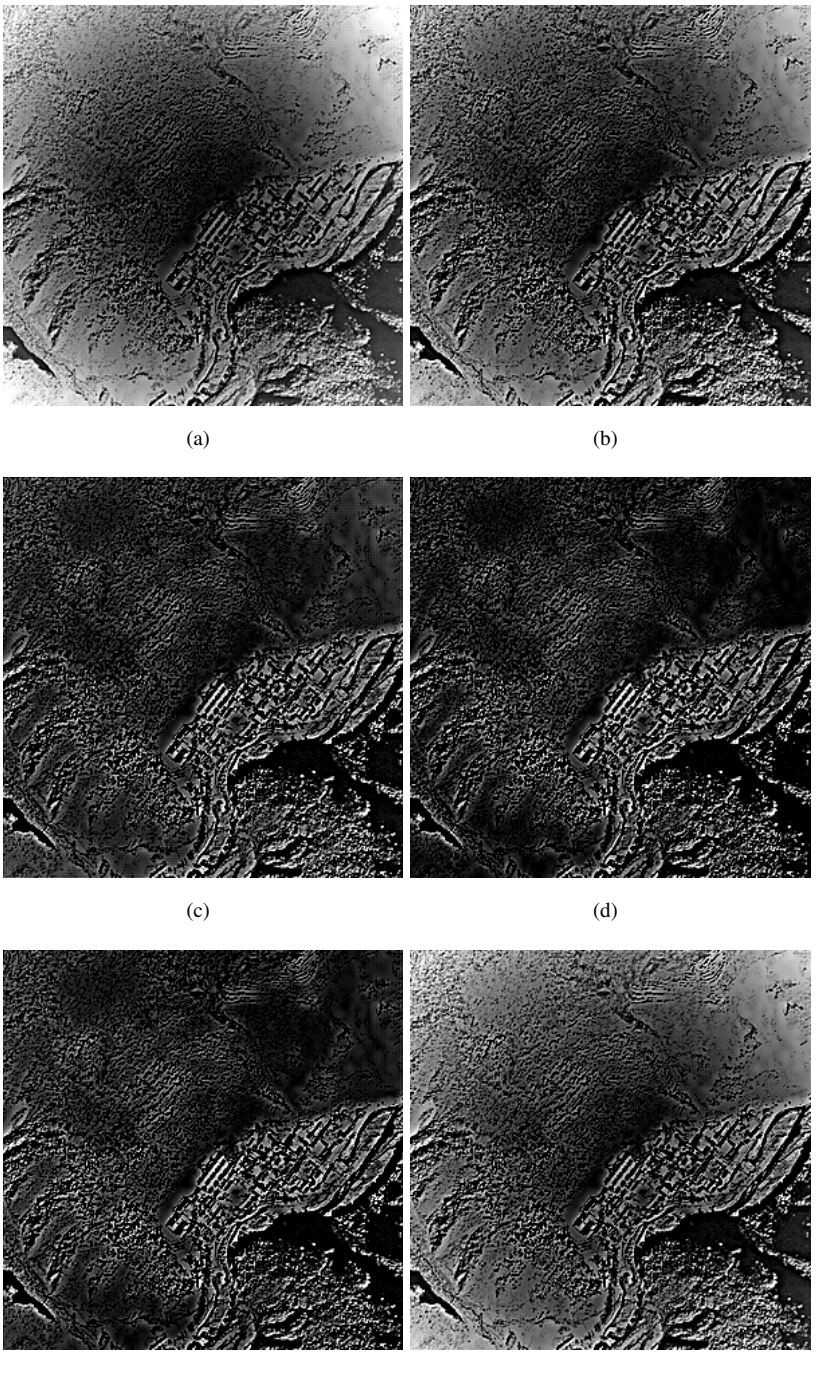

(a) (b)

(c) (d)

(e) (f)

FIGURE 4.10: Spatial information image I''_{α_1,β_1} for IKONOS satellite dataset at different values of angle parameters of the 2D-DFRFT are (a) α_1=β_1=$0.94\pi/2$, (b) α_1=β_1=$0.96\pi/2$, (c) α_1=β_1=$0.98\pi/2$, (d) α_1=β_1=$1\pi/2$, (e) α_1=β_1=$1.02\pi/2$, (f) α_1=β_1=$1.04\pi/2$.

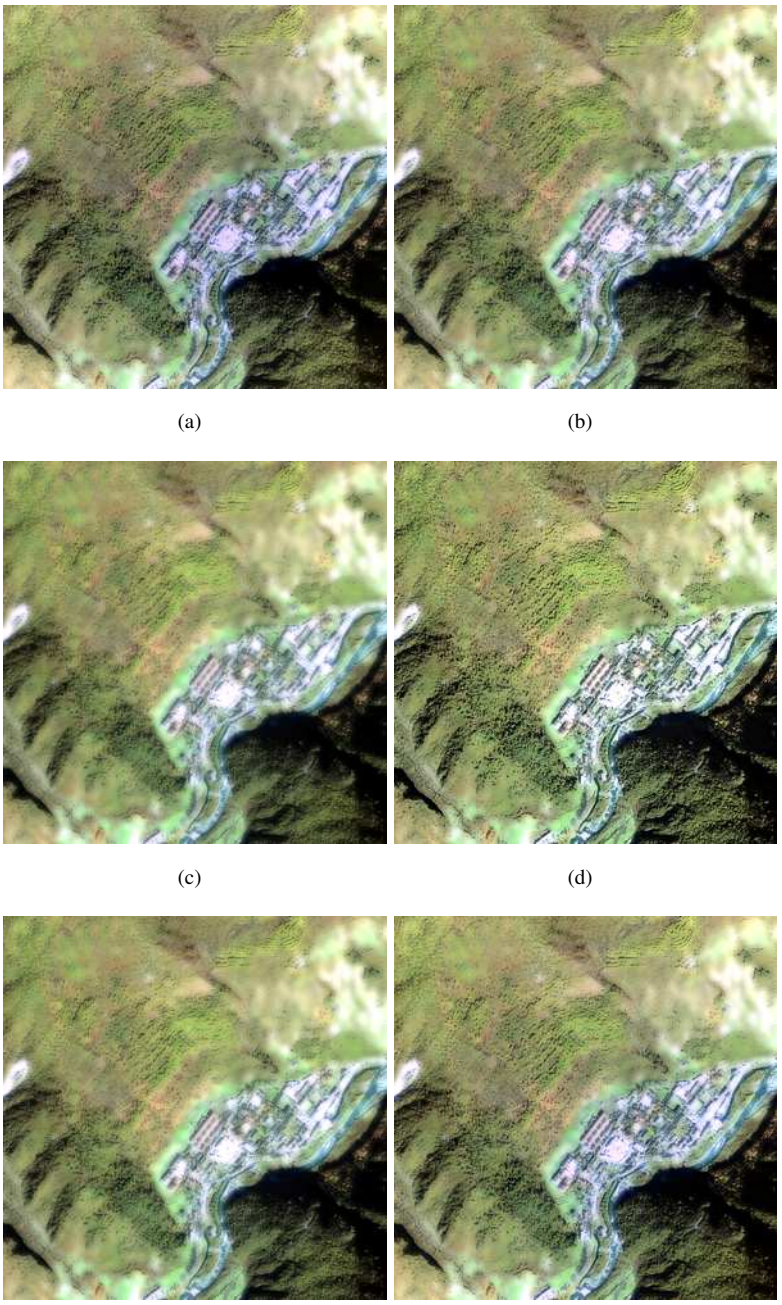

(a) (b)

(c) (d)

(e) (f)

FIGURE 4.11: Pansharpend images of the proposed scheme for IKONOS satellite dataset at different values of angle parameters of the 2D-DFRFT are (a) α_1=β_1=$0.94\pi/2$, (b) α_1=β_1=$0.96\pi/2$, (c) α_1=β_1=$0.98\pi/2$, (d) α_1=β_1=$1\pi/2$, (e) α_1=β_1=$1.02\pi/2$, (f) α_1=β_1=$1.04\pi/2$.

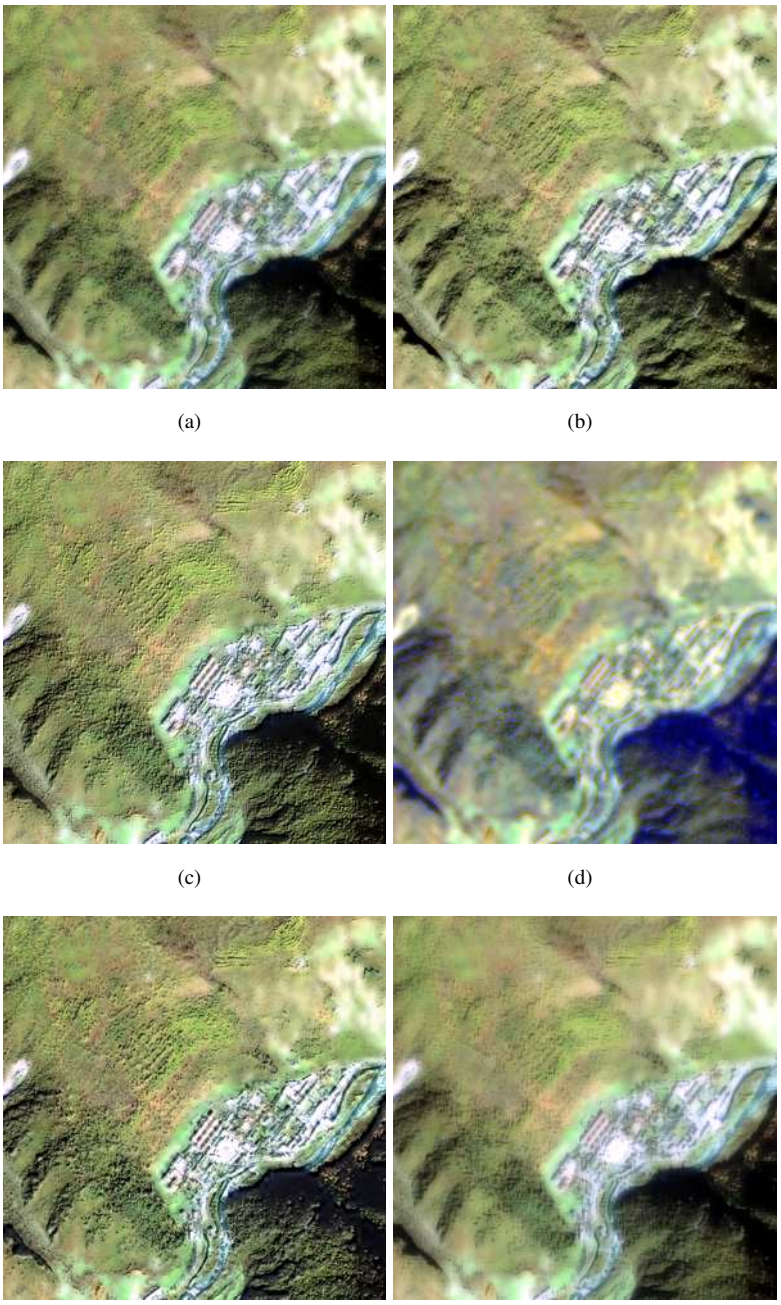

(a) (b)

(c) (d)

(e) (f)

FIGURE 4.12: Pansharpened images using different pansharpening methods for IKONOS satellite dataset are (a) Proposed 2D-DFRFT_F2, (b) HVD_F1, (c) OMF (d) AIHS, (e) Indusion and (f) ATWTM2 methods.

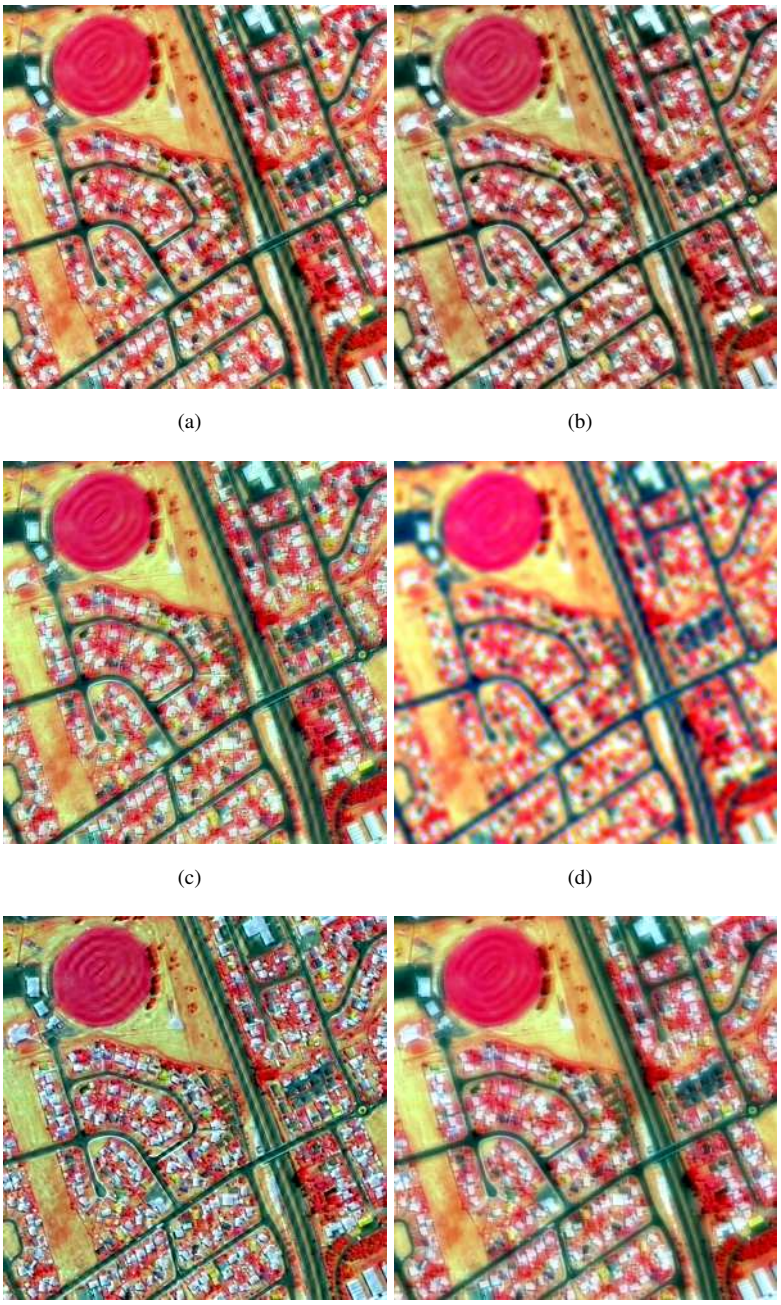

(a) (b)

(c) (d)

(e) (f)

FIGURE 4.13: Pansharpened images using different pansharpening methods for GeoEye-1 satellite dataset are (a) Proposed 2D-DFRFT_F2, (b) HVD_F1, (c) OMF (d) AIHS, (e) Indusion and (f) ATWTM2 methods.

The pansharpened images obtained using the proposed method for value of angle parameters $\alpha_1 = \beta_1 = 0.98\pi/2$ of the 2D-DFRFT and existing methods are shown in Fig.4.12(a)-4.12(f) and Fig.4.13(a)-4.13(f). It can be observed from the middle portion of the image shown in Fig.4.12(a) that this fused image reveals additional spatial information than the fused images obtained by the existing methods. Similarly spectral quality of the fused image shown in Fig.4.12(a) is better than the simulation results obtained by the other existing methods. Similar remarks hold good for the other set of images shown in Fig.4.13, particularly the left corner portion of it. Using the above pansharpened images shown in Fig.4.12(a) and 4.13(a), the quality metrics Q, SAM, ERGAS for degraded scale assessment and D_λ, D_S, QNR for full scale assessment are computed and the results are tabulated in Table 4.6 and 4.7. The best values of the performance measures are highlighted as bold face numerals. It can be seen from the quantitative results given in Table 4.6 for IKONOS dataset that the proposed method outperform the other methods in terms of SAM, ERGAS, D_S and QNR quality metrics while in Q4 and D_λ are comparable in values obtained for other existing methods. Similarly from the results give in Table 4.7 for the GeoEye-1 image dataset, it can be observed that the proposed method outperforms the other methods in terms of Q4, SAM, ERGAS, D_S and QNR quality metrics while the D_λ comparable in value obtained for other existing methods.

TABLE 4.6: The Spectral quality assessment of the pansharpened images for IKONOS dataset at degraded and full scale optimized 2D-DFRFT angle parameters $\alpha_1 = 0.98\pi/2$ and $\beta_1 = 0.98\pi/2$.

	Degraded scale				Full scale		
	Q4	**SAM**	**ERGAS**	**Time(S)**	**D_λ**	**D_S**	**QNR**
Ref.val.	1	0	0	0	0	0	1
2D-DFRFT_F2	0.6448	**3.0752**	**2.6041**	2.28	0.1206	**0.1136**	**0.7795**
HVD_F1	**0.6583**	3.0817	2.6049	5.04	**0.1158**	0.1409	0.7597
OMF	0.5479	3.3195	3.0876	2.02	0.1548	0.2419	0.6407
AIHS	0.5245	4.4030	3.1710	0.61	0.2007	0.2125	0.6295
Indusion	0.5572	3.2295	2.9811	0.16	0.1728	0.2177	0.6472
ATWTM2	0.5968	3.2991	2.7752	1.02	0.1676	0.1930	0.6718

The pansharpening results are obtained using the proposed method for the values of angle parameters (α_1,β_1) of the 2D-DFRFT for IKONOS and GeoEye-1 satellite images and it is observed that pansharpened images of the proposed method for the values $(0.98\pi/2, 0.98\pi/2)$

TABLE 4.7: The Spectral quality assessment of the pansharpened images for GeoEye-1 dataset at degraded and full scale optimized 2D-DFRFT angle parameters $\alpha_1 = 0.98\pi/2$ and $\beta_1 = 0.98\pi/2$.

	Degraded scale				Full scale		
	Q4	**SAM**	**ERGAS**	**Time(S)**	$\mathbf{D}_\lambda$	$\mathbf{D}_S$	**QNR**
Ref.val.	1	0	0	0	0	0	1
2D-DFRFT_F2	**0.7713**	**3.8639**	**2.8078**	1.63	0.0451	**0.0409**	**0.9158**
HVD_F1	0.7682	3.8888	2.8608	5.78	0.0654	0.0976	0.8434
OMF	0.6656	4.4149	3.4972	2.3	**0.0412**	0.1243	0.8396
AIHS	0.5524	4.7684	3.3077	0.63	0.1401	0.1409	0.7388
Indusion	0.6420	4.2838	3.5680	0.17	0.0828	0.0963	0.8288
ATWTM2	0.6810	4.6050	3.1848	1.04	0.0840	0.1094	0.8157

provided the best quality and hare robust against the effect of aliasing and misregistration errors as compared to the existing schemes.

4.5 Proposed Image Fusion Scheme using FRFT

Image fusion is the process of synthesizing two or more images of the same object which comes from different cameras into a new image, and the new image can describe the object more accurately. Image fusion has been widely used in military, remote sensing, robot vision, medical image processing, and other areas. The existing image fusion methods are mainly classified into transform domain and spatial domain methods. In the spatial domain methods, gradient basis [55], principal component analysis [56], singular value decomposition [57], Hilbert vibration decomposition [146], empirical mode decomposition [58] etc. are used in the image fusion. Fusion rules are directly applied into the images on the basis of pixel level and feature level. In the transform domain methods, discrete cosine transform [59], wavelet transform [60], curvelet transform [15] etc. are used for image fusion. Wavelet decomposition is a widespread method used for image fusion [21]. Wavelet decomposition uses basis functions or different filters that are fixed and create influence in the fused image. In [21], the wavelet transforms experience problems when analyzing high frequency content, thus tending to lose spatial information. Along with developing mathematical tools and fusion rules, the image fusion methods are continually being renewed. The fractional Fourier transform (FRFT), which is a generalized version of the conventional Fourier transform. It provides representation in these intermediate domains, and the 2D discrete FRFT (2D-DFRFT) of a signal provides infinite representations of the given signal in different DFRFT domains for corresponding angles, and the DFRFT provides a free degree of freedom in terms of its angle parameters. The 2D-DFRFT has been applied in many image processing applications [39, 40, 41, 42, 43, 44, 45, 46, 47].

This section describes the image fusion technique based on 2D-DFRFT. The additional information obtained through 2D-DFRFT operation is added in the fused image obtain to the conventional fusion rule. The additional degree of freedom in terms of its angle parameters

associated with the 2D-DFRFT is exploited for obtaining better results in the proposed fusion scheme.

The maximum selection rule is one of the commonly used fusion rule in the image fusion applications. In the proposed method, additional information obtained through 2D-DFRFT operation is added in the image obtained through maximum selection fusion rule. The proposed

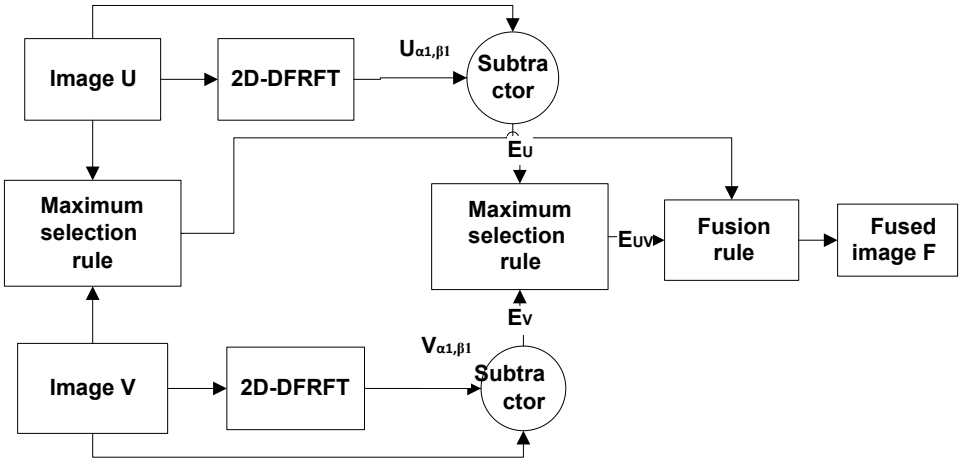

FIGURE 4.14: Block diagram of the proposed fusion scheme

image fusion algorithm is illustrated in Fig.4.14, where source images U and V are transformed using 2D-DFRFT defined in (4.7) as given below

$$U_{\alpha_1,\beta_1}(m,n) = |\sum_{i=0}^{A-1}\sum_{j=0}^{B-1} U(i,j)\mathcal{R}_{\alpha_1,\beta_1}(i,j,m,n)|, \tag{4.24}$$

$$V_{\alpha_1,\beta_1}(m,n) = |\sum_{i=0}^{A-1}\sum_{j=0}^{B-1} V(i,j)\mathcal{R}_{\alpha_1,\beta_1}(i,j,m,n)|, \tag{4.25}$$

where U_{α_1,β_1} and V_{α_1,β_1} are the magnitudes of the 2D-DFRFT domain representation of images U and V corresponding to angles $\alpha_1 = a_1\pi/2$ and $\beta_1 = b_1\pi/2$ respectively.

Then detailed images E_A and E_B are obtained using U_{α_1,β_1} and V_{α_1,β_1} given in (4.24) and (4.25) as given by

$$E_U(m,n) = U(m,n) - U_{\alpha_1,\beta_1}(m,n), \tag{4.26}$$

$$E_V(m,n) = V(m,n) - V_{\alpha_1,\beta_1}(m,n). \tag{4.27}$$

Applying the maximum selection rule on U, V and the obtained UV image as given in (3.18), and maximum selection rule is apply on E_U, E_V images is expressed by

$$E_{UV}(m,n) = \begin{cases} E_U(m,n), & if \;\; E_U(m,n) \geq E_V(m,n), \\ E_V(m,n), & if \;\; E_U(m,n) < E_V(m,n), \end{cases} \tag{4.28}$$

The final fused image in the proposed method is obtained by

$$F(m,n) = UV(m,n) + \alpha \; E_{UV}(m,n), \tag{4.29}$$

where F is the fused image and α is the tunning factor. The image E_{UV} provides most of the edge information of the source images U and V. The extracted detail image E_{UV} given in (4.28) and UV image given in (3.18) are added for obtaining the high detail image F.

4.5.1 Simulation Results

This section performed the Qualitative and quantitative assessment of the proposed method. In this section, simulation results are obtained using five source image pairs (given in section 3.5.1) to compare the proposed scheme with existing fusion schemes such as (i) adaptive sparse representation (ASR) based image fusion scheme [125], (ii) Discrete cosine harmonic wavelet transforms (DCHWT) based image fusion scheme [29] and (iii) cross bilateral filter (CBF) based image fusion [28].

Simulations are carried out for different values of angle parameters (α_1,β_1) of the 2D-DFRFT and it is observed that the values $(0.88\pi/2, 0.88\pi/2)$ provide better quality of the fusion results. In the proposed fusion rule given in (4.29), the value of tunning factor α is taken as 0.02 which is selected through multiple simulation trials.

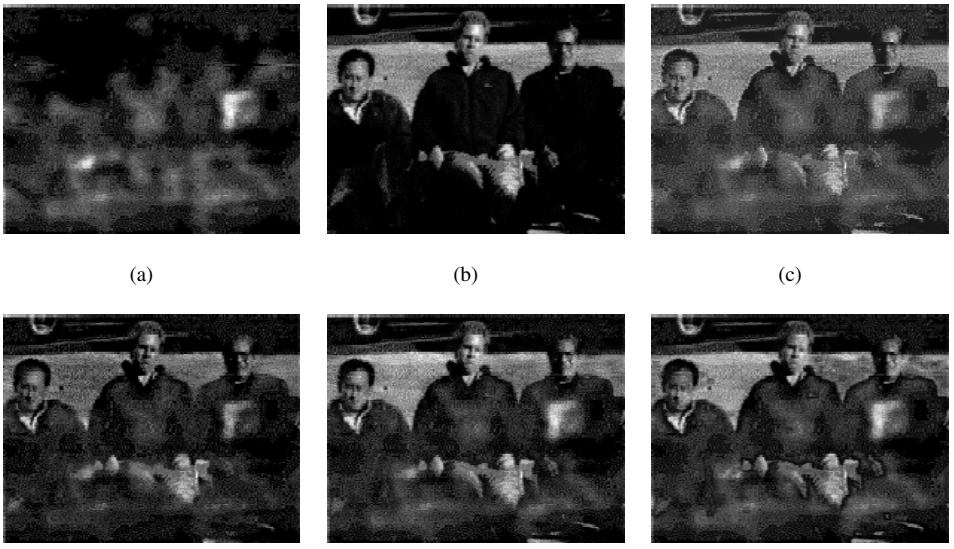

(a) (b) (c)

(d) (e) (f)

FIGURE 4.15: (a) MMW and (b) visible source images, fused image obtained by the (c) Proposed 2D-DFRFT, (d) ASR, (e) DCHWT and (f) CBF based schemes

In the first experiment, fusion is performed on multi-sensor image pairs.

- The MMW and visible source images are shown in Figs. 4.15(a) and 4.15(b). Figs. 4.15(c) shows the fused image obtained using the proposed method, and Figs. 4.15(d),(e),(f) show fused images using existing schemes given in [28, 29, 125].
- The IR and visible source images are shown in Figs. 4.16(a) and 4.16(b). Figs. 4.16(c) shows the fused image obtained using the proposed method, and Figs. 4.16(d), (e), (f) show fused images using existing schemes given in [28, 29, 125].

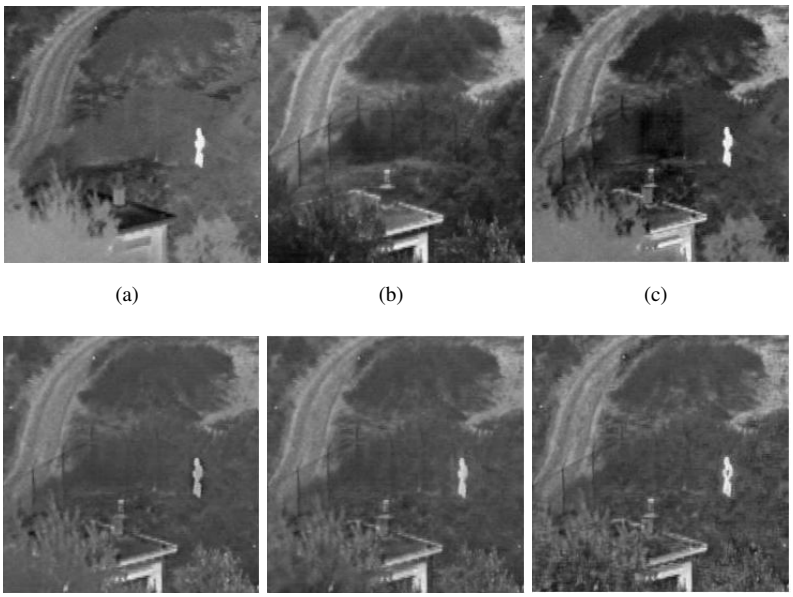

(a) (b) (c)

(d) (e) (f)

FIGURE 4.16: (a) IR and (b) visible source images, fused image obtained by the (c) Proposed 2D-DFRFT, (d) ASR, (e) DCHWT and (f) CBF based schemes

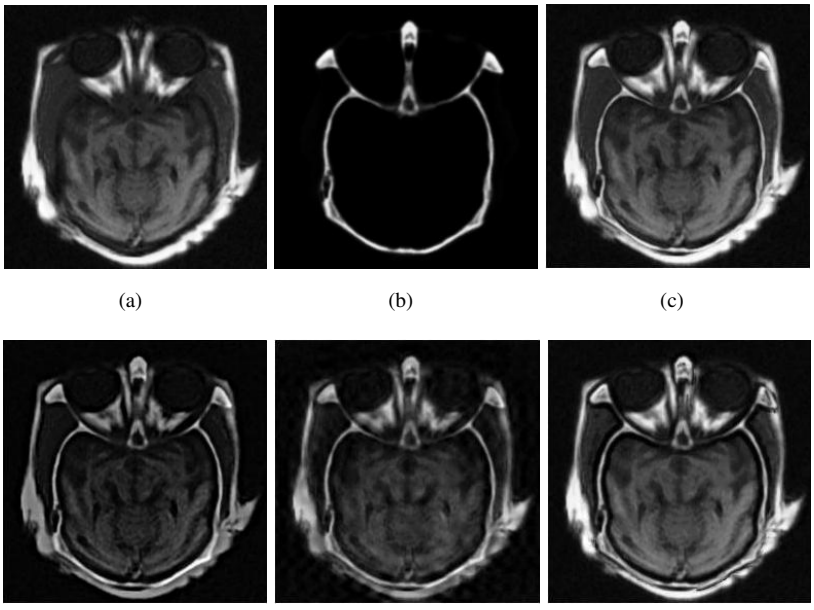

(a) (b) (c)

(d) (e) (f)

FIGURE 4.17: (a) MRI and (b) CT source images, fused image obtained by the (c) Proposed 2D-DFRFT, (d) ASR, (e) DCHWT and (f) CBF based schemes

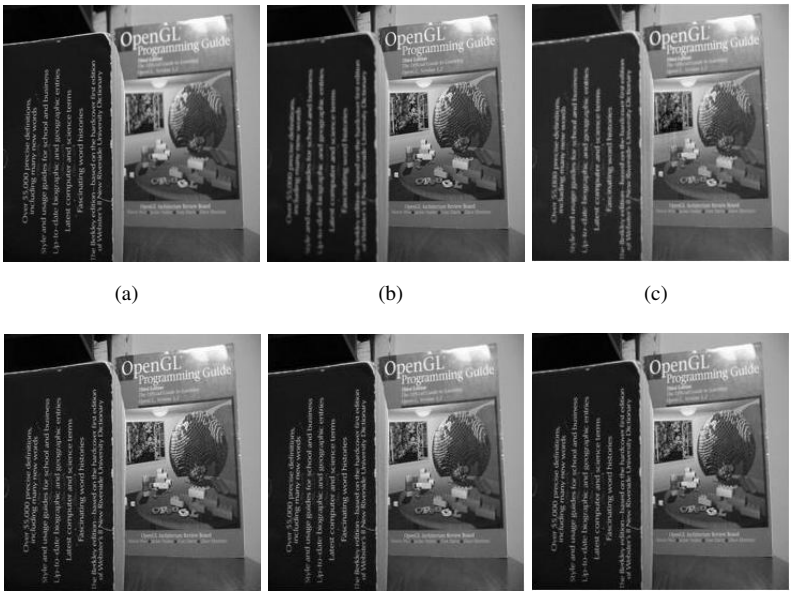

(a) (b) (c)

(d) (e) (f)

FIGURE 4.18: (a) and (b) Multi-focus Book source images, fused image obtained by the (c) Proposed 2D-DFRFT, (d) ASR, (e) DCHWT and (f) CBF based schemes

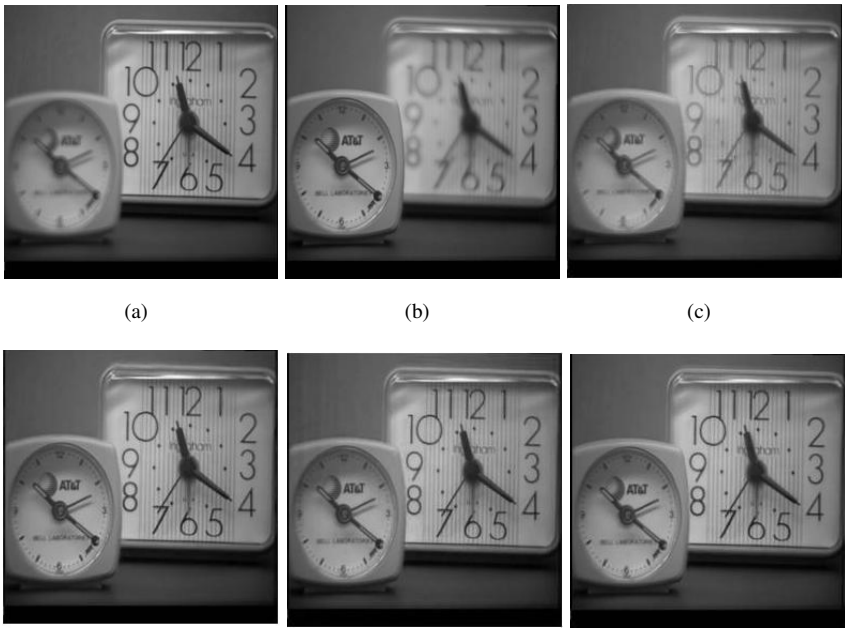

(a) (b) (c)

(d) (e) (f)

FIGURE 4.19: (a) and (b) Multi-focus Clock source images, fused image obtained by the (c) Proposed 2D-DFRFT, (d) ASR, (e) DCHWT and (f) CBF based schemes

- The MRI and CT medical images are shown in Figs. 4.17(a), 4.17(b). Figs. 4.17(c) show the fused images obtained using the proposed method and fusion results of existing schemes given in [28, 29, 125] are shown in Figs. 4.17(d), 4.17(e), 4.17(f) respectively.

By observing these figures it is clear that the images obtained using the proposed fusion technique are better in visual appearance than the images obtained using the existing techniques.

In the second experiment, the fusion is performed on multi-focus Book and Clock source image pairs.

TABLE 4.8: Performance comparison of fused images

	API	SD	AG	H	MI	FS	CC	SF
MMW and visible source images								
2D-DFRFT	**7.189**	**6.0515**	**3.0547**	**4.2717**	**3.8951**	1.905	0.6759	**3.869**
ASR	4.183	3.953	2.6103	3.6018	1.6531	1.9122	**0.7009**	3.2981
CBF	6.305	5.4303	2.916	4.1355	2.352	1.8994	0.6659	3.7107
DCHWT	5.4467	4.9544	2.7494	3.9545	1.7975	**1.9702**	0.6767	3.4529
IR and visible source images								
2D-DFRFT	**113.8201**	**30.5919**	7.2281	**6.76**	**5.8549**	**1.9571**	0.771	9.8446
ASR	90.7209	24.096	6.4558	6.3054	1.7018	1.8968	**0.7968**	9.1921
CBF	89.673	27.0939	**8.6559**	6.4852	1.6967	1.8342	0.7532	**11.3652**
DCHWT	90.1042	24.696	6.7305	6.2967	1.6022	1.8344	0.7701	9.0485
MRI and CT source images								
2D-DFRFT	**58.8409**	**60.4562**	9.9293	6.1919	**5.7489**	1.6333	0.6747	17.567
ASR	31.4959	39.1903	8.3337	6.1865	2.7663	1.6602	**0.6919**	14.6749
CBF	52.875	55.5312	**12.8419**	**6.7777**	5.3686	1.6227	0.6592	**22.0091**
DCHWT	38.0233	41.9861	8.0346	6.5888	1.9772	**1.7133**	0.6845	13.3888
Book source images								
2D-DFRFT	**86.9253**	**59.9457**	14.4993	**7.3769**	**9.2547**	1.9831	0.9899	23.5665
ASR	83.1806	59.3426	**16.7913**	7.3419	8.4621	1.9904	0.9893	**29.2452**
CBF	82.8529	58.9722	15.3524	7.3034	8.2881	**1.9922**	**0.9906**	26.0827
DCHWT	83.0109	59.1883	16.0855	7.3315	8.1143	1.9841	0.9901	27.7148
Clock source images								
2D-DFRFT	**102.4419**	**50.549**	6.8458	7.2874	**8.9195**	**1.9749**	0.9876	10.4878
ASR	96.9211	50.5028	9.0741	7.321	7.511	1.9579	0.9879	15.4741
CBF	96.5074	50.1742	**10.4601**	7.31	8.015	1.9622	0.9882	**16.8638**
DCHWT	96.6567	50.2248	8.8556	**7.3868**	7.0283	1.9693	**0.9888**	14.6276

- The multi-focus Book and Clock images are shown in Figs. 4.18(a), 4.18(b) and 4.19(a), 4.19(b). Figs. 4.18(c) and 4.19(c) shows the fused images obtained using the proposed

TABLE 4.9: Performance comparison of fused images

	$Q^{UV/F}$	$L^{UV/F}$	$N^{UV/F1}$	ans
MMW and visible source images				
2D-DFRFT	0.9011	0.0981	0.0416	1
ASR	0.7907	0.2092	**0.0109**	1
CBF	**0.9369**	**0.0619**	0.0328	1
DCHWT	0.9241	0.0756	0.0141	1
IR and visible source images				
2D-DFRFT	0.6731	0.3002	0.1922	1
ASR	**0.7345**	0.2621	**0.0166**	1
CBF	0.7223	**0.2312**	0.1371	1
DCHWT	0.7335	0.2612	0.0189	1
MRI and CT source images				
2D-DFRFT	0.8663	0.1211	0.5511	1
ASR	0.8555	0.1426	**0.0286**	1
CBF	**0.8816**	**0.1082**	0.1004	1
DCHWT	0.8145	0.182	0.0297	1
Book source images				
2D-DFRFT	0.9813	**0.0154**	0.0152	1
ASR	0.9704	0.0276	0.0077	1
CBF	**0.982**	0.018	3.78E-05	1
DCHWT	0.978	0.0212	0.0024	1
Clock source images				
2D-DFRFT	0.7324	0.2646	0.0188	1
ASR	0.9137	0.0833	0.022	1
CBF	0.9257	0.0742	5.67E-04	1
DCHWT	0.9102	0.0881	0.0091	1

method and fusion results of existing schemes given in [28, 29, 125] are shown in Figs. 4.18(d), 4.18(e), 4.18(f) and Figs. 4.19(d), 4.19(e), 4.19(f).

By observing Fig.4.18 and Fig.4.19, it is clear that the fused images obtained using the proposed method are comparable to the images obtained using the existing techniques.

From Figs. 4.15- Fig.4.19, it is clear that in the proposed scheme edges of the fused image are very clear and sharp as compared to the existing methods. In the proposed fusion scheme, it combines the edge information present in the high frequency component to the source images and resulting fused images have better spatial quality as compared to the existing methods.

Table 4.8 and 4.9 shows the performance of the fusion on multi-sensor and multi-focus image pairs. The performance of the existing and proposed fusion methods are compared with the

objective fidelity criterion measures such as API, SD, AG, H, MI, FS, CC, SF, $Q^{AB/F}$, $L^{AB/F}$ and $N^{AB/F}$. It is well known that for better fusion performance values of the API, SD, AG, H, MI, SF, $Q^{AB/F}$ should have higher value and $L^{AB/F}$, $N^{AB/F}$ should have lower value. In Tables 4.8 and 4.9 the best value of the performance measures are highlighted as bold face numerals. It can be observed from Tables 4.8 and 4.9 that the performance metrics API, SD, AG, H, MI, FS, CC, SF, $Q^{AB/F}$ measures are highest values and $L^{UV/F}$, $N^{AB/F}$ are lowest values for the proposed scheme in both of the experiments conducted. The comparative analyses show that the visual quality of the fused images are improved in the proposed method as compared to the existing methods.

4.6 Conclusions

In this chapter, two 2D-DFRFT based pansharpening and one image fusion schemes are proposed. In the proposed pansharpening scheme-I, the additional degree of freedom in terms of its angle parameters associated with the 2D-DFRFT is optimized by single objective particle swarm optimization (PSO) algorithm for obtaining the best results in the proposed pansharpening scheme. The optimized values of angle parameters (α_1,β_1) obtained using PSO algorithm for IKONOS and GeoEye-1 satellite images are $(0.0689\pi/2, 0.0710\pi/2)$ and $(0.0851\pi/2, 0.0991\pi/2)$ respectively. In scheme-II, pansharpening results obtained using the proposed method for the values of angle parameters (α_1,β_1) of the 2D-DFRFT for IKONOS and GeoEye-1 satellite images and it is observed that pansharpened images of the proposed method for the values $(0.98\pi/2, 0.98\pi/2)$ provide the best quality.

The qualitative and quantitative analysis of the presented simulation results shows that the proposed technique provides improved spectral and spatial quality fused image as compared to some of the existing pansharpening techniques for the IKONOS and GeoEye-1 satellite images. The effects of aliasing and mis-registration errors on our proposed methods are also investigated and compared with other existing pansharpening methods. It is also seen that the

proposed methods are robust against aliasing and mis-registration errors. In the proposed image fusion scheme, additional information obtained through 2D-DFRFT operation is added in the image obtained through maximum selection fusion rule. Simulation results are carried out for different values of angle parameters (α_1,β_1) of the 2D-DFRFT and it is observed that the values $(0.88\pi/2, 0.88\pi/2)$ provide better quality of the fusion results. The qualitative and quantitative analysis of the presented simulation results shows that the proposed technique provides improved spatial quality fused image as compared to some of the existing fusion techniques.

Chapter 5

Graph Signal Processing Based Image Fusion/Pansharpening Schemes

In this chapter, the recently developed Graph signal processing (GSP)/spectral graph wavelet filterbank (SGWF) based image fusion/pansharpening schemes are presented. The graph representations of the regular signals have been shown to be promising in practice recently [48]. Digital images can also be interpreted as graphs where every pixel in the image with its neighboring pixels (nodes) and by interpreting pixel values as the values of the graph-signal at each node. The advantage of this interpretation of images as graphs is in terms of the flexibility of linking pixels in arbitrary ways, leading to different filtering/downsampling patterns [48]. Recently, two-channel graph filterbank has been introduced [147] and has shown improved performance in different applications [49, 148, 149]. The structure of this chapter is as follows: In section 5.1, introduction and a brief literature review is presented; in Section 5.2, the details of the SGWF method are explained; Section 5.3 provides details of the proposed pansharpening scheme and simulation results which gives a comparative analysis of proposed scheme with existing schemes; Section 5.4 describes the proposed image fusion method with simulation results which gives a comparative analysis of the proposed scheme with existing

schemes. Section 5.5 provides the comparison between proposed pansharpening and image fusion techniques, Conclusions are drawn in Section 5.6.

5.1 Introduction

Remote sensing satellite sensors collect imagery with different spatial and spectral resolutions in multispectral (MS) and panchromatic (PAN) images. The PAN image has low spectral and high spatial resolution, while the MS images have low spatial and high spectral resolution [123]. The MS sensors with high spatial resolution are limited by technical constraints of the remote sensing satellite system [127]. Due to these constraints the high spatial resolution MS images are obtained by the pansharpening method, which combines information in MS images with information derived from higher spatial resolution PAN image [67]. One of the pansharpening scheme is based on multiresolution analysis (MRA). The multiresolution-analysis (MRA) based methods employ spatial filters to extract the high frequency information from the PAN image [150]. This high frequency information is added into the upscaled MS images, possibly weighted using a suitable injection model [151]. Wavelet transform (WT) [6], high pass filtering (HPF) [152], generalized Laplacian pyramid (GLP) [84], etc. are examples of MRA based pansharpening schemes. The undecimated wavelet decompositions and Laplacian pyramids, have proven to the effective in implementing fusion at different resolutions [71, 84].

In this chapter, a new pansharpening scheme using two-channel graph filterbank is proposed. The highpass component in the graph filterbank can be used for adding the spatial information from PAN image to MS images for pansharpening purpose. Simulations are carried out using MATLAB on IKONOS and GeoEye-1 satellite datasets. The results using different types of two-channel graph filterbank in the proposed method are compared with the existing pansharpening schemes based on decimated wavelet transform using an additive injection model (Indusion) [118] and additive wavelet luminance proportional (AWLP) [6], a-trous wavelet transform using the model 2 (ATWTM2) [50]. In the proposed pansharpening method, we have

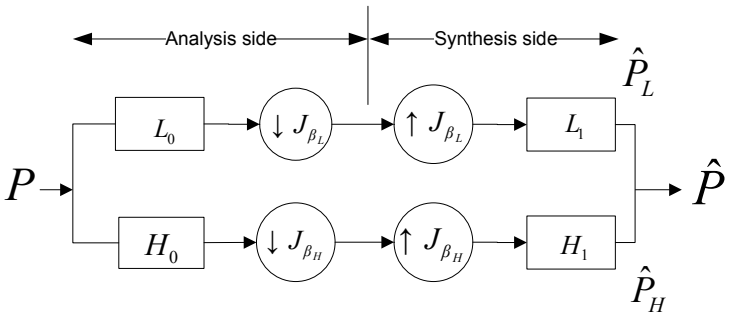

FIGURE 5.1: Critically sampled two-channel graph filterbank.

investigated the effect of aliasing and misregistration errors and compared it with other existing pansharpening methods using the methodology discussed in [143].

5.2 Review of SGWF

Graphs are mathematical structures representing a set of objects related to each other. The objects are represented by vertices or nodes and the relations are encoded by edges interconnecting the nodes [147]. The objects and the interconnections vary depending on the application of interest. To be explicit, a graph G of size N, is an ordered pair $(\mathcal{V}, E)$, where $\mathcal{V}$ is the set of N vertices of the graph indexed from 0 to $(N-1)$ and E is the set of all edges in the graph [147].

Digital images have also been interpreted as graph signals where every pixel is considered a node and the pixel value as the value of the graph signal at the corresponding node [147]. The advantage of this interpretation of images as graphs is in terms of the flexibility of linking pixels in arbitrary ways, leading to different filtering/downsampling patterns [48] with improved results in different applications. A two-channel wavelet filterbank on a graph provides a decomposition of any graph signal into a lowpass and a highpass graph signal component [147]. The two channels of the filterbank are characterized by the graph filters $\{L_i, H_i\}_{i\epsilon\{0,1\}}$ and the downsampling operations J_{β_H} and J_{β_L} [48] as shown in Fig.5.1. The L_0 and H_0 act as a lowpass and highpass filters respectively. The filtering operations in each channel are followed by

downsampling operations J_{β_H} and J_{β_L} described in detail in [147]. The output signals in the lowpass and highpass channels, after reconstruction are expressed as [147]

$$\hat{P}_L = \frac{1}{2} L_1 (I + J_{\beta_L}) L_0 P, \tag{5.1}$$

$$\hat{P}_H = \frac{1}{2} H_1 (I + J_{\beta_H}) H_0 P \tag{5.2}$$

respectively. To describe the operation of two-channel filterbank as shown in Fig.5.1, let us denote the entire operation in (5.1) as an operator $O_L^2(.)$ operating on input signal P for the sake of brevity. Therefore (5.1) can be written as

$$\hat{P}_L = O_L^2(P). \tag{5.3}$$

The overall output $\hat{P}$ of the filterbank is the sum of outputs of the two channels, i.e., $\hat{P} = \hat{P}_L + \hat{P}_H = TP$, where T is the overall transfer function of the filterbank given by [48]:

$$T = \frac{1}{2} L_1 (I + J_{\beta_L}) L_0 + \frac{1}{2} H_1 (I + J_{\beta_H}) H_0, = \frac{1}{2} (L_0 L_1 + H_0 H_1) + \frac{1}{2} (L_1 J_{\beta_L} L_0 + H_1 J_{\beta_H} H_0). \tag{5.4}$$

In (5.4), the spectral folding term $(L_1 J_{\beta_L} L_0 + H_1 J_{\beta_H} H_0)$ arising from downsampling and upsampling must be zero. In addition, $T = I_N$ should be satisfied for perfect reconstruction, where I_N is an $N \times N$ identity matrix.

The decomposition scheme shown in Fig.5.1 has also been extended for M-channels and multiscale decomposition [153].

5.3 Spectral Graph Wavelet Filterbank Based Proposed Pansharpening Algorithm

The aim of the pansharpening scheme for remote sensing images is to generate the pansharpened MS images with high spatial and spectral resolution. Some pansharpening schemes achieve this by adding the spatial information from the PAN image into the MS images. The spatial information of the PAN image is extracted by some filtering technique using Fourier transform, wavelet transform etc. In the present pansharpening scheme we propose the use of SGWF for extracting the information from the PAN image. In the proposed method the lowpass signal generated from multistage multichannel of SGWF decomposition will be used to add additional information in the MS images using appropriate pansharpening rule. The block diagram of the proposed pansharpening method is given in Fig.5.2. Here the input MS images are up-sampled and interpolated to the size of PAN image by using scheme described in [116].

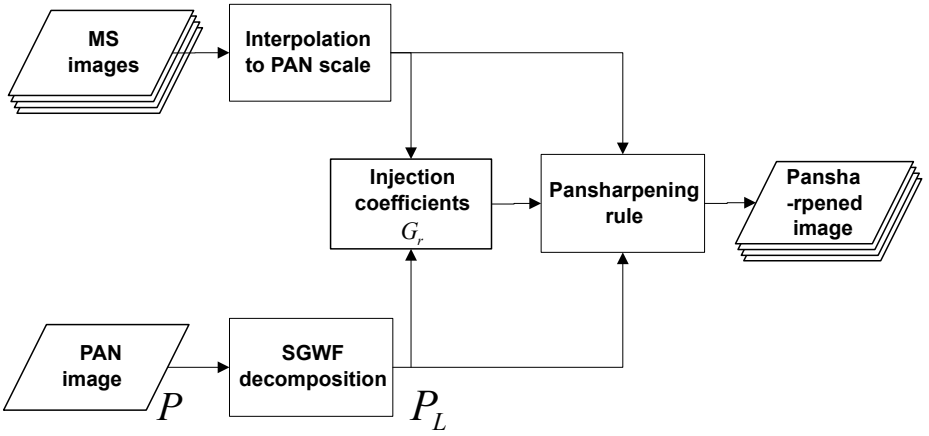

FIGURE 5.2: Block diagram of the proposed panshapening method

The interpolated PAN image P is decomposed by the SGWF (as shown in Fig.5.2). The details of the SGWF decomposition block is given in Fig.5.3. Here, an M_k-channel SGWF decomposition operator similar to the operator appearing in (5.3), giving us lowpass component of the input signal is denoted as $O_L^{M_k}(.)$. The relationship between output lowpass component and

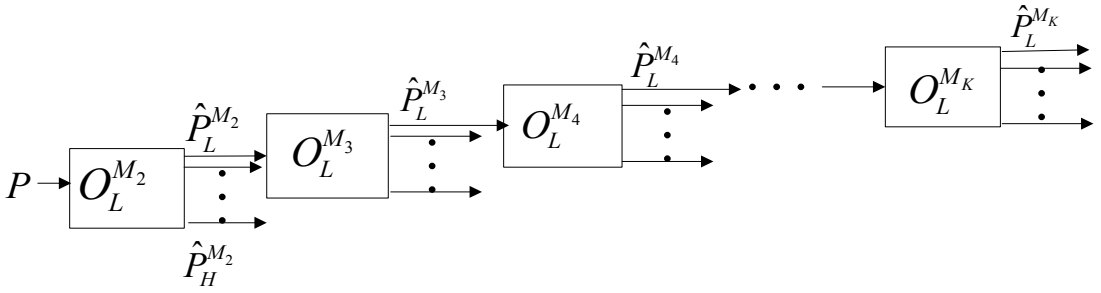

FIGURE 5.3: SGWF decomposition

input signal at kth stage of decomposition in Fig.5.3, therefore, can be written as

$$\hat{P}_L^{M_{k+1}} = O_L^{M_{k+1}}(\hat{P}_L^{M_k}), \tag{5.5}$$

where $k = 1, 2, ..., K-1$ and $K-1$ are the total stages in the SGWF decomposition and M_{k+1} denotes the number of channels at kth stage in the SGWF decomposition. Therefore, for the first stage in the decomposition $P = \hat{P}_L^{M_1}$.

The output image P_L after the SGWF decomposition block in Fig.5.2 is obtained using

$$P_L = \sum_{k=1}^{K-1} \alpha_k \hat{P}_L^{M_{k+1}}, \tag{5.6}$$

where α_k are the weighting coefficients. The coefficients α_k are obtained by optimizing single objective optimization technique using fitness function involving the quality metrics such as relative dimensionless global error in synthesis (ERGAS), spectral angle mapper (SAM) etc. [31], [34]. In this scheme we have used ERGAS as quality metric in the fitness function. Therefore the task of optimization is to minimize the ERGAS metric to obtain the pansharpened image with minimum spatial distortion. The fitness function f for the optimization problem is formulated as

$$f = \underset{(\alpha_k)}{\text{minimize}} \left[ERGAS\right], k = 1, 2, ..., K-1 \tag{5.7}$$

The ERGAS in (5.7) is a measure of spatial distortion between the reference MS and pansharpened images (obtained by applying Wald's protocol at degraded scale) and is given by [31]

$$ERGAS = 100\frac{h}{l}\sqrt{\frac{1}{n}\sum_{r}^{n}\left(\frac{RMSE(MS_r, \overline{MS}_r)}{\mu(MS_r)}\right)^2}, \tag{5.8}$$

where $r = 1, 2, ..., n,$. Here h/l is the ratio of resolution of PAN and MS images, MS_r are the rth reference MS images and n denotes the total number of band images (the value of n is usually four to combine red, blue, green and infrared component images), $\mu(MS_r)$ is the mean of the rth band image, $RMSE(A, B)$ stands for root mean square error between images A and B, and $\overline{MS}_r$ is the pansharpened image obtained using proposed pansharpening rule applied at the degraded scale as per the Wald's protocol [31]. It is assumed that the weighting coefficients α_k obtained at degraded scale using Wald's protocol will continue to be same for the full scale proposed pansharpening rule given below.

Using (5.6), we propose the following pansharpening rule as

$$\widehat{MS}_r = \widetilde{MS}_r + \gamma\, G_r\, (P - P_L), r = 1, 2, ..., n, \tag{5.9}$$

where $\widehat{MS}_r$ is the pansharpened image, γ is the tunning factor obtained through simulation trials, $\widetilde{MS}_r$ are the rth interpolated MS images at the scale of the PAN image and G_r are the injection coefficients obtained from the regression between each MS images and image P_L [32]. The injection coefficients G_r are calculated using [66]

$$G_r = \frac{cov(\widetilde{MS}_r, P_L)}{var(P_L)}, r = 1, ..., n, \tag{5.10}$$

where $var(P_L)$ is the variance of image P_L and $cov(\widetilde{MS}_r, P_L)$ indicates the covariance between two images $\widetilde{MS}_r$ and P_L.

Thus the relevant and additional spatial details extracted from the P image is injected into

the MS images by SGWF, giving us improved spatial and spectral details in the pansharpened image as compared to the existing pansharpening techniques.

5.3.1 Simulation Results

To test the proposed pansharpening scheme, dataset collected by the GeoEye-1 satellites is used. The size of the MS image for GeoEye-1 is 324×324.

To evaluate the pansharpening results, we follow the Wald's protocol [31]. According to this protocol, the PAN and MS images are degraded to the lower resolution to compare the pansharpened image with the reference original MS images [32]. The quality metrics for evaluating the quality of the pansharpened images obtained through the proposed method considered in this scheme are Q-index (Q4) [33], spectral angle mapper (SAM) [34], relative dimensionless global error (ERGAS) [31], and quality with no-reference (QNR). The QNR is composed of a spectral (D_λ) and spatial (D_S) distortion indices, without requiring high-resolution reference MS images [37].

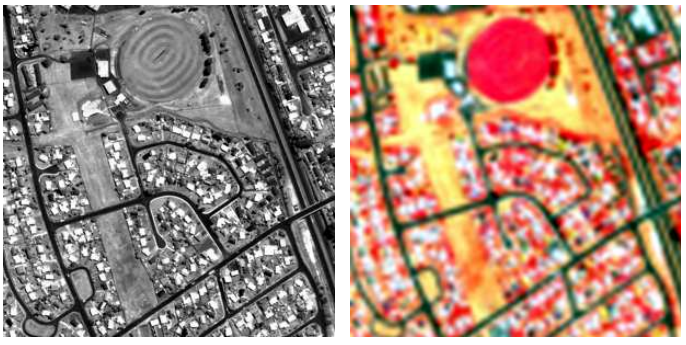

(a) (b)

FIGURE 5.4: Input images for GeoEye-1 satellite dataset are (a) PAN image, (b) EXP MS images.

In the proposed pansharpening rule given in (5.9), the value of tunning factor γ is taken as 0.73 which is selected through multiple simulation trials. The number of decomposition stages

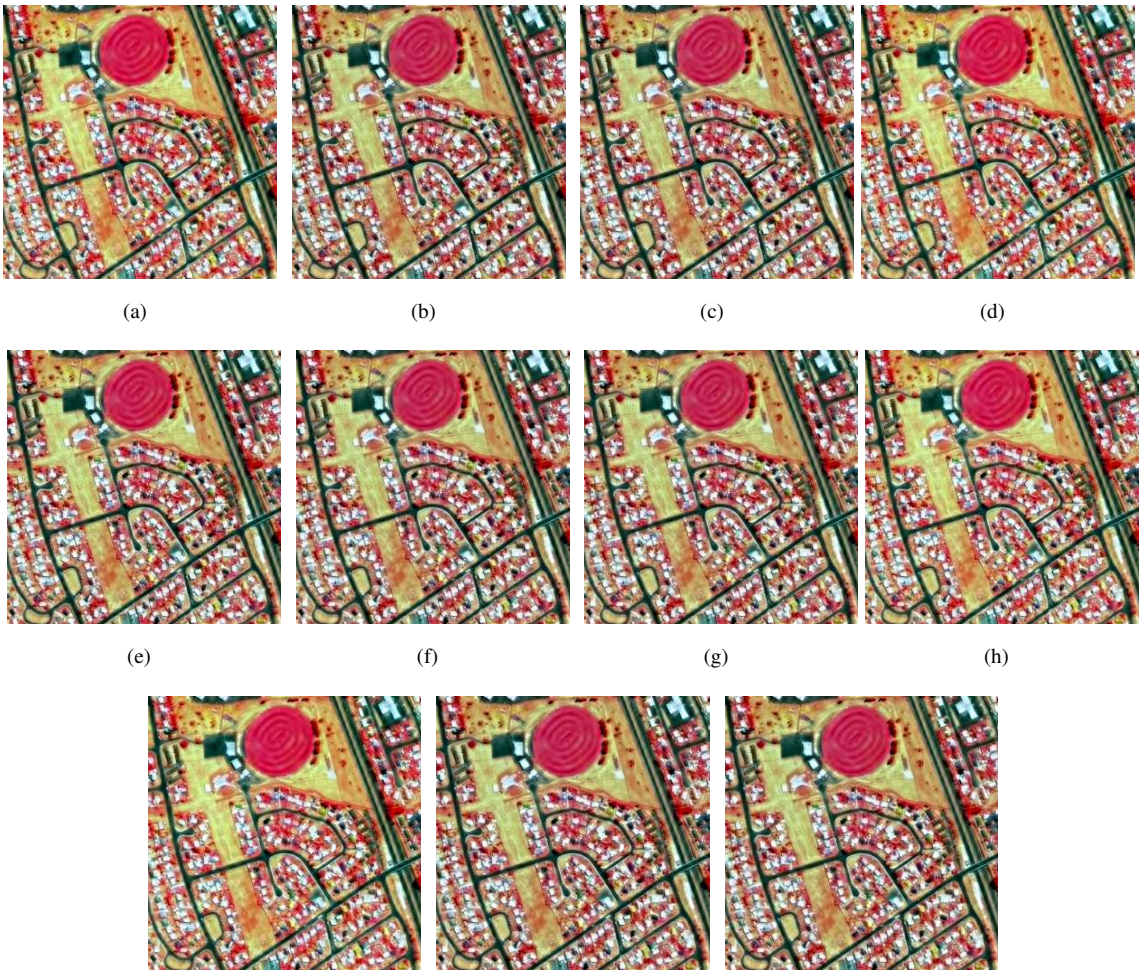

FIGURE 5.5: The Spectral quality assessments of the pansharpened images obtained by the proposed method using multistage multichannel decomposition are (a) $M_2 = 2, M_3 = 0, M_4 = 0$, (b) $M_2 = 3, M_3 = 0, M_4 = 0$, (c) $M_2 = 4, M_3 = 0, M_4 = 0$, (d) $M_2 = 2, M_3 = 2, M_4 = 0$, (e) $M_2 = 2, M_3 = 3, M_4 = 0$, (f) $M_2 = 3, M_3 = 3, M_4 = 0$, (g) $M_2 = 3, M_3 = 4, M_4 = 0$, (h) $M_2 = 2, M_3 = 3, M_4 = 4$, (i) $M_2 = 2, M_3 = 2, M_4 = 2$, (j) $M_2 = 3, M_3 = 3, M_4 = 3$, (k) $M_2 = 4, M_3 = 4, M_4 = 4$.

$(K-1)$ is taken as three since it is observed that larger values of decomposition stages increases the computational cost without significantly improving the quality of the pansharpened images. The image obtained through the re-sampling of the MS images to the size of the PAN image using interpolation [116] is labeled by EXP MS image. The input PAN and MS images for GeoEye-1 satellite dataset are shown in Fig.5.4(a) and (b).

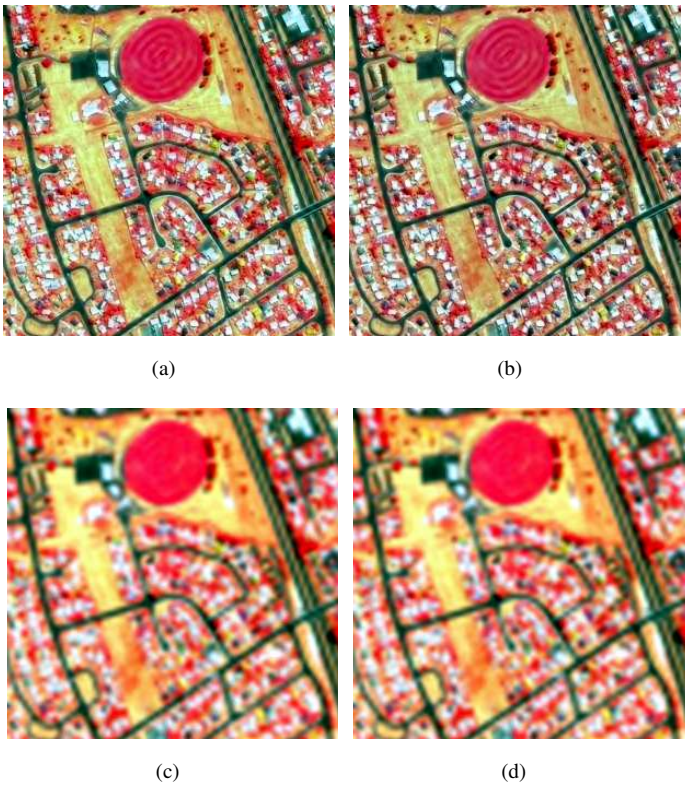

(a) (b)

(c) (d)

FIGURE 5.6: Pansharpened images obtained by the proposed pansharpening scheme using different filterbanks (a) SWF, (b) MHWF, (c) MWF, (d) SPWF.

The simulations are performed for different values of parameters M_2, M_3, and M_4 using the multistage multichannel MHWF. The obtained pansharpened images are shown in Fig.5.5(a)-5.5(k). The quality metrics Q4, SAM and ERGAS for degraded scale assessment are computed for Fig.5.5(a)-5.5(k) and results are tabulated in Table 5.1. The best values of the performance measures are highlighted as boldface numerals. It can be seen from the Table 5.1 that for parameter values of $M_2 = 2, M_3 = 3$ and $M_4 = 4$, the quality metric SAM is turning out to be better than the other values of parameters for M_2, M_3 and M_4. It can be observed that quality metrics Q4 and ERGAS values are almost same for different combinations of M_2, M_3 and M_4.

To evaluate the performance of the proposed pansharpening schemes for filterbanks based on different wavelets such as SW filterbank (SWF), MHWF, MW filterbank (MWF) and SPW filterbank (SPWF), simulations are carried out for parameter values $M_2 = 2, M_3 = 3$ and

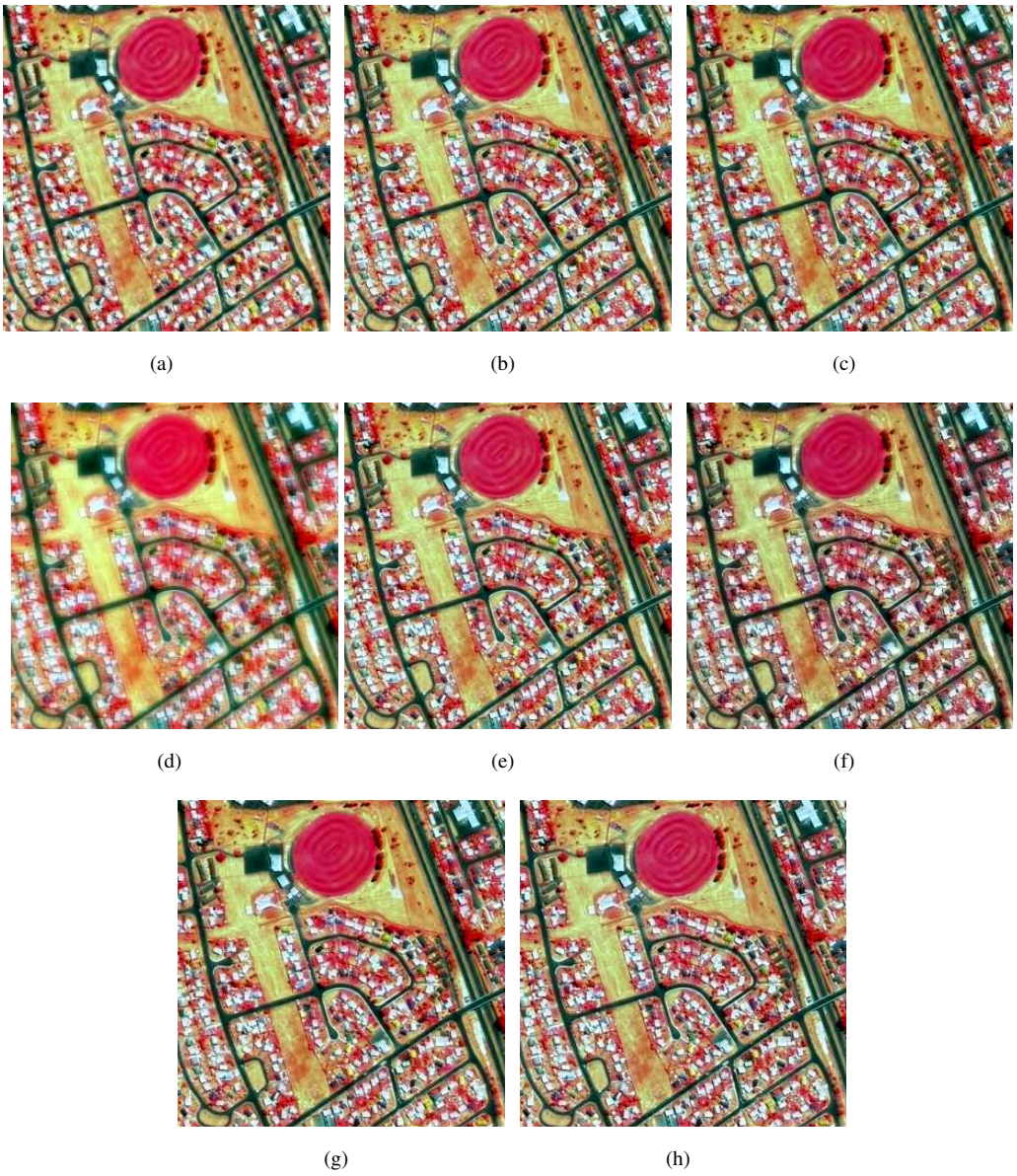

FIGURE 5.7: Pansharpened images obtained using proposed and existing pansharpening schemes (a) Proposed MHWF, (b) ATWT, (c) AWLP, (d) ATWTM2, (e) MTF-GLP, (f) GLP-PP, (g) GLP-HPM, (h) GLP-CBD.

$M_4 = 4$, and the results are shown in Fig.5.6(a)-5.6(d), respectively. It can be seen from the pansharpened image obtained by the MHWF shown in Fig.5.6(b) has better spatial and spectral details than the other filterbanks.

TABLE 5.1: The quality assessment of the pansharpened images obatined using multistage multichannel decomposition at degraded scale.

	Weighting coefficients	Degraded scale		
M_2, M_3, M_4	$\alpha_1,\ \alpha_2,\ \alpha_3$	**Q4**	**SAM**	**ERGAS**
Multi-stage (K-1)=1				
2, 0, 0	1, 0, 0	0.7627	3.6841	**2.7077**
3, 0, 0	1, 0, 0	0.7714	3.7676	2.8587
4, 0, 0	1, 0, 0	0.7713	3.7727	2.8644
Multi-stage (K-1)=2				
2, 2, 0	0.01, 0.9944, 0	0.7631	3.6811	2.7112
2, 3, 0	0.3885, 0.6066, 0	**0.7722**	3.6935	2.7717
3, 3, 0	1, 0.01, 0	0.7707	3.7690	2.8546
3, 4, 0	1, 0.01, 0	0.7707	3.7691	2.8546
Multi-stage (K-1)=3				
2, 3, 4	0.781, 0.135, 0.083	0.7681	**3.6669**	2.7150
2, 2, 2	0.023, 0.980, 0.012	0.7615	3.6811	2.7175
3, 3, 3	0.991, 0.010, 0.010	0.7706	3.7715	2.8564
4, 4, 4	0.983, 0.012, 0.013	0.7707	3.7764	2.8630

Using the above pansharpened images shown in Fig.5.6(a)-5.6(d) the quality metrics Q4, SAM, ERGAS for degraded scale assessment and D_λ, D_S, QNR for full scale assessment are computed and the results are tabulated in Table 5.2. It can be seen from the quantitative results given in Table 5.2 that the MHWF provides the better result in terms of Q4, SAM, ERGAS quality metrics as compared to the other filterbanks.

TABLE 5.2: The quality assessment of the pansharpened images obatined using different filterbanks at degraded and full scale.

	Degraded scale			Full scale		
	Q4	**SAM**	**ERGAS**	$\mathbf{D}_\lambda$	$\mathbf{D}_S$	**QNR**
Ref. value	1	0	0	0	0	1
SWF	0.7514	3.7259	2.7243	0.0337	**0.0598**	0.9086
MHWF	**0.7681**	**3.6669**	**2.7150**	0.0509	0.0942	0.8597
MWF	0.6753	4.0924	3.1383	0.0023	0.0626	**0.9353**
SPWF	0.6751	4.0927	3.1390	**0.0017**	0.0642	0.9342

To compare the simulation results obtained by proposed pansharpening method using parameter values $M_2 = 2, M_3 = 3$ and $M_4 = 4$ with multistage multichannel MHWF with the existing pansharpening schemes based on additive $\grave{a}$ trous wavelet transform with unitary injection model (ATWT) [51], additive wavelet luminance proportional (AWLP) [6], $\grave{a}$ trous

TABLE 5.3: The quality assessment of the pansharpened images using proposed and existing pansharpening schemes at degraded and full scale.

	Degraded scale			Full scale		
	Q4	**SAM**	**ERGAS**	$\mathbf{D}_\lambda$	$\mathbf{D}_S$	**QNR**
Ref.val.	1	0	0	0	0	1
MHWF	**0.7681**	3.6669	**2.7150**	**0.0509**	**0.0942**	**0.8597**
ATWT	0.7557	3.6680	2.7674	0.1203	0.1495	0.7482
AWLP	0.7445	3.7842	2.7860	0.1247	0.1493	0.7447
ATWTM2	0.6728	4.4373	3.0822	0.0761	0.0984	0.8330
MTF-GLP	0.7548	**3.661**	2.7608	0.1214	0.1467	0.7497
GLP-PP	0.7198	4.2476	3.002	0.1819	0.2083	0.6477
GLP-HPM	0.7515	3.7105	2.7822	0.1216	0.1474	0.7489
GLP-CBD	0.7591	3.7318	2.8534	0.0668	0.1077	0.8326

wavelet transform using the model-2 (ATWTM2) [50], generalized Laplacian pyramid (GLP) with modulation transfer function (MTF) matched filter using unitary injection model (MTF-GLP) [154], multiplicative injection model and post-processing (GLP-PP) [115], multiplicative injection model (GLP-HPM) [68], and regression based injection model (GLP-CBD) [155] are shown in Fig.5.7(a)-5.7(h).

It can be seen from the pansharpened images obtained by the proposed method shown in Fig.5.7(a) that it provides additional spatial and spectral information as compared to the existing pansharpening methods. Simulation results of the quality metrics using these images are tabulated in Table 5.3. It can be seen from the quantitative results given in Table 5.3 that the proposed method outperforms the other methods in terms of all the quality metrics considered in this scheme except SAM. Optimizing the weighted combination of subband information provided by the SGWF in the proposed pansharpening rule is the main reason for improved pansharpening results here.

In the proposed method, effects of aliasing and misregistration errors are evaluated by computing Q4 metric as a function of Nyquist frequency and Q4 metric as a function of misregistration displacement respectively. The simulation results of the proposed and existing schemes are shown in Fig.5.8. For aliasing error, it can be seen from Fig.5.8(a) that Q4 metric increases with

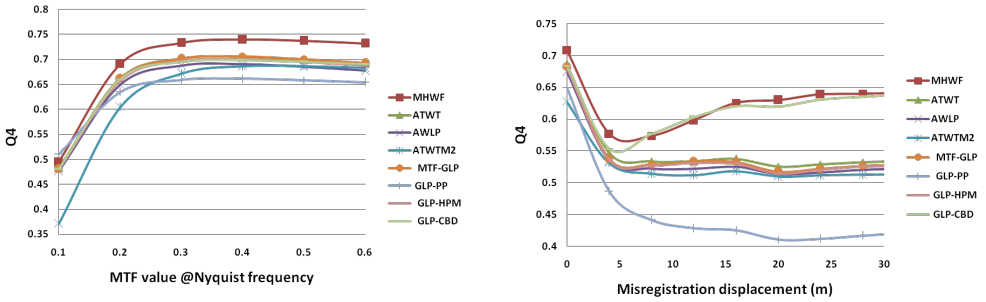

(a) (b)

FIGURE 5.8: Quality index (a) for increasing amounts of aliasing, measured by the amplitude at nyquist frequency of the Gaussian-like low-pass filter simulating the modulation transfer functions of the multispectral instrument, and (b) for increasing amounts of misregistration between MS and PAN images.

increasing Nyquist frequency values initially but becomes almost constant for higher Nyquist frequency values beyond 0.3 Hz. For misregistration errors, it can be observed from Fig.5.8(b), the parameter Q4 has attained almost a constant value after the displacement error beyond 15m. Thus it is observed that the proposed method provides better results and robustness against registration error and aliasing effect.

5.4 Proposed image fusion scheme

In the present scheme, we propose the use of SGWF for extracting additional information from source images. In the proposed image fusion scheme, the lowpass signal generated from multistage multichannel of SGWF decomposition will be used to add additional information in the source images using appropriate fusion rule. The proposed image fusion algorithm is

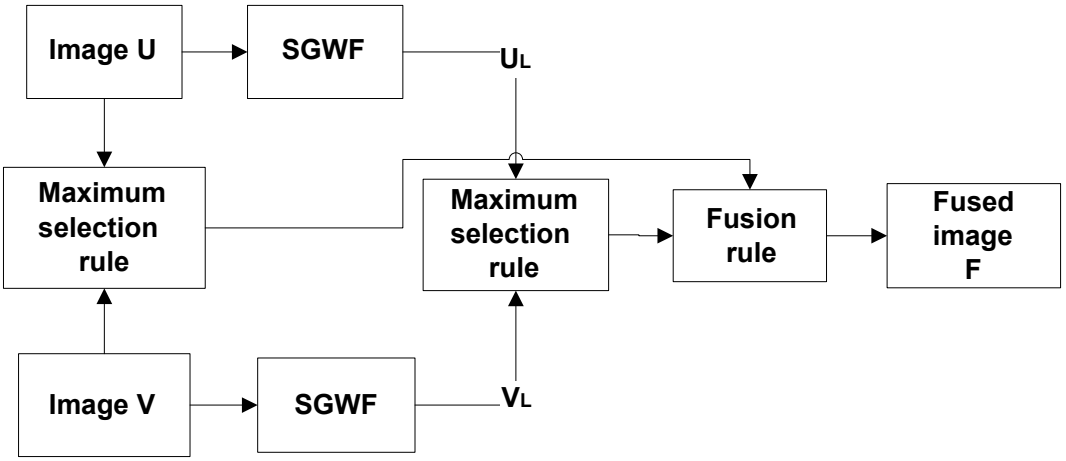

FIGURE 5.9: Block diagram of the proposed fusion scheme

illustrated in Fig.5.9. The source images U and V are decomposed by the SGWF (as shown in Fig.5.2). The details of the SGWF decomposition block is given in Fig.5.3. The output lowpass component and input signal at kth stage of decomposition in Fig.5.3, therefore, can be written as

$$\hat{U}_L^{M_{k+1}} = O_L^{M_{k+1}}(\hat{U}_L^{M_k}), \tag{5.11}$$

$$\hat{V}_L^{M_{k+1}} = O_L^{M_{k+1}}(\hat{V}_L^{M_k}), \tag{5.12}$$

where $k = 1, 2, ..., K-1$ and $K-1$ is the total stages in the SGWF decomposition and M_{k+1} denotes the number of channels at kth stage in the SGWF decomposition. Therefore, for the first stage in the decomposition $U = \hat{U}_L^{M_1}$.

Now by applying the maximum selection rule on $\hat{U}_L^{M_{k+1}}$, $\hat{V}_L^{M_{k+1}}$ images are expressed by

$$\widehat{UV}_L^{M_{k+1}}(m,n) = \begin{cases} \hat{U}_L^{M_{k+1}}(m,n), & if \;\; \hat{U}_L^{M_{k+1}}(m,n) \geq \hat{V}_L^{M_{k+1}}(m,n), \\ \hat{V}_L^{M_{k+1}}(m,n), & if \;\; \hat{U}_L^{M_{k+1}}(m,n) < \hat{V}_L^{M_{k+1}}(m,n), \end{cases} \tag{5.13}$$

Using UV and $\widehat{UV}_L^{M_{k+1}}$ images given in (3.18) and (5.13) respectively, the final fused image is obtained:

$$F(m,n) = UV(m,n) + \alpha\, \widehat{UV}_L^{M_{k+1}}(m,n), \tag{5.14}$$

where F is the fused image and α is the tunning factor. The images $\widehat{UV}_L^{M_{k+1}}$ and UV provide additional information of the source images U and V.

5.4.1 Simulation Results

Simulation results of the proposed fusion method based on SGWF are performed using MATLAB. The proposed fusion method is applied on five source image pairs which are divided into two groups (given in section 3.5.1). Simulations are also performed to compare the proposed scheme with other fusion schemes such as (i) adaptive sparse representation (ASR) based image fusion scheme [125], (ii) Discrete cosine harmonic wavelet transforms (DCHWT) based image fusion scheme [29] and (iii) cross bilateral filter (CBF) based image fusion [28]. The mexican-hat wavelet filterbank (MHWF) is used in the proposed fusion scheme. In the fusion rule given in (5.14), the value of tunning factor α is taken as 0.5 which is selected through multiple simulation trials. The number of channels M_{k+1} and decomposition stages $(K-1)$ are taken as two and one respectively, since it is observed that larger values of channels and decomposition stages increase the computational cost without significantly improving the quality of the fused image.

In the first experiment, fusion is performed on multi-sensor source image pairs. The MMW and visible source images are shown in Figs. 5.10(a) and 5.10(b). Figs. 5.10(c) shows the fused

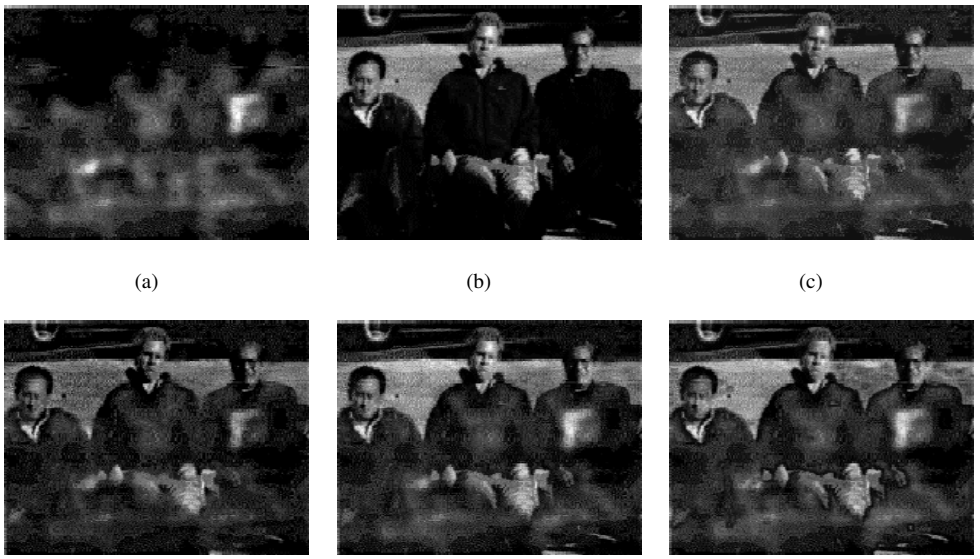

(a) (b) (c)

(d) (e) (f)

FIGURE 5.10: (a) MMW and (b) visible source images, fused image obtained by the (c) Proposed MHWF, (d) ASR, (e) DCHWT and (f) CBF based schemes

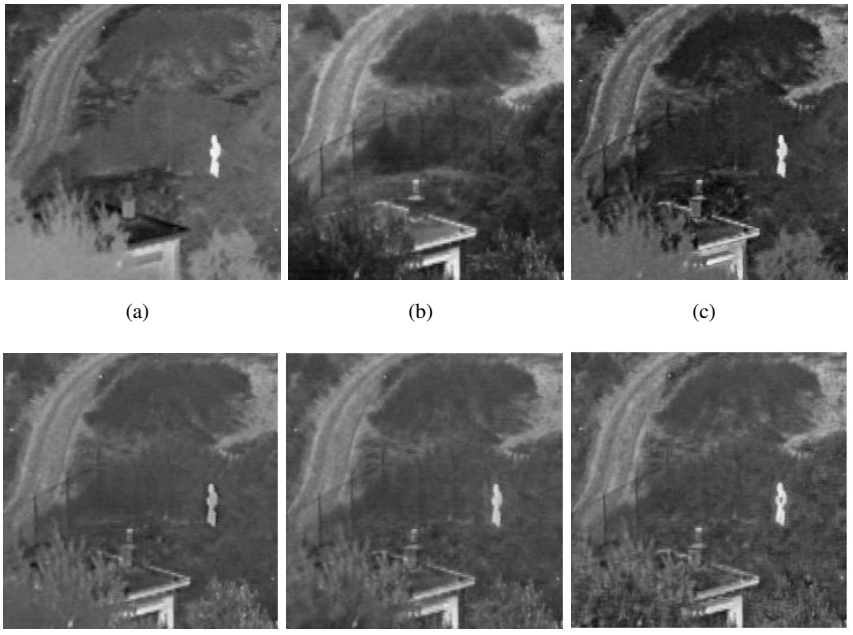

(a) (b) (c)

(d) (e) (f)

FIGURE 5.11: (a) IR and (b) visible source images, fused image obtained by the (c) Proposed MHWF, (d) ASR, (e) DCHWT and (f) CBF based schemes

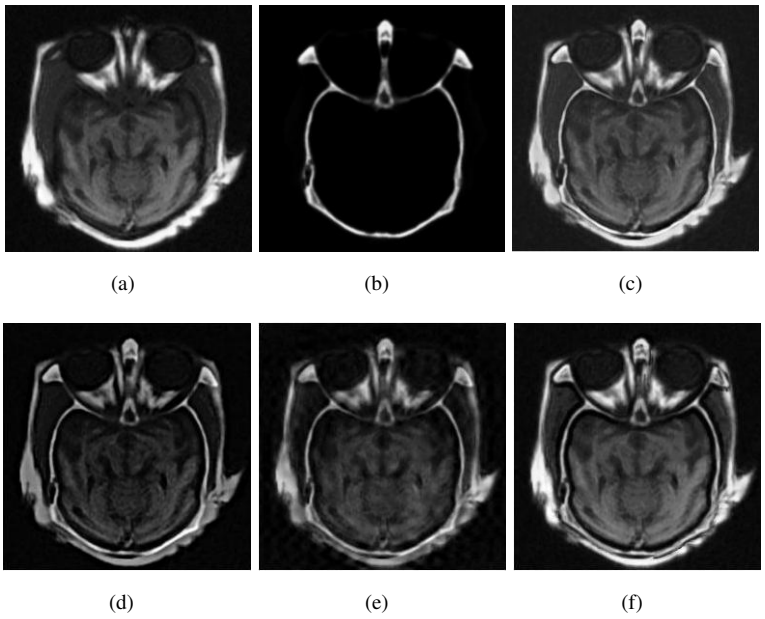

(a) (b) (c)

(d) (e) (f)

FIGURE 5.12: (a) MRI and (b) CT source images, fused image obtained by the (c) Proposed MHWF, (d) ASR, (e) DCHWT and (f) CBF based schemes

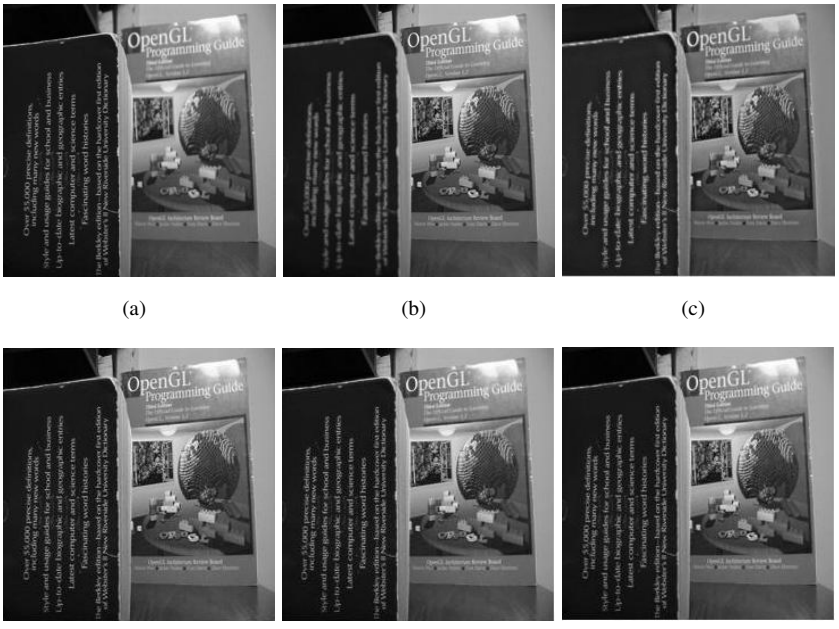

(a) (b) (c)

(d) (e) (f)

FIGURE 5.13: (a) and (b) Multi-focus Book source images, fused image obtained by the (c) Proposed MHWF, (d) ASR, (e) DCHWT and (f) CBF based schemes

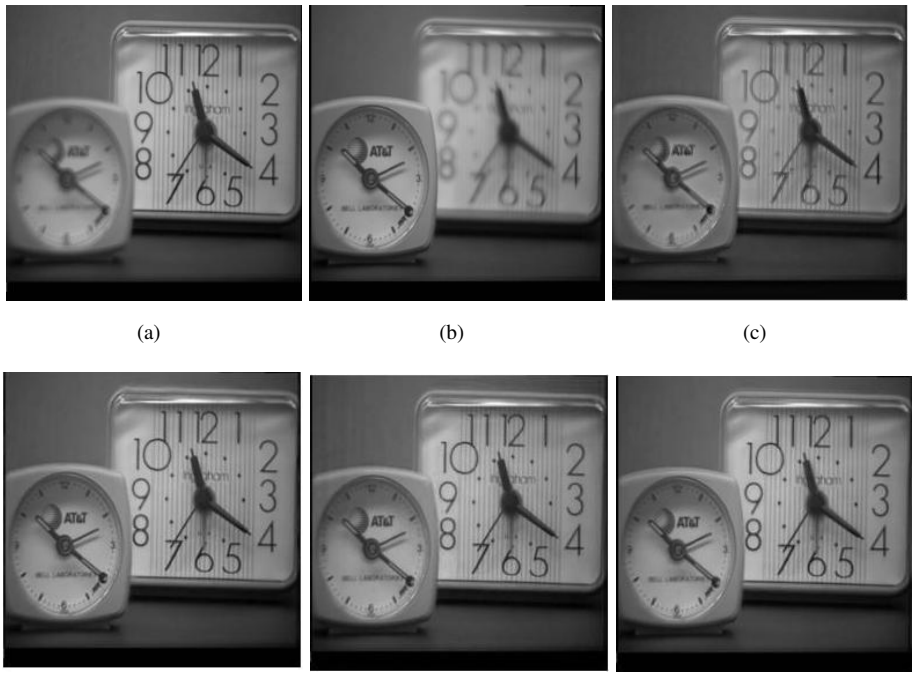

(a) (b) (c)

(d) (e) (f)

FIGURE 5.14: (a) and (b) Multi-focus Clock source images, fused image obtained by the (c) Proposed MHWF, (d) ASR, (e) DCHWT and (f) CBF based schemes

image obtained using the proposed method, and Figs. 5.10(d),(e),(f) show fused images using existing schemes given in [28, 29, 125].

The IR and visible source images are shown in Figs. 5.11(a) and 5.11(b). Figs. 5.11(c) shows the fused image obtained using the proposed method, and Figs. 5.11(d), (e), (f) show fused images using existing schemes given in [28, 29, 125].

The MRI and CT medical images are shown in Figs. 5.12(a) and 5.12(b). Figs. 5.12(c) show the fused images obtained using the proposed method and fusion results of existing schemes given in [28, 29, 125] are shown in Figs. 5.12(d), 5.12(e), 5.12(f) respectively.

In the second experiment, fusion is performed on multi-focus Book and Clock source image pairs. The multi-focus Book and Clock images are shown in Figs. 5.13(a), 5.13(b) and 5.14(a), 5.14(b). Figs. 5.13(c) and 5.14(c) shows the fused images obtained using the proposed method

and fusion results of existing schemes given in [28, 29, 125] are shown in Figs. 5.13(d), 5.13(e), 5.13(f) and Figs. 5.14(d), 5.14(e), 5.14(f).

By observing Fig.5.13 and Fig.5.14, it is clear that the fused images obtained using the proposed method are comparable to the images obtained using the existing techniques.

TABLE 5.4: Performance comparison of fused images

	API	SD	AG	H	MI	FS	CC	SF
MMW and visible source images								
MHWF	**7.8048**	**6.7815**	**3.979**	**4.4143**	**2.723**	1.8812	0.6679	**5.0877**
ASR	4.183	3.953	2.6103	3.6018	1.6531	1.9122	**0.7009**	3.2981
CBF	6.305	5.4303	2.916	4.1355	2.352	1.8994	0.6659	3.7107
DCHWT	5.4467	4.9544	2.7494	3.9545	1.7975	**1.9702**	0.6767	3.4529
IR and visible source images								
MHWF	**114.7432**	**32.3668**	**9.3547**	**6.8001**	**3.1917**	**1.9374**	0.77	**12.9256**
ASR	90.7209	24.096	6.4558	6.3054	1.7018	1.8968	**0.7968**	9.1921
CBF	89.673	27.0939	8.6559	6.4852	1.6967	1.8342	0.7532	11.3652
DCHWT	90.1042	24.696	6.7305	6.2967	1.6022	1.8344	0.7701	9.0485
MRI and CT source images								
MHWF	**61.7319**	**65.186**	12.0362	6.7645	3.7959	1.6216	0.6734	**22.1834**
ASR	31.4959	39.1903	8.3337	6.1865	2.7663	1.6602	**0.6919**	14.6749
CBF	52.875	55.5312	**12.8419**	**6.7777**	**5.3686**	1.6227	0.6592	22.0091
DCHWT	38.0233	41.9861	8.0346	6.5888	1.9772	**1.7133**	0.6845	13.3888
Book source images								
MHWF	**87.2041**	**64.3846**	**20.8155**	**7.53**	5.647	1.9839	0.9787	**34.3782**
ASR	83.1806	59.3426	16.7913	7.3419	**8.4621**	1.9904	0.9893	29.2452
CBF	82.8529	58.9722	15.3524	7.3034	8.2881	**1.9922**	**0.9906**	26.0827
DCHWT	83.0109	59.1883	16.0855	7.3315	8.1143	1.9841	0.9901	27.7148
Clock source images								
MHWF	**102.7995**	**52.4396**	9.3678	**7.4717**	6.236	**1.9838**	0.9862	14.8475
ASR	96.9211	50.5028	9.0741	7.321	7.511	1.9579	0.9879	15.4741
CBF	96.5074	50.1742	**10.4601**	7.31	**8.015**	1.9622	0.9882	**16.8638**
DCHWT	96.6567	50.2248	8.8556	7.3868	7.0283	1.9693	**0.9888**	14.6276

Table 5.4 and 5.5 shows the performance of the fusion on multi-sensor and multi-focus image pairs. The performance of the existing and proposed fusion methods are compared with the objective fidelity criterion measures such as API, SD, AG, H, MI, FS, CC, SF, $Q^{AB/F}$, $L^{AB/F}$ and $N^{AB/F}$. It is well known that for better fusion performance values of the API, SD, AG, H, MI, SF, $Q^{AB/F}$ should have higher value and $L^{AB/F}$, $N^{AB/F}$ should have lower value. In the Table 5.4 and 5.5 the best value of the performance measures are highlighted as bold face numerals. It can be observed from the Table 4.8 and 4.9 that the performance metrics API,

TABLE 5.5: Performance comparison of fused images

	$Q^{UV/F}$	$L^{UV/F}$	$N^{UV/F1}$	ans
MMW and visible source images				
MHWF	0.9345	**0.0514**	0.7002	1
ASR	0.7907	0.2092	**0.0109**	1
CBF	**0.9369**	0.0619	0.0328	1
DCHWT	0.9241	0.0756	0.0141	1
IR and visible source images				
MHWF	0.7149	**0.2162**	0.3647	1
ASR	**0.7345**	0.2621	**0.0166**	1
CBF	0.7223	0.2312	0.1371	1
DCHWT	0.7335	0.2612	0.0189	1
MRI and CT source images				
MHWF	0.8666	**0.109**	0.6507	1
ASR	0.8555	0.1426	**0.0286**	1
CBF	**0.8816**	0.1082	0.1004	1
DCHWT	0.8145	0.182	0.0297	1
Book source images				
MHWF	0.9277	**0.0068**	0.1792	1
ASR	0.9704	0.0276	0.0077	1
CBF	**0.982**	0.018	3.78E-05	1
DCHWT	0.978	0.0212	**0.0024**	1
Clock source images				
MHWF	0.8102	0.1578	0.1443	1
ASR	0.9137	0.0833	**0.022**	1
CBF	**0.9257**	**0.0742**	5.67E-04	1
DCHWT	0.9102	0.0881	0.0091	1

SD, AG, H, MI, FS, CC, SF, $Q^{AB/F}$ measures are the highest values and $L^{UV/F}$, $N^{AB/F}$ are lowest values for the proposed scheme in both of the experiments conducted. The comparative analyses show that the visual quality of the fused images is improved in the proposed method as compared to the existing methods.

5.5 Comparison of the Proposed Schemes

This section compares the proposed image fusion/pansharpening schemes using HVD, 2D-DFRFT and SGWF techniques. The comparison is categorized into (i) pansharpening schemes and (ii) image fusion schemes.

5.5.1 Pansharpening Schemes

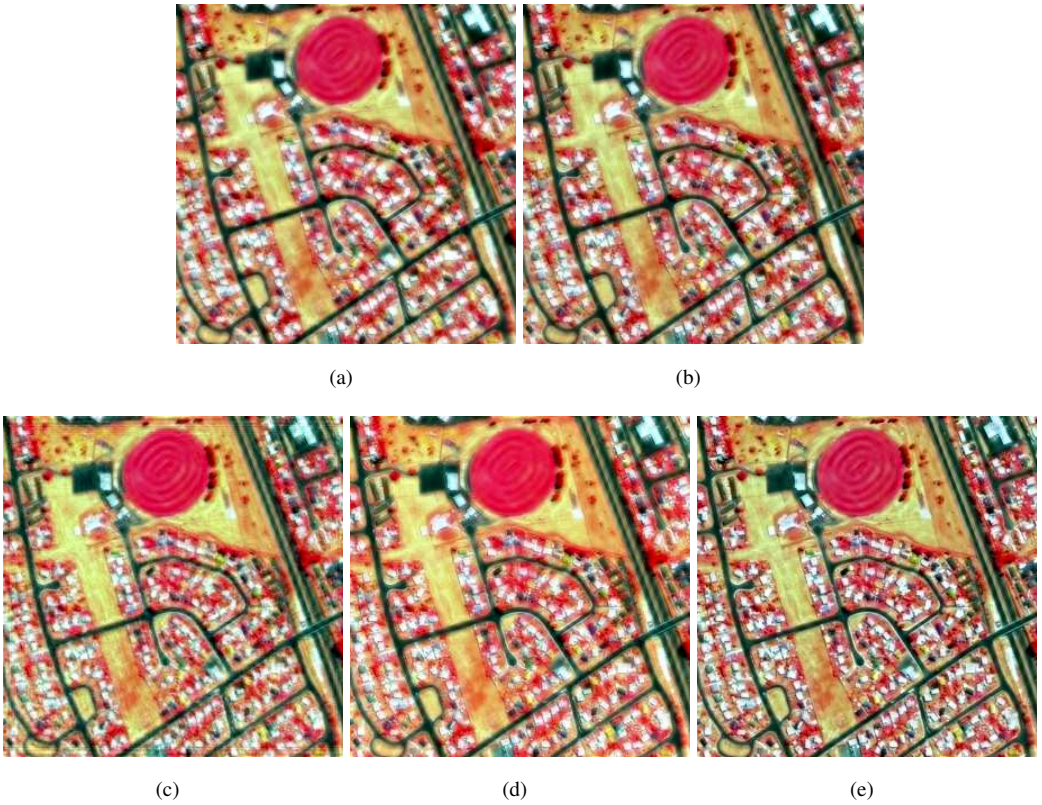

(a) (b)

(c) (d) (e)

FIGURE 5.15: Pansharpened images obtained for GeoEye-1 satellite dataset using proposed pansharpening schemes are (a) HVD_F1, (b) HVD_F2, (c) 2D-DFRFT_F1, (d) 2D-DFRFT_F2, (e) MHWF

To test the proposed pansharpening schemes, dataset collected by the GeoEye-1 satellites is used. The size of MS image is 324×324. To evaluate the pansharpening results, we follow

the Wald's protocol [31]. According to this protocol, the PAN and MS images are degraded to a lower resolution to compare the pansharpened image with the reference original MS images [32]. The quality metrics for evaluating the quality of the pansharpened images obtained through the proposed method considered in this scheme are Q-index (Q4) [33], spectral angle mapper (SAM) [34], relative dimensionless global error (ERGAS) [31], and quality with no-reference (QNR). The QNR is composed of spectral (D_λ) and spatial (D_S) distortion indices, without requiring high-resolution reference MS images [37].

TABLE 5.6: The quality assessment of the pansharpened image for proposed pansharpening schemes at degraded and full scale for GeoEye-1 satellite dataset

	Degraded scale			Full scale		
	Q4	**SAM**	**ERGAS**	**D_λ**	**D_S**	**QNR**
Ref.val.	1	0	0	0	0	1
HVD_F1	0.7578	3.7614	2.7778	0.0632	0.0945	0.8483
HVD_F2	0.7598	3.7471	2.7648	0.0801	0.1545	0.7778
2D-DFRFT_F1	0.7430	3.8497	2.8213	0.0655	**0.0388**	**0.8982**
2D-DFRFT_F2	0.7590	3.7253	2.7192	0.1623	0.0964	0.7569
MHWF	**0.7681**	**3.6669**	**2.7150**	**0.0509**	0.0942	0.8597

Simulations are performed to compare the results of the proposed pansharpening methods using HVD, 2D-DFRFT and SGWF techniques. The HVD based pansharpening scheme-I and II are denoted by the HVD_F1 and HVD_F2 respectively. Similarly, for 2D-DFRFT based proposed pansharpening scheme-I and II are labeled by the 2D-DFRFT_F1 and 2D-DFRFT_F2 respectively, and the SGWF/GSP based scheme is MHWF. The obtained pansharpened images are shown in Fig.5.15(a)-5.15(e). It is observed from the image shown in Fig.5.15(e) (obtained by the SGWF based pansharpening scheme) that the image has higher spatial and spectral resolution as compared to the other proposed methods shown in Fig.5.15(a)-5.15(d).

Simulation results of the quality metrics using images shown in Fig.5.15(a)-5.15(e) are tabulated in Table 5.6. It can be seen from the quantitative results given in Table 5.6 that the proposed method using MHWF outperforms in terms of the quality metrics Q4, SAM, ERGAS except QNR.

In degraded scale, the performance parameters Q4, SAM, and ERGAS are measure the quality index, spectral and spatial distortion of the fused image respectively [31, 33, 34] and in the full scale QNR comprises two indexes, one pertaining to spectral distortion (D_s) and other to spatial distortion (D_γ). For the better simulation results, both the full and degraded scale performances needs to provide the highest value [156]. The MHWF based proposed scheme provides better performance in degraded scale while the 2D-DFRFT_F1 gives best result in the full scale. There are minor differences in the QNR values of the MHWF and 2D-DFRFT_F1. Therefore, MHWF based proposed scheme has better results as compared to the other proposed schemes.

5.5.2 Image Fusion Schemes

This section compares the simulation results of the proposed image fusion schemes using HVD, 2D-DFRFT and SGWF techniques. The proposed fusion methods are applied on five source image pairs which are divided into two groups: (i) Multi-spectral source images and (ii) Multi-focus source images.

In the first experiment, fusion is performed on multi-spectral images:

(a) (b) (c)

FIGURE 5.16: (a) MMW and (b) visible source images, fused image obtained by the proposed schemes using (a) HVD_FS1, (b) 2D-DFRFT, (c) MHWF

(a) (b) (c)

FIGURE 5.17: (a) IR and (b) visible source images, fused image obtained by the proposed schemes using (a) HVD_FS1, (b) 2D-DFRFT, (c) MHWF

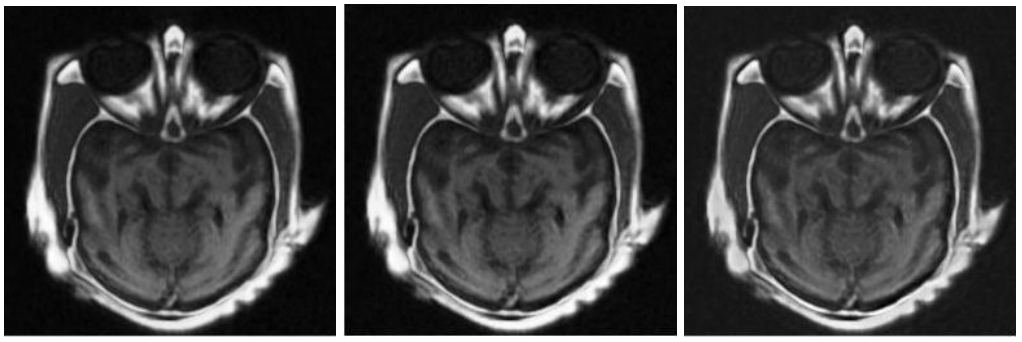

(a) (b) (c)

FIGURE 5.18: (a) MRI and (b) CT source images, fused image obtained by the proposed schemes using (a) HVD_FS1, (b) 2D-DFRFT, (c) MHWF

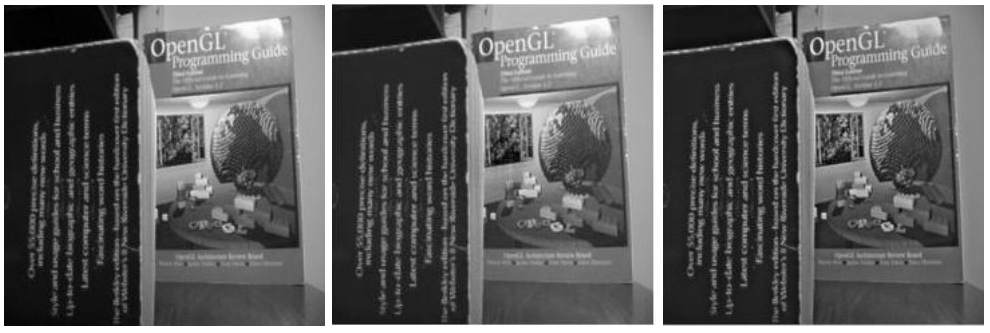

(a) (b) (c)

FIGURE 5.19: (a) and (b) Multi-focus Book source images, fused image obtained by the proposed schemes using (a) HVD_FS1, (b) 2D-DFRFT, (c) MHWF

(a) (b) (c)

FIGURE 5.20: (a) and (b) Multi-focus Clock source images, fused image obtained by the proposed schemes using (a) HVD_FS1, (b) 2D-DFRFT, (c) MHWF

TABLE 5.7: Performance comparison of fused images

	API	SD	AG	H	MI	FS	CC	SF
MMW and visible source images								
HVD_FS1	**7.8499**	6.5217	3.105	4.3959	**3.3194**	1.9	0.668	**3.9212**
2D-DFRFT	7.189	6.0515	3.0547	4.2717	3.8951	**1.905**	**0.6759**	3.869
MHWF	7.8048	**6.7815**	**3.979**	**4.4143**	2.723	1.8812	0.6679	5.0877
IR and visible source images								
HVD_FS1	122.8502	31.8585	7.1818	6.7979	4.6808	1.9289	**0.7712**	9.8086
2D-DFRFT	113.8201	30.5919	7.2281	6.76	**5.8549**	**1.9571**	0.771	9.8446
MHWF	**114.7432**	**32.3668**	**9.3547**	**6.8001**	3.1917	1.9374	0.77	**12.9256**
MRI and CT source images								
HVD_FS1	**63.4209**	63.2239	10.0173	6.7163	4.6649	1.6188	0.6726	17.8766
2D-DFRFT	58.8409	60.4562	9.9293	6.1919	**5.7489**	**1.6333**	**0.6747**	17.567
MHWF	61.7319	**65.186**	**12.0362**	**6.7645**	3.7959	1.6216	0.6734	**22.1834**
Book source images								
HVD_FS1	**94.2561**	63.7642	14.6263	7.473	8.2588	**1.9879**	**0.9901**	23.7482
2D-DFRFT	86.9253	59.9457	14.4993	7.3769	**9.2547**	1.9831	0.9899	23.5665
MHWF	87.2041	**64.3846**	**20.8155**	**7.53**	5.647	1.9839	0.9787	**34.3782**
Clock source images								
HVD_FS1	**110.8424**	**54.152**	6.9568	7.4939	7.7809	**1.9862**	0.9869	10.5717
2D-DFRFT	102.4419	50.549	6.8458	7.2874	**8.9195**	1.9749	**0.9876**	10.4878
MHWF	102.7995	52.4396	**9.3678**	**7.4717**	6.236	1.9838	0.9862	**14.8475**

1. In the millimeter wave (MMW) and visible source image fusion, Figs. 5.16(a)-(c) show the fused images obtained using the HVD, 2D-DFRFT and SGWF based proposed image methods.

2. In the infrared (IR) and visible source image fusion, Figs. 5.17(a)-(c) show fused images obtained by the proposed schemes using HVD, 2D-DFRFT and SGWF techniques.

TABLE 5.8: Performance comparison of fused images

	$Q^{UV/F}$	$L^{UV/F}$	$N^{UV/F1}$	ans
MMW and visible source images				
HVD_FS1	0.9043	0.0933	0.2216	1
2D-DFRFT	0.9011	0.0981	**0.0416**	1
MHWF	**0.9345**	**0.0514**	0.7002	1
IR and visible source images				
HVD_FS1	0.6739	0.301	**0.1768**	1
2D-DFRFT	0.6731	0.3002	0.1922	1
MHWF	**0.7149**	**0.2162**	0.3647	1
MRI and CT source images				
HVD_FS1	0.8641	0.1249	**0.5143**	1
2D-DFRFT	0.8663	0.1211	0.5511	1
MHWF	**0.8666**	**0.109**	0.6507	1
Book source images				
HVD_FS1	0.9791	0.0164	0.0174	1
2D-DFRFT	**0.9813**	0.0154	**0.0152**	1
MHWF	0.9277	**0.0068**	0.1792	1
Clock source images				
HVD_FS1	0.7354	0.2617	0.0199	1
2D-DFRFT	0.7324	0.2646	**0.0188**	1
MHWF	**0.8102**	**0.1578**	0.1443	1

3. In the MRI and CT source image fusion, Figs. 5.18(a)-(c) show fused images obtained by the proposed schemes using HVD, 2D-DFRFT and SGWF techniques.

From Figs. 5.16-5.18, it is clear that in the SGWF based proposed fusion technique is better in visual appearance than the images obtained using the other proposed fusion techniques.

In the second experiment, fusion is performed on multi-focus Book and Clock source image pairs, fused images obtained using HVD, 2D-DFRFT and MHWF based proposed image fusion schemes are shown in Fig.5.19(a)-(c) and Fig.5.20(a)-(c) respectively.

By observing Fig.5.19(c) and Fig.5.20(c), it is clear that the fused images obtained using the SGWF based proposed method is better in visual appearance as compared to the HVD and FRFT based proposed images fusion techniques.

Table 5.7 and 5.8 show the performance of the fusion on multi-spectral and multi-focus images. The comparative analyses show that the visual quality of the fused images are improved in the SGWF based proposed method as compared to the HVD and FRFT based methods.

5.6 Conclusions

In this chapter, pansharpening and image fusion schemes using the multistage multichannel approach based on graph signal processing (GSP)/spectral graph wavelet filterbank (SGWF) are proposed. In the proposed pansharpening method, the PAN image is decomposed by the multistage M-channel SGWF, and then the weighted combination of lowpass component signals in the multistage SGWF decomposition is used to generate the pansharpened image using the appropriate pansharpening rule. Simulation results of the proposed technique using the different number of channels and different filterbanks based on SW, MHW, MW and SPW for GeoEye-1 satellite images are also compared with existing pansharpening methods. It is observed that the proposed pansharpening scheme provides better pansharpening results using MHW filterbank as compared to the existing schemes. The qualitative and quantitative analysis of the presented simulation results shows that the proposed technique using parameter values $M_2 = 2, M_3 = 3$ and $M_4 = 4$ and MHWF provides improved spectral and spatial quality pansharpened image as compared to some of the existing pansharpening techniques for the GeoEye-1 satellite images. It is also seen that the proposed method is robust against aliasing and misregistration errors. In the proposed image fusion scheme, lowpass signal generated from multistage multichannel of SGWF decomposition is used to add additional information in the source images using appropriate fusion rule. The qualitative and quantitative analysis of the presented simulation results show that the proposed technique provides improved spatial quality fused image as compared to some of the existing fusion techniques. The comparative analysis of the proposed image fusion/pansharpening schemes using HVD, 2D-DFRFT and SGWF techniques shows that the

SGWF based schemes give better quantitative and qualitative results as compared to the HVD and 2D-DFRFT techniques.

Chapter 6

Conclusions and Future Scope

Image fusion is a well-recognized and a conventional field of image processing. It is designed to combine multiple input images into a fused image, which is expected to be more informative for human or machine perception as compared to any of the input images. The main objective of any image fusion is to improve the visual appearance, increase reliability, give robust system performance, provide a compact representation of information in different applications like medical imaging, remote sensing, biometrics and military, etc. Image fusion or pansharpening scheme in the remote sensing application is to keep maximum spectral details from the original images while increasing the spatial resolution. Spectral distortion is a significant issue for remote sensing, in the medical field, etc. Many algorithms are developed in these areas for better performance of the fused images.

The objective of the present research work is to developed efficient techniques for improving the spatial and spectral quality of the fused image. For attaining these objectives, image fusion/pansharpening algorithms are developed using three techniques-Hilbert vibration decomposition (HVD), fractional Fourier transforms (FRFT) and graph signal processing (GSP).

6.1 Summary of the Significant Findings

Some of the major findings of the present research work are described as follows:

- The HVD technique is used for developing the three new image fusion/pansharpening schemes for improving the spatial and spectral quality of the fused image which is closer to the filtering based approaches used in the many of the existing image fusion/pansharpening schemes. The HVD decomposes a wideband input signal into many signals in the decreasing order of the energy in terms of instantaneous amplitude and frequency components. The instantaneous amplitude of the first signal in the decomposition obtained through the HVD is similar in shape to the lowpass filtered version of a signal. This lowpass signal obtained through the HVD happens to be the highest energy component of the original signal, and it is an instantaneous frequency-based lowpass filtering of the signal. On the other hand, the output signal obtained through the conventional lowpass filtering does not take the energy of the input/output signal into account and is based on the frequency content of the input signal only. This signal energy dependent and instantaneous based filtering are the main advantages of the HVD over conventional lowpass filtering based image fusion/pansharpening approaches. Performance evaluation of fused images is done by computing fusion quality metrics, and the fusion results are compared with other existing fusion schemes. It is seen that the performance of the proposed schemes is better as compared to the existing fusion schemes.

- The 2D-discrete FRFT (2D-DFRFT) technique based three novel image fusion/pansharpening approaches are proposed for improving the spatial and spectral information of the fused image. The 2D-DFRFT is the generalized version of the conventional Fourier transform which provides the representation of a given signal in intermediate domains between spatial and fast Fourier transform (FFT) domains. The angle parameters associated with the 2D-DFRFT provides the additional degrees of freedom. Smaller values

of the angle parameters of a signal are similar in shape to the low pass filtered version of a signal, and hence it can be considered as fractional domain filtering of the signal. The 2D-DFRFT provides different representations of the given signal/image corresponding to different angles which can be optimized for better results of the image fusion/pansharpening. The fractional domain filtered signals of the source images are used for adding the spatial information to the input images for image fusion/pansharpening purpose similar to other filtered based existing approaches. The angle parameters associated with the 2D-DFRFT provide additional degrees of freedom which are optimized by single objective PSO algorithm for finding better pansharpening results. It is observed that the proposed image fusion/pansharpening schemes provide improved spectral and spatial quality as compared to the existing schemes. The effects of aliasing and misregistration errors on the proposed pansharpening methods are also investigated and compared to existing pansharpening methods. It is seen that the proposed methods are effective against aliasing and misregistration errors.

- Using the multistage multichannel GSP/SGWF, two new image fusion/pansharpening approaches are proposed. The SGWF have been utilizing the ability to decompose images into different subbands via the spectral characteristics of the images in the graph domain. The GSP exploits internode/interpixel dependence and it can be the reason for the improved results with the GSP. The time-frequency localization property and filterbanks of conventional wavelet transform have also been extended to GSP as SGWF and associated filterbanks. In the SGWF based proposed image fusion/pansharpening method, the source images are decomposed by the multistage M-channel SGWF, and then the weighted combination of lowpass component signals in the multistage SGWF decomposition is used to generate the fused image. Simulation results of the proposed technique using different wavelets such as spline wavelet (SW), mexican-hat wavelet (MHW),

meyer wavelet (MW) and simple tight frame wavelet (SPW) are also presented and compared with existing pansharpening methods in terms of both visual perception and objective metrics such as Q-index (Q4), spectral angle mapper (SAM), relative dimensionless global error (ERGAS) and quality with-no reference (QNR). It is observed that the proposed image fusion/pansharpening scheme provides better results using MHW filterbank (MHWF) as compared with some of the existing schemes. Performance evaluation of fused image is done by computing fusion quality metrics, and the fusion results are compared with other existing fusion schemes. It is seen that the performance of the proposed schemes is better as compared to the existing fusion schemes.

In a nutshell, the present research work investigates image fusion/pansharpening schemes to develop efficient techniques for improving the spatial quality and reducing the spectral distortion in the fused image. We demonstrate the applicability of the HVD, FRFT and GSP techniques in image fusion/pansharpening schemes.

6.2 Future Scope of the Research Work

In the contemporary age,the fusion of multimodality video sequences provided by a network of multimodal cameras is becoming increasingly important for surveillance purposes, navigation, and object tracking applications. The complementary information supplied by these sensors needs to be fused to obtain a more accurate estimate in order to use them more efficiently in various tasks, such as detection, recognition, tracking and situation assessment. From the fused representation of multimodality video sequences, it is possible to create a more complete and accurate representation of the perceived scene, resulting in a larger degree of situation awareness. The proposed algorithms could be extended for efficient fusion of video sequences.

Bibliography

[1] Heiko Schoder, Henry WD Yeung, Mithat Gonen, Dennis Kraus, and Steven M Larson. Head and neck cancer: Clinical usefulness and accuracy of pet/ct image fusion 1. *Radiology*, 231(1):65–72, 2004.

[2] Yong Du, Paris W Vachon, and Joost J Van der Sanden. Satellite image fusion with multiscale wavelet analysis for marine applications: preserving spatial information and minimizing artifacts (psima). *Canadian J. of Remote Sensing*, 29(1):14–23, 2003.

[3] Ying Hao, Zhenan Sun, and Tieniu Tan. Comparative studies on multispectral palm image fusion for biometrics. In *Computer Vision–ACCV 2007*, pages 12–21. Springer, 2007.

[4] Cher Hau Seng, Abdesselam Bouzerdoum, Moeness G Amin, and Son Lam Phung. Probabilistic fuzzy image fusion approach for radar through wall sensing. *Image Processing, IEEE Transactions on*, 22(12):4938–4951, 2013.

[5] Sheida Rahmani, Melissa Strait, Daria Merkurjev, Michael Moeller, and Todd Wittman. An adaptive ihs pan-sharpening method. *IEEE Geoscience and Remote Sensing Letters*, 7(4):746–750, 2010.

[6] Sheida Rahmani, Melissa Strait, Daria Merkurjev, Michael Moeller, and Todd Wittman. An adaptive pan-sharpening method. *IEEE Geoscience and Remote Sensing Letters*, 7 (4):746–750, 2010.

[7] Vijay P Shah, Nicolas H Younan, and Roger L King. An efficient pan-sharpening method via a combined adaptive pca approach and contourlets. *IEEE transactions on geoscience and remote sensing*, 46(5):1323–1335, 2008.

[8] Chen Chen, Yeqing Li, Wei Liu, and Junzhou Huang. Sirf: simultaneous satellite image registration and fusion in a unified framework. *IEEE Transactions on Image Processing*, 24(11):4213–4224, 2015.

[9] Chao Han, Thomas S Hatsukami, and Chun Yuan. A multi-scale method for automatic correction of intensity non-uniformity in mr images. *Journal of Magnetic Resonance Imaging*, 13(3):428–436, 2001.

[10] Gemma Piella. A general framework for multiresolution image fusion: from pixels to regions. *Information fusion*, 4(4):259–280, 2003.

[11] Shaohui Chen, Renhua Zhang, Hongbo Su, Jing Tian, and Jun Xia. Sar and multispectral image fusion using generalized ihs transform based on a trous wavelet and emd decompositions. *IEEE Sensors Journal*, 10(3):737–745, 2010.

[12] Rajenda Pandit Desale and Sarita V Verma. Study and analysis of pca, dct & dwt based image fusion techniques. In *Signal Processing Image Processing & Pattern Recognition (ICSIPR), 2013 International Conference on*, pages 66–69. IEEE, 2013.

[13] Michael Elad and Michal Aharon. Image denoising via sparse and redundant representations over learned dictionaries. *IEEE Transactions on Image processing*, 15(12): 3736–3745, 2006.

[14] Ayush Dogra, Sunil Agrawal, and Bhawna Goyal. Efficient representation of texture details in medical images by fusion of ripplet and ddct transformed images. *Tropical Journal of Pharmaceutical Research*, 15(9):1983–1993, 2016.

[15] Myungjin Choi, Rae Young Kim, Myeong-Ryong Nam, and Hong Oh Kim. Fusion of multispectral and panchromatic satellite images using the curvelet transform. *IEEE Geoscience and remote sensing letters*, 2(2):136–140, 2005.

[16] David L Hall and James Llinas. An introduction to multisensor data fusion. *Proceedings of the IEEE*, 85(1):6–23, 1997.

[17] Zhong Zhang and Rick S Blum. A categorization of multiscale-decomposition-based image fusion schemes with a performance study for a digital camera application. *Proceedings of the IEEE*, 87(8):1315–1326, 1999.

[18] Wenzhong Shi, ChangQing Zhu, Yan Tian, and Janet Nichol. Wavelet-based image fusion and quality assessment. *International Journal of Applied Earth Observation and Geoinformation*, 6(3):241–251, 2005.

[19] Krista Amolins, Yun Zhang, and Peter Dare. Wavelet based image fusion techniques—an introduction, review and comparison. *ISPRS Journal of Photogrammetry and Remote Sensing*, 62(4):249–263, 2007.

[20] M González-Audícana, X Otazu, O Fors, and A Seco. Comparison between mallat's and the 'à trous' discrete wavelet transform based algorithms for the fusion of multispectral and panchromatic images. *International Journal of Remote Sensing*, 26(3):595–614, 2005.

[21] Hui Li, BS Manjunath, and Sanjit K Mitra. Multisensor image fusion using the wavelet transform. *Graphical models and image processing*, 57(3):235–245, 1995.

[22] Shutao Li, James T Kwok, and Yaonan Wang. Multifocus image fusion using artificial neural networks. *Pattern Recognition Letters*, 23(8):985–997, 2002.

[23] Gao Guorong, Xu Luping, and Feng Dongzhu. Multi-focus image fusion based on non-subsampled shearlet transform. *IET Image Processing*, 7(6):633–639, 2013.

[24] Ming Yin, Wei Liu, Xia Zhao, Yanjun Yin, and Yu Guo. A novel image fusion algorithm based on nonsubsampled shearlet transform. *Optik-international journal for light and electron optics*, 125(10):2274–2282, 2014.

[25] France Laliberté, Langis Gagnon, and Yunlong Sheng. Registration and fusion of retinal images: a comparative study. In *Pattern Recognition, 2002. Proceedings. 16th International Conference on*, volume 1, pages 715–718. IEEE, 2002.

[26] France Laliberté, Langis Gagnon, and Yunlong Sheng. Registration and fusion of retinal images-an evaluation study. *IEEE Transactions on Medical Imaging*, 22(5):661–673, 2003.

[27] Y Kirankumar and S Shenbaga Devi. Transform-based medical image fusion. *International Journal of Biomedical Engineering and Technology*, 1(1):101–110, 2007.

[28] BK Shreyamsha Kumar. Image fusion based on pixel significance using cross bilateral filter. *Signal, Image and Video Processing*, pages 1–12, 2013.

[29] BK Shreyamsha Kumar. Multifocus and multispectral image fusion based on pixel significance using discrete cosine harmonic wavelet transform. *Signal, Image and Video Processing*, 7(6):1125–1143, 2013.

[30] CS Xydeas and V Petrović. Objective image fusion performance measure. *Electronics Letters*, 36(4):308–309, 2000.

[31] Lucien Wald. *Data fusion: definitions and architectures: fusion of images of different spatial resolutions*. Presses des MINES, 2002.

[32] Gemine Vivone, Luciano Alparone, Jocelyn Chanussot, Mauro Dalla Mura, Andrea Garzelli, Giorgio A Licciardi, Rocco Restaino, and Lucien Wald. A critical comparison among pansharpening algorithms. *IEEE Transactions on Geoscience and Remote Sensing*, 53(5):2565–2586, 2015.

[33] Zhou Wang and Alan C Bovik. A universal image quality index. *IEEE signal processing letters*, 9(3):81–84, 2002.

[34] Roberta H Yuhas, Alexander FH Goetz, and Joe W Boardman. Discrimination among semi-arid landscape endmembers using the spectral angle mapper (sam) algorithm. 1992.

[35] Roozbeh Rajabi and Hassan Ghassemian. Fusion of hyperspectral and panchromatic images using spectral uumixing results. *arXiv preprint arXiv:1310.5965*, 2013.

[36] Naoto Yokoya, Takehisa Yairi, and Akira Iwasaki. Coupled nonnegative matrix factorization unmixing for hyperspectral and multispectral data fusion. *IEEE Transactions on Geoscience and Remote Sensing*, 50(2):528–537, 2012.

[37] Luciano Alparone, Bruno Aiazzi, Stefano Baronti, Andrea Garzelli, Filippo Nencini, and Massimo Selva. Multispectral and panchromatic data fusion assessment without reference. *Photogrammetric Engineering & Remote Sensing*, 74(2):193–200, 2008.

[38] Michael Feldman. Time-varying vibration decomposition and analysis based on the hilbert transform. *J. of Sound and Vibration*, 295(3):518–530, 2006.

[39] Khalid H Miah and David K Potter. Geophysical signal parameterization and filtering using the fractional fourier transform. *IEEE Journal of Selected Topics in Applied Earth Observations and Remote Sensing*, 7(3):845–852, 2014.

[40] Çagatay Candan, M Alper Kutay, and Haldun M Ozaktas. The discrete fractional fourier transform. *IEEE Transactions on Signal Processing*, 48(5):1329–1337, 2000.

[41] Haldun M Ozaktas, Nilgun Erkaya, and M Alper Kutay. Effect of fractional fourier transformation on time-frequency distributions belonging to the cohen class. *IEEE signal processing letters*, 3(2):40–41, 1996.

[42] Haldun M Ozaktas and David Mendlovic. Fractional fourier transforms and their optical implementation. ii. *JOSA A*, 10(12):2522–2531, 1993.

[43] Soo-Chang Pei and Jian-Jiun Ding. Eigenfunctions of fourier and fractional fourier transforms with complex offsets and parameters. *IEEE Transactions on Circuits and Systems I: Regular Papers*, 54(7):1599–1611, 2007.

[44] Kamalesh Kumar Sharma and Shiv Dutt Joshi. Time delay estimation using fractional fourier transform. *Signal processing*, 87(5):853–865, 2007.

[45] Ahmed I Zayed. *Advances in Shannon's sampling theory*. CRC press, 1993.

[46] KK Sharma. Approximate signal reconstruction using nonuniform samples in fractional fourier and linear canonical transform domains. *IEEE Transactions on Signal Processing*, 57(11):4573–4578, 2009.

[47] Kamalesh Kumar Sharma and Shiv Dutt Joshi. Image registration using fractional fourier transform. In *APCCAS 2006-2006 IEEE Asia Pacific Conference on Circuits and Systems*, pages 470–473. IEEE, 2006.

[48] Sunil K Narang and Antonio Ortega. Perfect reconstruction two-channel wavelet filter banks for graph structured data. *IEEE Transactions on Signal Processing*, 60(6):2786–2799, 2012.

[49] Hemant Meena, Kamlesh Sharma, and Shiv Dutt Joshi. Improved facial expression recognition using graph signal processing. *Electronics Letters*, 2017.

[50] Thierry Ranchin and Lucien Wald. Fusion of high spatial and spectral resolution images: the arsis concept and its implementation. *Photogrammetric Engineering and Remote Sensing*, 66(1):49–61, 2000.

[51] Gemine Vivone, Rocco Restaino, Mauro Dalla Mura, Giorgio Licciardi, and Jocelyn Chanussot. Contrast and error-based fusion schemes for multispectral image pansharpening. *IEEE Geoscience and Remote Sensing Letters*, 11(5):930–934, 2014.

[52] Cle Pohl and John L Van Genderen. Review article multisensor image fusion in remote sensing: concepts, methods and applications. *International journal of remote sensing*, 19(5):823–854, 1998.

[53] Stavri Nikolov A. Ardeshir Goshtasby. Image fusion: Advances in the state of the art. *Information Fusion*, 8(2):114–118, 2007.

[54] Gemma Piella. A region-based multiresolution image fusion algorithm. In *Information Fusion, 2002. Proceedings of the Fifth International Conference on*, volume 2, pages 1557–1564. IEEE, 2002.

[55] Peter J Burt. A gradient pyramid basis for pattern-selective image fusion. *Proceedings of the Society for Information Display*, pages 467–470, 1992.

[56] VPS Naidu and JR Raol. Pixel-level image fusion using wavelets and principal component analysis. *Defence Science Journal*, 58(3):338, 2008.

[57] Haidawati Nasir, Vladimir Stanković, and Stephen Marshall. Singular value decomposition based fusion for super-resolution image reconstruction. *Signal Processing: Image Communication*, 27(2):180–191, 2012.

[58] Slavica Savić and Zdenka Babić. Multifocus image fusion based on the first level of empirical mode decomposition. In *Systems, Signals and Image Processing (IWSSIP), 2012 19th International Conference on*, pages 604–607. IEEE, 2012.

[59] VPS Naidu. Discrete cosine transform-based image fusion. *Defence Science J.*, 60(1): 48–54, 2010.

[60] SV Narasimhan and M Harish. Spectral estimation based on sub band decomposition by harmonic wavelet transform and modified group delay13. *Signal Processing and Communications*, pages 349–353, 2004.

[61] Shanmuganathan Raman and Subhasis Chaudhuri. A matte-less, variational approach to automatic scene compositing. In *Computer Vision, 2007. ICCV 2007. IEEE 11th International Conference on*, pages 1–6. IEEE, 2007.

[62] Ketan Kotwal and Subhasis Chaudhuri. An optimization-based approach to fusion of multi-exposure, low dynamic range images. In *Information Fusion (FUSION), 2011 Proceedings of the 14th International Conference on*, pages 1–7. IEEE, 2011.

[63] Craig A Laben and Bernard V Brower. Process for enhancing the spatial resolution of multispectral imagery using pan-sharpening, January 4 2000. US Patent 6,011,875.

[64] Pats Chavez, Stuart C Sides, Jeffrey A Anderson, et al. Comparison of three different methods to merge multiresolution and multispectral data- landsat tm and spot panchromatic. *Photogrammetric Engineering and remote sensing*, 57(3):295–303, 1991.

[65] Alan R Gillespie, Anne B Kahle, and Richard E Walker. Color enhancement of highly correlated images. ii. channel ratio and "chromaticity" transformation techniques. *Remote Sensing of Environment*, 22(3):343–365, 1987.

[66] Bruno Aiazzi, Stefano Baronti, and Massimo Selva. Improving component substitution pansharpening through multivariate regression of ms+ pan data. *IEEE Transactions on Geoscience and Remote Sensing*, 45(10):3230–3239, 2007.

[67] Claire Thomas, Thierry Ranchin, Lucien Wald, and Jocelyn Chanussot. Synthesis of multispectral images to high spatial resolution: A critical review of fusion methods based on remote sensing physics. *IEEE Transactions on Geoscience and Remote Sensing*, 46 (5):1301–1312, 2008.

[68] B Aiazzi, L Alparone, S Baronti, A Garzelli, and M Selva. An mtf-based spectral distortion minimizing model for pan-sharpening of very high resolution multispectral images of urban areas. In *Remote Sensing and Data Fusion over Urban Areas, 2003. 2nd GRSS/ISPRS Joint Workshop on*, pages 90–94. IEEE, 2003.

[69] Wojciech Czaja, Timothy Doster, and James M Murphy. Wavelet packet mixing for image fusion and pan-sharpening. In *SPIE Defense+ Security*, pages 908803–908803. International Society for Optics and Photonics, 2014.

[70] Altan-Ulzii Moonon, Jianwen Hu, and Shutao Li. Remote sensing image fusion method based on nonsubsampled shearlet transform and sparse representation. *Sensing and Imaging*, 16(1):23, 2015.

[71] Jorge Nunez, Xavier Otazu, Octavi Fors, Albert Prades, Vicenc Pala, and Roman Arbiol. Multiresolution-based image fusion with additive wavelet decomposition. *IEEE Transactions on Geoscience and Remote sensing*, 37(3):1204–1211, 1999.

[72] María González-Audícana, José Luis Saleta, Raquel García Catalán, and Rafael García. Fusion of multispectral and panchromatic images using improved ihs and pca mergers based on wavelet decomposition. *IEEE Transactions on Geoscience and Remote sensing*, 42(6):1291–1299, 2004.

[73] Min Guo, Hongyan Zhang, Jiayi Li, Liangpei Zhang, and Huanfeng Shen. An online coupled dictionary learning approach for remote sensing image fusion. *IEEE Journal of Selected Topics in Applied Earth Observations and Remote Sensing*, 7(4):1284–1294, 2014.

[74] Fardin Mirzapour and Hassan Ghassemian. Improving hyperspectral image classification by combining spectral, texture, and shape features. *International Journal of Remote Sensing*, 36(4):1070–1096, 2015.

[75] Meysam Golipour, Hassan Ghassemian, and Fardin Mirzapour. Integrating hierarchical segmentation maps with mrf prior for classification of hyperspectral images in a bayesian framework. *IEEE Transactions on Geoscience and Remote Sensing*, 54(2):805–816, 2016.

[76] Morteza Ghahremani and Hassan Ghassemian. A compressed-sensing-based pan-sharpening method for spectral distortion reduction. *IEEE Transactions on Geoscience and Remote Sensing*, 54(4):2194–2206, 2016.

[77] Peter J Burt and Raymond J Kolczynski. Enhanced image capture through fusion. In *Computer Vision, 1993. Proceedings., Fourth International Conference on*, pages 173–182. IEEE, 1993.

[78] Alexander Toet. Hierarchical image fusion. *Machine Vision and Applications*, 3(1): 1–11, 1990.

[79] Alexander Toet. Multiscale contrast enhancement with applications to image fusion. *Optical Engineering*, 31(5):1026–1031, 1992.

[80] Zheng Liu, Kazuhiko Tsukada, Koichi Hanasaki, Yeong-Khing Ho, and YP Dai. Image fusion by using steerable pyramid. *Pattern Recognition Letters*, 22(9):929–939, 2001.

[81] Eero P Simoncelli and William T Freeman. The steerable pyramid: A flexible architecture for multi-scale derivative computation. In *Image Processing, 1995. Proceedings., International Conference on*, volume 3, pages 444–447. IEEE, 1995.

[82] Chen Ye Wen and Jia Ken Chen. Multi-resolution image fusion technique and its application to forensic science. *Forensic Science International*, 140(2):217–232, 2004.

[83] Rafael Redondo, F Šroubek, S Fischer, and Gabriel Cristóbal. Multifocus image fusion using the log-gabor transform and a multisize windows technique. *Information Fusion*, 10(2):163–171, 2009.

[84] Bruno Aiazzi, Luciano Alparone, Stefano Baronti, and Andrea Garzelli. Context-driven fusion of high spatial and spectral resolution images based on oversampled multiresolution analysis. *IEEE Transactions on geoscience and remote sensing*, 40(10):2300–2312, 2002.

[85] Norden E Huang, Zheng Shen, Steven R Long, Manli C Wu, Hsing H Shih, Quanan Zheng, Nai-Chyuan Yen, Chi Chao Tung, and Henry H Liu. The empirical mode decomposition and the hilbert spectrum for nonlinear and non-stationary time series analysis. In *Proceedings of the Royal Society of London A: Mathematical, Physical and Engineering Sciences*, volume 454, pages 903–995. The Royal Society, 1998.

[86] Harishwaran Hariharan, Andrei Gribok, Mongi A Abidi, and Andreas Koschan. Image fusion and enhancement via empirical mode decomposition. *J. of Pattern Recognition Research*, 1:16–32, 2006.

[87] Yangrong Ling, Manfred Ehlers, E Lynn Usery, and Marguerite Madden. Fft enhanced ihs transform method for fusing high-resolution satellite images. *ISPRS Journal of photogrammetry and Remote Sensing*, 61(6):381–392, 2007.

[88] Morteza Ghahremani and Hassan Ghassemian. Remote sensing image fusion using ripplet transform and compressed sensing. *IEEE Geoscience and Remote Sensing Letters*, 12(3):502–506, 2015.

[89] Hamid Reza Shahdoosti and Hassan Ghassemian. Fusion of ms and pan images preserving spectral quality. *IEEE Geoscience and Remote Sensing Letters*, 12(3):611–615, 2015.

[90] Libao Zhang and Jue Zhang. A new saliency-driven fusion method based on complex wavelet transform for remote sensing images. *IEEE Geoscience and Remote Sensing Letters*, 14(12):2433–2437, 2017.

[91] Hamid Reza Shahdoosti and Nayereh Javaheri. Pansharpening of clustered ms and pan images considering mixed pixels. *IEEE Geoscience and Remote Sensing Letters*, 14(6): 826–830, 2017.

[92] Xudong Guan, Gaohuan Liu, Chong Huang, Qingsheng Liu, Chunsheng Wu, Yan Jin, and Yafei Li. An object-based linear weight assignment fusion scheme to improve classification accuracy using landsat and modis data at the decision level. *IEEE Transactions on Geoscience and Remote Sensing*, 55(12):6989–7002, 2017.

[93] Grant J Scott, Richard A Marcum, Curt H Davis, and Tyler W Nivin. Fusion of deep convolutional neural networks for land cover classification of high-resolution imagery. *IEEE Geoscience and Remote Sensing Letters*, 14(9):1638–1642, 2017.

[94] Bin Hou, Yunhong Wang, and Qingjie Liu. Change detection based on deep features and low rank. *IEEE Geoscience and Remote Sensing Letters*, 14(12):2418–2422, 2017.

[95] Zhenfeng Shao and Jiajun Cai. Remote sensing image fusion with deep convolutional neural network. *IEEE Journal of Selected Topics in Applied Earth Observations and Remote Sensing*, 11(5):1656–1669, 2018.

[96] Yong Yang, Lei Wu, Shuying Huang, Weiguo Wan, and Yue Que. Remote sensing image fusion based on adaptively weighted joint detail injection. *IEEE Access*, 6:6849–6864, 2018.

[97] Weiwei Sun and Ruisheng Wang. Fully convolutional networks for semantic segmentation of very high resolution remotely sensed images combined with dsm. *IEEE Geoscience and Remote Sensing Letters*, 15(3):474–478, 2018.

[98] Wei Huang, Liang Xiao, Zhihui Wei, Hongyi Liu, and Songze Tang. A new pan-sharpening method with deep neural networks. *IEEE Geoscience and Remote Sensing Letters*, 12(5):1037–1041, 2015.

[99] Qiangqiang Yuan, Yancong Wei, Xiangchao Meng, Huanfeng Shen, and Liangpei Zhang. A multiscale and multidepth convolutional neural network for remote sensing imagery pan-sharpening. *IEEE Journal of Selected Topics in Applied Earth Observations and Remote Sensing*, 11(3):978–989, 2018.

[100] Laetitia Loncan, Luis B de Almeida, José M Bioucas-Dias, Xavier Briottet, Jocelyn Chanussot, Nicolas Dobigeon, Sophie Fabre, Wenzhi Liao, Giorgio A Licciardi, Miguel Simoes, et al. Hyperspectral pansharpening: A review. *IEEE Geoscience and remote sensing magazine*, 3(3):27–46, 2015.

[101] Carlos Souza, Laurel Firestone, Luciano Moreira Silva, and Dar Roberts. Mapping forest degradation in the eastern amazon from spot 4 through spectral mixture models. *Remote Sensing of Environment*, 87(4):494–506, 2003.

[102] Francesca Bovolo and Lorenzo Bruzzone. The time variable in data fusion: A change detection perspective. *IEEE Geoscience and Remote Sensing Magazine*, 3(3):8–26, 2015.

[103] Ali Mohammadzadeh, Ahad Tavakoli, Valadan Zoej, and J Mohammad. Road extraction based on fuzzy logic and mathematical morphology from pan-sharpened ikonos images. *The photogrammetric record*, 21(113):44–60, 2006.

[104] Miaomiao Liu, Xinde Li, Jean Dezert, and Chaomin Luo. Generic object recognition based on the fusion of 2d and 3d sift descriptors. In *Information Fusion (Fusion), 2015 18th International Conference on*, pages 1085–1092. IEEE, 2015.

[105] Mrinal Kanti Bhowmik, Barin Kumar De, Debotosh Bhattacharjee, Dipak Kumar Basu, and Mita Nasipuri. Multisensor fusion of visual and thermal images for human face identification using different svm kernels. In *Systems, Applications and Technology Conference (LISAT), 2012 IEEE Long Island*, pages 1–7. IEEE, 2012.

[106] Florence Laporterie-Déjean, Hélène de Boissezon, Guy Flouzat, and Marie-José Lefèvre-Fonollosa. Thematic and statistical evaluations of five panchromatic/multispectral fusion methods on simulated pleiades-hr images. *Information Fusion*, 6(3):193–212, 2005.

[107] Lucien Wald, Thierry Ranchin, and Marc Mangolini. Fusion of satellite images of different spatial resolutions: assessing the quality of resulting images. *Photogrammetric engineering and remote sensing*, 63(6):691–699, 1997.

[108] Ronald Newbold Bracewell and Ronald N Bracewell. *The Fourier transform and its applications*, volume 31999. McGraw-Hill New York, 1986.

[109] Weihua Dong, Xian'en Li, Xiangguo Lin, and Zhilin Li. A bidimensional empirical mode decomposition method for fusion of multispectral and panchromatic remote sensing images. *Remote Sensing*, 6(9):8446–8467, 2014.

[110] Lutfiye Durak and Orhan Arikan. Short-time fourier transform: two fundamental properties and an optimal implementation. *IEEE Transactions on Signal Processing*, 51(5): 1231–1242, 2003.

[111] Robert X Gao and Ruqiang Yan. From fourier transform to wavelet transform: A historical perspective. In *Wavelets*, pages 17–32. Springer, 2011.

[112] Y Huang, Cj Yan, and Q Xu. On the difference between empirical mode decomposition and hilbert vibration decomposition for earthquake motion records.

[113] http://www.dsp.etfbl.net/mif/. .

[114] JJ Ramos, JI Reyes, and E Barocio. An improved hilbert vibration decomposition method for analysis of low frequency oscillations. In *Transmission & Distribution Conference and Exposition-Latin America (PES T&D-LA), 2014 IEEE PES*, pages 1–6. IEEE, 2014.

[115] Jonghwa Lee and Chulhee Lee. Fast and efficient panchromatic sharpening. *IEEE transactions on geoscience and remote sensing*, 48(1):155–163, 2010.

[116] Bruno Aiazzi, Stefano Baronti, Massimo Selva, and Luciano Alparone. Bi-cubic interpolation for shift-free pan-sharpening. *ISPRS journal of photogrammetry and remote sensing*, 86:65–76, 2013.

[117] http://hitech.technion.ac.il/feldman/hvd.html. .

[118] Muhammad Murtaza Khan, Jocelyn Chanussot, Laurent Condat, and Annick Montanvert. Indusion: Fusion of multispectral and panchromatic images using the induction scaling technique. *IEEE Geoscience and Remote Sensing Letters*, 5(1):98–102, 2008.

[119] Robert O Green, Michael L Eastwood, Charles M Sarture, Thomas G Chrien, Mikael Aronsson, Bruce J Chippendale, Jessica A Faust, Betina E Pavri, Christopher J Chovit, Manuel Solis, et al. Imaging spectroscopy and the airborne visible/infrared imaging spectrometer (aviris). *Remote Sensing of Environment*, 65(3):227–248, 1998.

[120] Gemine Vivone, Rocco Restaino, Giorgio Licciardi, Mauro Dalla Mura, and Jocelyn Chanussot. Multiresolution analysis and component substitution techniques for hyperspectral pansharpening. In *Geoscience and remote sensing symposium (IGARSS), 2014 IEEE international*, pages 2649–2652. IEEE, 2014.

[121] Wenzhi Liao, Xin Huang, Frieke Van Coillie, Sidharta Gautama, Aleksandra Pižurica, Wilfried Philips, Hui Liu, Tingting Zhu, Michal Shimoni, Gabriele Moser, et al. Processing of multiresolution thermal hyperspectral and digital color data: Outcome of the 2014 ieee grss data fusion contest. *IEEE Journal of Selected Topics in Applied Earth Observations and Remote Sensing*, 8(6):2984–2996, 2015.

[122] N Saxena and K. K. Sharma. A novel pansharpening approach using hilbert vibration decomposition. *Image Processing, IET, Accepted*, 2017.

[123] Luciano Alparone, Stefano Baronti, Bruno Aiazzi, and Andrea Garzelli. Spatial methods for multispectral pansharpening: Multiresolution analysis demystified. *IEEE Transactions on Geoscience and Remote Sensing*, 54(5):2563–2576, 2016.

[124] The image fusion server, http://www.imagefusion.org/. .

[125] Yu Liu and Zengfu Wang. Simultaneous image fusion and denoising with adaptive sparse representation. *Image Processing, IET*, 9(5):347–357, 2014.

[126] Yadong Song, Wei Wu, Zheng Liu, Xiaomin Yang, Kai Liu, and Wei Lu. An adaptive pansharpening method by using weighted least squares filter. *IEEE Geoscience and Remote Sensing Letters*, 13(1):18–22, 2016.

[127] Yun Zhang. Understanding image fusion. *Photogrammetric engineering and remote sensing*, 70(6):657–661, 2004.

[128] Hassan Ghassemian. A review of remote sensing image fusion methods. *Information Fusion*, 32:75–89, 2016.

[129] Wenlong Lu, Junwei Xie, Heming Wang, and Chuan Sheng. Non-stationary component extraction in noisy multicomponent signal using polynomial chirping fourier transform. *SpringerPlus*, 5(1):1177, 2016.

[130] Haldun M Ozaktas, Billur Barshan, and David Mendlovic. Convolution and filtering in fractional fourier domains. *Optical Review*, 1(1):15–16, 1994.

[131] Alper Kutay, Haldun M Ozaktas, Orhan Ankan, and Levent Onural. Optimal filtering in fractional fourier domains. *IEEE Transactions on Signal Processing*, 45(5):1129–1143, 1997.

[132] Soo-Chang Pei and Min-Hung Yeh. Two dimensional discrete fractional fourier transform. *Signal Processing*, 67(1):99–108, 1998.

[133] V Ashok Narayanan and KMM Prabhu. The fractional fourier transform: theory, implementation and error analysis. *Microprocessors and Microsystems*, 27(10):511–521, 2003.

[134] Soo-Chang Pei and Min-Hung Yeh. Discrete fractional fourier transform. In *Circuits and Systems, 1996. ISCAS'96., Connecting the World., 1996 IEEE International Symposium on*, volume 2, pages 536–539. IEEE, 1996.

[135] Soo-Chang Pei and Min-Hung Yeh. Improved discrete fractional fourier transform. *Optics letters*, 22(14):1047–1049, 1997.

[136] Jagdish Chand Bansal, PK Singh, Mukesh Saraswat, Abhishek Verma, Shimpi Singh Jadon, and Ajith Abraham. Inertia weight strategies in particle swarm optimization. In *Nature and Biologically Inspired Computing (NaBIC), 2011 Third World Congress on*, pages 633–640. IEEE, 2011.

[137] Pedram Ghamisi, Micael S Couceiro, Fernando ML Martins, and Jon Atli Benediktsson. Multilevel image segmentation based on fractional-order darwinian particle swarm optimization. *IEEE Transactions on Geoscience and Remote sensing*, 52(5):2382–2394, 2014.

[138] K Kuppusamy and K Thamodaran. Optimized image watermarking scheme based on pso. *Procedia Engineering*, 38:493–503, 2012.

[139] Wenqing Wang, Licheng Jiao, and Shuyuan Yang. Novel adaptive component-substitution-based pan-sharpening using particle swarm optimization. *IEEE Geoscience and Remote Sensing Letters*, 12(4):781–785, 2015.

[140] Jianbin Xin, Guimin Chen, and Yubao Hai. A particle swarm optimizer with multi-stage linearly-decreasing inertia weight. In *Computational Sciences and Optimization, 2009. CSO 2009. International Joint Conference on*, volume 1, pages 505–508. IEEE, 2009.

[141] Russ C Eberhart, James Kennedy, et al. A new optimizer using particle swarm theory. In *Proceedings of the sixth international symposium on micro machine and human science*, volume 1, pages 39–43. New York, NY, 1995.

[142] James Kennedy. Particle swarm optimization. In *Encyclopedia of machine learning*, pages 760–766. Springer, 2011.

[143] Stefano Baronti, Bruno Aiazzi, Massimo Selva, Andrea Garzelli, and Luciano Alparone. A theoretical analysis of the effects of aliasing and misregistration on pansharpened imagery. *IEEE Journal of Selected Topics in Signal Processing*, 5(3):446–453, 2011.

[144] Yuhui Shi and Russell C Eberhart. Empirical study of particle swarm optimization. In *Evolutionary Computation, 1999. CEC 99. Proceedings of the 1999 Congress on*, volume 3, pages 1945–1950. IEEE, 1999.

[145] Mahamad Nabab Alam. Particle swarm optimization: Algorithm and its codes in matlab, 2016.

[146] N Saxena and KK Sharma. Hilbert vibration decomposition based image fusion. *Electronics Letters*, 52(19):1605–1607, 2016.

[147] David K Hammond, Pierre Vandergheynst, and Rémi Gribonval. Wavelets on graphs via spectral graph theory. *Applied and Computational Harmonic Analysis*, 30(2):129–150, 2011.

[148] Sunil K Narang, Yung Hsuan Chao, and Antonio Ortega. Graph-wavelet filterbanks for edge-aware image processing. In *Statistical Signal Processing Workshop (SSP), 2012 IEEE*, pages 141–144. IEEE, 2012.

[149] Giulia Fracastoro and Enrico Magli. Predictive graph construction for image compression. In *Image Processing (ICIP), 2015 IEEE International Conference on*, pages 2204–2208. IEEE, 2015.

[150] Frosti Palsson, Johannes R Sveinsson, Magnus Orn Ulfarsson, and Jon Atli Benediktsson. Mtf-based deblurring using a wiener filter for cs and mra pansharpening methods. *IEEE Journal of Selected Topics in Applied Earth Observations and Remote Sensing*, 9 (6):2255–2269, 2016.

[151] Bruno Aiazzi, Stefano Baronti, Franco Lotti, and Massimo Selva. A comparison between global and context-adaptive pansharpening of multispectral images. *IEEE Geoscience and Remote Sensing Letters*, 6(2):302–306, 2009.

[152] W Joseph Carper. The use of intensity-hue-saturation transformations for merging spot panchromatic and multispectral image data. *Photogramm. Eng. Remote Sens.*, 56(4): 457–467, 1990.

[153] Akie Sakiyama and Yuichi Tanaka. Oversampled graph laplacian matrix for graph filter banks. *IEEE Transactions on Signal Processing*, 62(24):6425–6437, 2014.

[154] B Aiazzi, L Alparone, S Baronti, A Garzelli, and M Selva. Mtf-tailored multiscale fusion of high-resolution ms and pan imagery. *Photogrammetric Engineering & Remote Sensing*, 72(5):591–596, 2006.

[155] Luciano Alparone, Lucien Wald, Jocelyn Chanussot, Claire Thomas, Paolo Gamba, and Lori Mann Bruce. Comparison of pansharpening algorithms: Outcome of the 2006 grs-s data-fusion contest. *IEEE Transactions on Geoscience and Remote Sensing*, 45(10): 3012–3021, 2007.

[156] P Jagalingam and Arkal Vittal Hegde. A review of quality metrics for fused image. *Aquatic Procedia*, 4:133–142, 2015.

[157] Hannu Olkkonen and Peitsa Pesola. Gaussian pyramid wavelet transform for multiresolution analysis of images. *Graphical Models and Image Processing*, 58(4):394–398, 1996.

[158] Peter Burt and Edward Adelson. The laplacian pyramid as a compact image code. *IEEE Transactions on communications*, 31(4):532–540, 1983.

[159] Om Prakash and Ashish Khare. Ct and mr images fusion based on stationary wavelet transform by modulus maxima. In *Computational Vision and Robotics*, pages 199–204. Springer, 2015.

[160] K Kannan, S Arumuga Perumal, and K Arulmozhi. Performance comparison of various levels of fusion of multi-focused images using wavelet transform. *International Journal of Computer Applications*, 1(6):71–78, 2010.

[161] Somkait Udomhunsakul, Pradab Yamsang, Suwut Tumthong, and Pusit Borwonwatanadelok. Multiresolution edge fusion using swt and sfm. In *Proceedings of the World Congress on Engineering*, volume 2, pages 6–8, 2011.

[162] Shivsubramani Krishnamoorthy and KP Soman. Implementation and comparative study of image fusion algorithms. *International Journal of Computer Applications (0975–8887) Volume*, 2010.

[163] Gonzalo Pajares and Jesus Manuel De La Cruz. A wavelet-based image fusion tutorial. *Pattern recognition*, 37(9):1855–1872, 2004.

[164] Stéphane Mallat. *A wavelet tour of signal processing*. Academic press, 1999.

[165] Rajiv Singh and Ashish Khare. Multiscale medical image fusion in wavelet domain. *The Scientific World Journal*, 2013, 2013.

[166] VPS Naidu. Discrete cosine transform based image fusion techniques. *Journal of Communication, Navigation and Signal Processing*, 1(1):35–45, 2012.

[167] Zhijun Wang, Djemel Ziou, Costas Armenakis, Deren Li, and Qingquan Li. A comparative analysis of image fusion methods. *IEEE transactions on geoscience and remote sensing*, 43(6):1391–1402, 2005.

[168] Lindsay I Smith et al. A tutorial on principal components analysis. *Cornell University, USA*, 51(52):65, 2002.

[169] Le Song, Yuchi Lin, Weichang Feng, and Meirong Zhao. A novel automatic weighted image fusion algorithm. In *Intelligent Systems and Applications, 2009. ISA 2009. International Workshop on*, pages 1–4. IEEE, 2009.

[170] Dong Jiang, Dafang Zhuang, Yaohuan Huang, and Jinying Fu. Survey of multispectral image fusion techniques in remote sensing applications. In *Image fusion and its applications*. Intech, 2011.

[171] Mark D Jasiunas, David A Kearney, John Hopf, and Grant B Wigley. Image fusion for uninhabited airborne vehicles. In *Field-Programmable Technology, 2002.(FPT). Proceedings. 2002 IEEE International Conference on*, pages 348–351. IEEE, 2002.

[172] Jeff R Harris, Richard Murray, and Tom Hirose. Ihs transform for the integration of radar imagery with other remotely sensed data. *Photogrammetric Engineering and Remote Sensing*, 56(12):1631–1641, 1990.

[173] Filippo Nencini, Andrea Garzelli, Stefano Baronti, and Luciano Alparone. Remote sensing image fusion using the curvelet transform. *Information Fusion*, 8(2):143–156, 2007.

[174] Aliaksei Sandryhaila and José MF Moura. Discrete signal processing on graphs. *IEEE transactions on signal processing*, 61(7):1644–1656, 2013.

[175] David I Shuman, Christoph Wiesmeyr, Nicki Holighaus, and Pierre Vandergheynst. Spectrum-adapted tight graph wavelet and vertex-frequency frames. *IEEE Transactions on Signal Processing*, 63(16):4223–4235, 2015.

[176] J Zhou, DL Civco, and JA Silander. A wavelet transform method to merge landsat tm and spot panchromatic data. *International Journal of Remote Sensing*, 19(4):743–757, 1998.

[177] Paul Scheunders and Steve De Backer. Fusion and merging of multispectral images with use of multiscale fundamental forms. *JOSA A*, 18(10):2468–2477, 2001.

[178] David A Yocky. Multiresolution wavelet decomposition i me merger of landsat thematic mapper and spot panchromatic data. *Photogrammetric Engineering & Remote Sensing*, 62(9):1067–1074, 1996.

[179] Qiang Zhang and Bao-long Guo. *Signal Processing*.

[180] Gaurav Bhatnagar, QM Jonathan Wu, and Zheng Liu. Directive contrast based multimodal medical image fusion in nsct domain. *IEEE Transactions on Multimedia*, 15(5): 1014–1024, 2013.

[181] Sneha Singh, Deep Gupta, RS Anand, and Vinod Kumar. Nonsubsampled shearlet based ct and mr medical image fusion using biologically inspired spiking neural network. *Biomedical Signal Processing and Control*, 18:91–101, 2015.

[182] Shutao Li, James T Kwok, and Yaonan Wang. Using the discrete wavelet frame transform to merge landsat tm and spot panchromatic images. *Information Fusion*, 3(1): 17–23, 2002.

[183] Hasan Demirel and Gholamreza Anbarjafari. Image resolution enhancement by using discrete and stationary wavelet decomposition. *IEEE transactions on image processing*, 20(5):1458–1460, 2011.

[184] Stephane G Mallat. A theory for multiresolution signal decomposition: the wavelet representation. *IEEE transactions on pattern analysis and machine intelligence*, 11(7): 674–693, 1989.

[185] Vladimir S Petrovic and Costas S Xydeas. Gradient-based multiresolution image fusion. *IEEE Transactions on Image processing*, 13(2):228–237, 2004.

[186] Javier Portilla, Vasily Strela, Martin J Wainwright, and Eero P Simoncelli. Adaptive wiener denoising using a gaussian scale mixture model in the wavelet domain. In *Image Processing, 2001. Proceedings. 2001 International Conference on*, volume 2, pages 37–40. IEEE, 2001.

[187] . URL `http://hitech.technion.ac.il/feldman/hvd.html`.

[188] . URL http://openremotesensing.net/index.php/codes/11-pansharpening/2-pansharpening.

[189] Lucien Wald. Quality of high resolution synthesised images: Is there a simple criterion? In *Third conference" Fusion of Earth data: merging point measurements, raster maps and remotely sensed images"*, pages 99–103. SEE/URISCA, 2000.

[190] Yanfei Zhong, Qiqi Zhu, and Liangpei Zhang. Scene classification based on the multifeature fusion probabilistic topic model for high spatial resolution remote sensing imagery. *IEEE Transactions on Geoscience and Remote Sensing*, 53(11):6207–6222, 2015.

[191] Johanna Schmidt, M Eduard Gröller, and Stefan Bruckner. Vaico: Visual analysis for image comparison. *IEEE Transactions on Visualization and Computer Graphics*, 19(12): 2090–2099, 2013.

[192] Lei Tong, Jun Zhou, Yuntao Qian, Xiao Bai, and Yongsheng Gao. Nonnegative-matrix-factorization-based hyperspectral unmixing with partially known endmembers. *IEEE Transactions on Geoscience and Remote Sensing*, 54(11):6531–6544, 2016.

[193] Xiao Bai, Chuntian Liu, Peng Ren, Jun Zhou, Huijie Zhao, and Yun Su. Object classification via feature fusion based marginalized kernels. *IEEE Geoscience and Remote Sensing Letters*, 12(1):8–12, 2015.

[194] Rafael C Gonzalez et al. Re woods, digital image processing. *Addison–Wesely Publishing Company*, 1992.

[195] Miodrag Potkonjak, Saro Meguerdichian, and Jennifer L Wong. Trusted sensors and remote sensing. In *Sensors, 2010 IEEE*, pages 1104–1107. IEEE, 2010.

[196] Haldun M Ozaktas, Orhan Arikan, M Alper Kutay, and Gozde Bozdagi. Digital computation of the fractional fourier transform. *IEEE Transactions on signal processing*, 44 (9):2141–2150, 1996.

[197] Jaewan Choi, Kiyun Yu, and Yongil Kim. A new adaptive component-substitution-based satellite image fusion by using partial replacement. *IEEE Transactions on Geoscience and Remote Sensing*, 49(1):295–309, 2011.

[198] Te-Ming Tu, Shun-Chi Su, Hsuen-Chyun Shyu, and Ping S Huang. A new look at ihs-like image fusion methods. *Information fusion*, 2(3):177–186, 2001.

[199] Manfred Ehlers, Sascha Klonus, Pär Johan Åstrand, and Pablo Rosso. Multi-sensor image fusion for pansharpening in remote sensing. *International Journal of Image and Data Fusion*, 1(1):25–45, 2010.

[200] Juliana G Denipote and Maria Stela V Paiva. A fourier transform-based approach to fusion high spatial resolution remote sensing images. In *Computer Vision, Graphics & Image Processing, 2008. ICVGIP'08. Sixth Indian Conference on*, pages 179–186. IEEE, 2008.

[201] Parul Shah, TV Srikanth, SN Merchant, and UB Desai. A novel multifocus image fusion scheme based on pixel significance using wavelet transform. In *IVMSP Workshop, 2011 IEEE 10th*, pages 54–59. IEEE, 2011.

[202] http://www.metapix.de/examples.htm/. .

[203] H Sharma and KK Sharma. Baseline wander removal of ecg signals using hilbert vibration decomposition. *Electronics Letters*, 51(6):447–449, 2015.

[204] KK Sharma and Mohit Sharma. Image fusion based on image decomposition using self-fractional fourier functions. *Signal, image and video processing*, 8(7):1335–1344, 2014.

[205] JB Sharma, KK Sharma, and Vineet Sahula. Hybrid image fusion scheme using self-fractional fourier functions and multivariate empirical mode decomposition. *Signal Processing*, 100:146–159, 2014.

[206] KK Sharma. Fractional laplace transform. *Signal, image and video processing*, 4(3): 377–379, 2010.

[207] Luis B Almeida. The fractional fourier transform and time-frequency representations. *IEEE Transactions on signal processing*, 42(11):3084–3091, 1994.

[208] Haldun M Ozaktas, Zeev Zalevsky, and M Alper Kutay. *The fractional Fourier transform*.

[209] Bruno Garguet-Duport, Jacky Girel, and Jean-Marc Chassery. The use of multiresolution analysis and wavelets transform for merging spot panchromatic and multispectral image data. *Photogrammetric Engineering and remote sensing*, 62(9):1057–1066, 1996.

[210] Shuang Li and Zhilin Li. Effects of image fusion algorithms on classification accuracy. In *2010 18th International Conference on Geoinformatics*, pages 1–6. IEEE, 2010.

[211] Kamalesh Kumar Sharma and Shiv Dutt Joshi. Papoulis-like generalized sampling expansions in fractional fourier domains and their application to superresolution. *Optics communications*, 278(1):52–59, 2007.

[212] KK Sharma and SD Joshi. On scaling properties of fractional fourier transform and its relation with other transforms. *Optics communications*, 257(1):27–38, 2006.

[213] Kamalesh Kumar Sharma and Shiv Dutt Joshi. Signal reconstruction from the undersampled signal samples. *Optics communications*, 268(2):245–252, 2006.

[214] KK Sharma and SD Joshi. Fractional fourier transform of bandlimited periodic signals and its sampling theorems. *Optics communications*, 256(4):272–278, 2005.

[215] Ute G Gangkofner, Pushkar S Pradhan, and Derrold W Holcomb. Optimizing the high-pass filter addition technique for image fusion. *Photogrammetric Engineering & Remote Sensing*, 74(9):1107–1118, 2008.

[216] JG Liu. Smoothing filter-based intensity modulation: a spectral preserve image fusion technique for improving spatial details. *International Journal of Remote Sensing*, 21 (18):3461–3472, 2000.

[217] Qing Guo, Qu Wang, Zhengjun Liu, An Li, Hongqun Zhang, and Zhongkui Feng. Multispectral and panchromatic image fusion using a joint spatial domain and transform domain for improved dfrnt. *Optik-International Journal for Light and Electron Optics*, 126(24):5241–5248, 2015.

[218] Luyi Bai, Changming Xu, and Cong Wang. A review of fusion methods of multi-spectral image. *Optik-International Journal for Light and Electron Optics*, 126(24):4804–4807, 2015.

[219] Qing Guo and Shutian Liu. Performance analysis of multi-spectral and panchromatic image fusion techniques based on two wavelet discrete approaches. *Optik-International Journal for Light and Electron Optics*, 122(9):811–819, 2011.

[220] Ingrid Daubechies. *Ten lectures on wavelets*. SIAM, 1992.

[221] Parishwad P Vaidyanathan. *Multirate systems and filter banks*. Pearson Education India, 1993.

Publications

International Journal Papers

1. Nidhi Saxena and K.K. Sharma, “Hilbert vibration decomposition based image fusion,” Electronics Letters, vol. 52, no. 19, pp. 1605-1607, 2016.
2. Nidhi Saxena and K.K. Sharma, “Pansharpening approach using Hilbert vibration decomposition,” IET Image Processing 11.12, pp.1152-1162, 2017.
3. Nidhi Saxena and K.K. Sharma, “Pansharpening scheme using filtering in two dimensional discrete fractional Fourier transform,” IET Image Processing journal 12.6, pp.1013-1019 2018.
4. Nidhi Saxena and K.K. Sharma, “Two dimensional discrete fractional Fourier transform based pansharpening scheme,” IJRS journal, Taylor’s and Frances, (**under revision**).
5. Nidhi Saxena and K.K. Sharma, “Spectral graph wavelet filterbank based pansharpening scheme,” Signal, Image and Video Processing journal, (**under review**).

International Conference Papers

1. Nidhi Saxena and K.K. Sharma, “Image fusion scheme using two dimensional discrete fractional Fourier transform,” IEEE International Conference CICT 2017, 3-5 Nov. 17, IIITM Gwalior.
2. Nidhi Saxena and K.K. Sharma, “A hybrid approach for pansharpening using Hilbert vibration decomposition,” IEEE International Conference ICPCSI 2017, 21-22 Sep. 17, Chennai.